

Numerical Modeling of a Thermal-Hydraulic Loop and Test Section Design for Heat Transfer Studies in Supercritical Fluids

By

Daniel M^cGuire

A thesis submitted to
The Faculty of Graduate and Postdoctoral Affairs
in partial fulfilment of
the degree requirements of
Masters of Applied Science

Ottawa-Carleton Institute for
Mechanical and Aerospace Engineering

Department of Mechanical and Aerospace Engineering
Carleton University
Ottawa, Ontario, Canada
May 2011

Copyright ©
2011 – Daniel M^cGuire



Library and Archives
Canada

Published Heritage
Branch

395 Wellington Street
Ottawa ON K1A 0N4
Canada

Bibliothèque et
Archives Canada

Direction du
Patrimoine de l'édition

395, rue Wellington
Ottawa ON K1A 0N4
Canada

Your file Votre référence

ISBN: 978-0-494-93516-3

Our file Notre référence

ISBN: 978-0-494-93516-3

NOTICE:

The author has granted a non-exclusive license allowing Library and Archives Canada to reproduce, publish, archive, preserve, conserve, communicate to the public by telecommunication or on the Internet, loan, distribute and sell theses worldwide, for commercial or non-commercial purposes, in microform, paper, electronic and/or any other formats.

The author retains copyright ownership and moral rights in this thesis. Neither the thesis nor substantial extracts from it may be printed or otherwise reproduced without the author's permission.

AVIS:

L'auteur a accordé une licence non exclusive permettant à la Bibliothèque et Archives Canada de reproduire, publier, archiver, sauvegarder, conserver, transmettre au public par télécommunication ou par l'Internet, prêter, distribuer et vendre des thèses partout dans le monde, à des fins commerciales ou autres, sur support microforme, papier, électronique et/ou autres formats.

L'auteur conserve la propriété du droit d'auteur et des droits moraux qui protègent cette thèse. Ni la thèse ni des extraits substantiels de celle-ci ne doivent être imprimés ou autrement reproduits sans son autorisation.

In compliance with the Canadian Privacy Act some supporting forms may have been removed from this thesis.

While these forms may be included in the document page count, their removal does not represent any loss of content from the thesis.

Conformément à la loi canadienne sur la protection de la vie privée, quelques formulaires secondaires ont été enlevés de cette thèse.

Bien que ces formulaires aient inclus dans la pagination, il n'y aura aucun contenu manquant.

Canada

Abstract

A numerical tool for the simulation of the thermal dynamics of pipe networks with heat transfer has been developed with the novel capability of modeling supercritical fluids. The tool was developed to support the design and deployment of two thermal-hydraulic loops at Carleton University for the purpose of heat transfer studies in supercritical and near-critical fluids. First, the system was characterized based on its defining features; the characteristic length of the flow path is orders of magnitude larger than the other characteristic lengths that define the system's geometry; the behaviour of the working fluid in the supercritical thermodynamic state. An analysis of the transient thermal behaviour of the model's domains is then performed to determine the accuracy and range of validity of the modeling approach for simulating the transient thermal behaviour of a thermal-hydraulic loop.

Preliminary designs of three test section geometries, for the purpose of heat transfer studies, are presented in support of the overall design of the Carleton supercritical thermal-hydraulic loops. A 7-rod-bundle, annular and tubular geometries are developed with support from the new numerical tool. Materials capable of meeting the experimental requirements while operating in supercritical water are determined. The necessary geometries to satisfy the experimental goals are then developed based on the

material characteristics and predicted heat transfer behaviour from previous simulation results. An initial safety analysis is performed on the test section designs, where they are evaluated against the *ASME Boiler, Pressure Vessel, and Pressure Piping Code* standard, required for safe operation and certification.

To my parents and brother: for all your support.

Acknowledgements

It is with heartfelt gratitude that I acknowledge the support and guidance of (now) Drs. Dylan McGuire and Chukwudi Azhi. Their contributions throughout my graduate education proved invaluable, providing personal encouragement as well as lending their weight of knowledge and experience to my endeavours. In addition I would like to extend my sincere appreciation of the opportunity provided by Professor Metin Yaras and his support and guidance through the process. His mentorship and insight has provided a unique and rewarding educational experience that left me enriched for the journey. I have been truly fortunate to have met these people and shared this experience with them.

Table of Contents

Abstract	
Acknowledgements	ii
Table of Contents	iii
List of Figures	vi
List of Tables	x
Nomenclature	xii
Chapter 1 Introduction	1
1.1 Background	1
1.1.1 Carleton Supercritical Facility	2
1.2 Objectives.....	6
1.2.1 Development of Predictive Tools.....	7
1.2.2 Development of Test sections to meet Experimental Goals	8
Chapter 2 Literature Survey	9
2.1 Modeling the Transient Thermal Response of a Discretized System	10
2.2 Modeling One-Dimensional, Compressible Flow.....	16
2.2.1 Capturing Turbulence Effects	19
2.3 Test Section Design	31
Chapter 3 Modeling a Thermal-Hydraulics Loop	32
3.1 Numerical Methods	34
3.2 Fluid Modeling	36
3.3 Solid Material Modeling.....	39
3.4 Discretization and Numerical Stability Analysis.....	40

3.4.1 Discretization of Governing Equations	41
3.4.2 Stability Analysis	44
3.5 Modeling and Meshing of Loop Components	46
3.5.1 Piping Modeling	46
3.5.2 Component Modeling	49
3.5.3 Meshing.....	55
3.6 Algorithm	58
3.7 Conclusion.....	62
Chapter 4 Numerical Simulation Results	67
4.1 Time Step Size	67
4.2 Grid Independence	68
4.3 Benchmarks and Quality Assurance	72
4.3.1 Conduction in the Fluid Domain	73
4.3.2 Convection in the Fluid Domain.....	75
4.3.3 Conduction in the Solid Domain	77
4.3.4 Fluid Property Handling	80
4.4 Simulation Results.....	81
Chapter 5 Material Selection	88
5.1 High Temperature Alloys	88
5.2 Corrosion.....	89
5.3 Ceramic Coatings	92
5.4 Electrical Resistivity and Conductor.....	93
Chapter 6 Preliminary Test section Design	96
6.1 Background	96
6.2 Test section Geometry.....	103
6.2.1 Loop Interface.....	104
6.2.2 7-Rod-Bundle Test section.....	108
6.2.3 Annular Test section	114

6.2.4 Tubular Test section.....	117
6.3 Electric Resistive Heating.....	118
6.3.2 Convective Heat Transfer Coefficient and Heating Element Temperature...	121
6.3.4 Power Delivery and Electric Insulation	129
6.4 Safety Analysis and Certification.....	139
6.4.1 ASME Boiler, Pressure Vessel, and Pressure Piping Code Standards	139
6.4.2 Sealing.....	146
Chapter 7 Conclusions and Future Work	154
7.1 Transient Thermal Numerical Solver	154
7.1.1 – Numerical Solver and Simulation Results	154
7.1.2 Suggested Future Simulation Work	155
7.2 Thermal-hydraulic Loop Test sections	155
7.1.1 Test section Designs.....	155
7.1.2 Material Selection.....	156
7.1.3 Suggested Future Test section Work.....	156
List of References	158
Appendix A:	164
Appendix B:	171
Appendix C:	173

List of Figures

Figure 1-1: Supercritical Fluids Facility at Carleton [5]	3
Figure 1-2: "Layout and Major Components of the SCW loop" [5]	4
Figure 1-3: Grayloc Connector [5][6]	6
Figure 2-1: "Dimensionless temperature profile at the outlet of the supply pipe" [12]..	15
Figure 2-2: "Dimensionless temperature profile at the outlet of the return pipe" [12]..	16
Figure 2-3: "Comparison of experimental Nusselt number and Dittus-Boelter correlation" [7][25]	23
Figure 2-4: "Comparison of experimental Nusselt number and Jackson correlation" [7]	24
Figure 2-5: "Effect of Prandtl number on turbulent flow temperature distribution; Re = 100,000" [26]	26
Figure 2-6: Sleicher and Rouse vs Jackson, Nusselt Correlations for Re = 100000 at 25 MPa	27
Figure 2-7: "Single-phase heat transfer at prototypical SCWR conditions" [4].....	28
Figure 2-8: "CFD and Nusselt correlation in comparison to Shitsman experiment" [7]..	29
Figure 2-9: "Heat transfer coefficient in the low bulk temperature region" [31]	30
Figure 3-1: General Component Segment Model.....	33
Figure 3-2: General Node Distribution for a Solid Material.....	42
Figure 3-3: Magnitude of Stability Criterion for the limiting values of β_1 and β_2 for the Two-Dimensional DuFort-Frankel Method	45
Figure 3-4: Feature Modeling of a Butt Weld Hub and Pipe	48
Figure 3-5: Determining Additional Thickness Distribution for Piping Features	49
Figure 3-6: Tubular Test section Schematic.....	50
Figure 3-7: Annular Test section Schematic	51
Figure 3-8: 7 Rod Bundle Test section Schematic.....	51

Figure 3-9: Heat Exchanger Schematic	52
Figure 3-10: Cut away of SLM-NVE pump from Klaus Union [24]	54
Figure 3-11: Typical Mesh for a Component and Piping Run	57
Figure 3-12: Flow Chart Key	58
Figure 4-1: Thermal Time Constant versus Temperature for 7-Rod-Bundle Test section at 25 MPa and Mass Flow Rate of 0.127 kg/s.....	70
Figure 4-2: "Exponential response curve [1st Order]" [42]	73
Figure 4-3: Axial Conduction in the Fluid Domain	74
Figure 4-4: Fluid Temperature Profile at Selected Times	74
Figure 4-5: First Fluid Cell's Temperature Response to a Step Input, Axial Conduction ..	75
Figure 4-6: Fluid's Temperature Response to a Step Input, Convective Heat Transfer ...	77
Figure 4-7: One Dimensional Radial Conduction in the Solid Domain	78
Figure 4-8: Solid Temperature Profile at Selected Times	78
Figure 4-9: First Solid Cell's Temperature Response to a Step Input, Radial Conduction	79
Figure 4-10: Fluid Temperature Profile.....	84
Figure 4-11: Temperature versus Time, Test section	86
Figure 4-12: Temperature versus Time, Heat Exchanger	87
Figure 5-1: Tensile Properties of Annealed IN625 [44]	88
Figure 5-2: "Weight gain as a function of corrosion time for 1520S and 1520Ti exposed to supercritical water at 400, 500, 600oC, <1000h" [52]	90
Figure 5-3: Typical Weight Gain of a High Chromium Nickel Superalloy [53]	91
Figure 5-4: Temperature versus Electrical Resistivity for Selected Superalloys and Ceramics [44][51][59][61]	94
Figure 5-5: Copper Tensile Strength versus Temperature [63][64].....	95
Figure 6-1: "Sliding Thermocouples Assembly and Carrier." [59]	97
Figure 6-2: "Heat Transfer Loop" [7]	98
Figure 6-3: "Heater Schematic." [7]	99
Figure 6-4: "Pressure Boundary." a) Fixed Position, b) Allowing Differential Expansion [7]	100

Figure 6-5: “Leak-proof seal and insulation structure of the [Xi’an Jiaotong] test section” [25]	101
Figure 6-6: “Cross Section of Test section [Types]” [69]	104
Figure 6-7: Test section Loop Interface [5]	105
Figure 6-8: Common Test section Elements	106
Figure 6-9: Inlet/Outlet Block, 7-Rod-Bundle Test section	107
Figure 6-10: 7-Rod-Bundle Test section Cross Section	110
Figure 6-11: 7-Rod-Bundle Sub-channel and Periphery-channel Cross Section.....	111
Figure 6-12: 7-Rod-Bundle Inlet/Outlet Assembly Exploded View.....	112
Figure 6-13: Inlet Cross Section and Flow Distribution Illustration, 7-Rod-Bundle Test section.....	113
Figure 6-14: Annular Test section Cross Section	115
Figure 6-15: Inlet Cross Section, Annular Test section	116
Figure 6-16: Inlet Cross Section, Tubular Test section.....	117
Figure 6-17: Convective Heat Transfer Coefficient versus Temperature for the Test sections with a Mass Flow Rate of 0.125 kg/s	123
Figure 6-18: Steady State Fluid Temperature Profile in the Test section.....	124
Figure 6-19: Heating Element Temperature versus Test section Length at Maximum Heat Flux.....	125
Figure 6-20: Heating Element to Fluid Temperature Difference versus Test section Length at Maximum Heat Flux.....	126
Figure 6-21: Heat Transfer Coefficient versus Test section Length at Maximum Heat Flux	127
Figure 6-22: Heat Transfer Coefficient versus Heating Element Temperature at Maximum Heat Flux.....	128
Figure 6-23: Cam-Lok E1017 Series Female Receptacles [74]	129
Figure 6-24: Electrical Bus and Test section Assembly	130
Figure 6-25: 7-Rod-Bundle Copper Bus and Gasket	132
Figure 6-26: 7-Rod-Bundle Coating Schematic	132

Figure 6-27: Kanthal Thickness and Area Profile versus Heated Test section Length....	133
Figure 6-28: Tubular Test section with Electric Buses	137
Figure 6-29: Tubular Test section Electrical Bus Assembly.....	138
Figure 6-30: Principle and von Mises Stress Variation with Radius of a Heated Rod at 28.35 MPa	145
Figure 6-31: "316 SS Swagelok Tube Fitting with Advanced Geometry Back Ferrules."	147
Figure 6-32: "Flange with Ring-type Joint Face" [5]	150
Figure 6-33: Copper Electrical Bus as Flange Ring and Gasket	151
Figure 6-34: Flange Cap, 7-Rod-Bundle Test section	152

List of Tables

Table 2-1: Transient Thermal-Hydraulic Model Capability [9]	19
Table 2-2: “Trends in generalizing heat transfer rate at supercritical pressures” [27]	25
Table 3-1: Loop Acoustic Data	37
Table 3-2: Viscous Heating Data	39
Table 4-1: Maximum Permissible Temperature Gradient for Different Axial Spacing.....	71
Table 4-2: Axial Conduction Fluid Domain Properties	74
Table 4-3: Convective Heat Transfer Fluid Domain Properties	76
Table 4-4: Radial Conduction Solid Domain Properties.....	78
Table 4-5: Simulation Model Component Definition.....	82
Table 4-6: Simulation Model Piping Definition.....	83
Table 4-7: Simulation Parameters	83
Table 5-1: Top Ten ASME Rated Materials at 650°C [49]	89
Table 5-2: Comparison of Ceramic Coating Applicability as Electrical Insulators [44] [60][61].....	92
Table 5-3: Mechanical Properties of Alumina at Room Temperature [61]	93
Table 6-1: Common Test section Elements	106
Table 6-2: Inlet/Outlet Block Elements Across Each Test section	108
Table 6-3: Internal Component Geometry Comparison, 7-Rod-Bundle Test section	108
Table 6-4: 7-Rod-Bundle Test section Geometry.....	110
Table 6-5: Sub-channel vs Periphery-channel Geometry	111
Table 6-6: Test Section Heated and Unheated Lengths	114
Table 6-7: Internal Component Geometry Comparison, Annular Test section	115
Table 6-8: Annular Test section Geometry	115
Table 6-9: Tubular Test section Reentrant Inlet/Outlet Geometry [22].....	118

Table 6-10: Basic Test section Power Characteristics IN625	120
Table 6-11: Test section Heat Flux and Peak Heating Element Surface Temperature ...	123
Table 6-12: 7-Rod-Bundle Coatings	133
Table 6-13: Copper Components Electrical Properties, 7-Rod-Bundle Test section [64]	134
Table 6-14: Test section Electrical Resistance, 7-Rod-Bundle Test section.....	135
Table 6-15: Test section Geometry Modified for Coatings, 7-Rod-Bundle Test section	135
Table 6-16: Copper Components Electrical Properties, Annular Test section [64]	136
Table 6-17: Test section Electrical Resistance, 7-Rod-Bundle Test section.....	137
Table 6-18: “Values of γ” [49]	140
Table 6-19: Minimum Wall Thickness of Inlet/Outlet Blocks, 7-Rod-Bundle and Annular Test section	140
Table 6-20: Branch Connections of Inlet/Outlet Blocks, 7-Rod-Bundle and Annular Test sections	142
Table 6-21: Minimum Wall Thickness for each of the Test section Shrouds.....	143
Table 6-22: Maximum Operating Temperature of Heated Test section Components IN625 [44]	145
Table 6-23: Flange Cap Geometry, 7-Rod-Bundle and Annular Test sections.....	152

Nomenclature

A – area

a - coefficient

\hat{a} - ratio of thermal energy storage capacity

Bi – Biot number

b - coefficient

C – Courant number; constant

c – specific heat capacity

\bar{c} – area averaged specific heat capacity

D – diameter

E – energy, efficiency factor

Fo – Fourier number

f – friction factor; forcing function

h – specific enthalpy; convective heat transfer coefficient

I – electric current

k - thermal conductivity

L – length

l – length

m – mass, meter

mmscf – million-standard-cubic-feet

mmscfd – million-standard-cubic-feet/day

Nu – Nusselt number

P – perimeter, power

Pr – Prandtl number

p – pressure

Q – heat

q – specific heat

R – radius, half height of channel, resistance

r - radius

Re – Reynolds number

S – allowable stress, non-dimensional variable

s - second

T - temperature

t - time; thickness

U - heat transmission coefficient

u - fluid velocity along the x-axis

V – volume, volts

W – watt

X – non-dimensional variable

x - principle axis

y – secondary axis, coefficient

Greek Symbols

α - thermal diffusivity

β - error frequency coefficient

ϵ - surface roughness

μ - dynamic viscosity

ν – Poisson’s Ratio

ϕ – Solution function

ρ – density

σ - stress

τ - shear stress, thermal time constant

Subscripts

b - bulk

c - characteristic, cross sectional

conv - convection

d - difference

h - hydraulic

i - inner, principle axis

j - secondary axis

m - mass averaged, minimum

n - coefficient, time step

o - initial value, outer

p - at constant pressure

s - surface

w - wall

∞ - infinite time; center line value or where property variation becomes zero

Chapter 1 Introduction

1.1 Background

In 2001 nine countries, including Canada, signed the Generation IV International Forum (GIF) charter to cooperatively carry out the preliminary research and development for the next generation of nuclear reactors. Of the six nuclear energy systems selected by the GIF for further investigation, Canada and Atomic Energy Canada Limited (AECL) were particularly interested in the supercritical-water-cooled reactor (SCWR) design, which the CANDU (CANada Deuterium Uranium) nuclear reactor design may be extended to, for improved efficiency and economics[1][2] [3] [4].

The primary research for GIF, including heat transfer in supercritical fluids, is to be carried out by academic institutions of the participating countries. Carleton University, with their industrial partner AECL, joined the project “Nuclear Ontario: A University-based Research Network Supporting CANDU Nuclear Technology in Ontario” to provide a facility to study phenomena in supercritical water and data derived from experimental work carried out in this facility. This provides the opportunity for Carleton to expand its research in the field of supercritical fluids, along with developing a world class research facility for experiments with supercritical water.

The use of supercritical fluid for power generation applications is highly desirable as fluids near their critical point have an increased specific heat capacity making them an excellent medium for heat absorption. A pure substance in the supercritical state does not experience a distinct phase change transitioning from a liquid state to a gaseous state, or vice versa. Unlike boiling reactors, supercritical reactors cannot suffer dry out where a vapour layer forms on the heating element reducing heat transfer, due to critical heat flux (CHF), which can lead to a rapid rise in

temperature of the heating elements and their subsequent failure [5]. In a nuclear reactor, melting the sheath of a fuel rod will result in the loss of containment of the fissile material, while in a classic boiler, a breach in the pressure vessel will result in the escape of high energy steam; both are serious safety concerns. The significant safety advantage inherent in supercritical fluids, by removing the possibility of dry out, coupled with the increased efficiency due to the increased operating pressure and temperatures make them attractive for use in modern power generation applications.

Power generation using supercritical water as the working fluid, as an emerging technology, has a limited body of knowledge concerning the fluid dynamics, material safety and heat transfer effects to draw upon. Experimental work carried out to date indicates that the tools currently available for design are insufficient to predict fluid behaviour near the critical point [4]. The extent of these tools' inaccuracies, and the resultant effects, are detailed in the chapters below. To help develop the body of knowledge on supercritical fluids, Carleton has built a new facility to house its supercritical fluids experimental apparatus.

1.1.1 Carleton Supercritical Facility

The Carleton supercritical fluids facility, shown in Figure 1-1 below, is comprised of the experimental apparatus and four main components: data acquisition, test section cooling lines, air conditioners to maintain the lab environment, and the DC power supply. The experimental apparatus are isolated from the operator by the layout of the floor space, while shielding provides a containment barrier between the apparatus and the rest of the facility. The power supply is capable of delivering a maximum of 300 kW of DC power at 150 V and 2000 A. The electric power dissipated in the supercritical thermal-hydraulic loop, either by a pre-heater or the test section, will be removed through the glycol coolant lines to an external cooling tower

(not pictured) that will reject the heat to the atmosphere. The facility is capable of meeting the experimental needs of the planned supercritical thermal-hydraulic loops, water and R134a. As pertains to the work presented in this document, and the goals of the GIF, the design of the supercritical water (SCW) loop will be expanded upon.

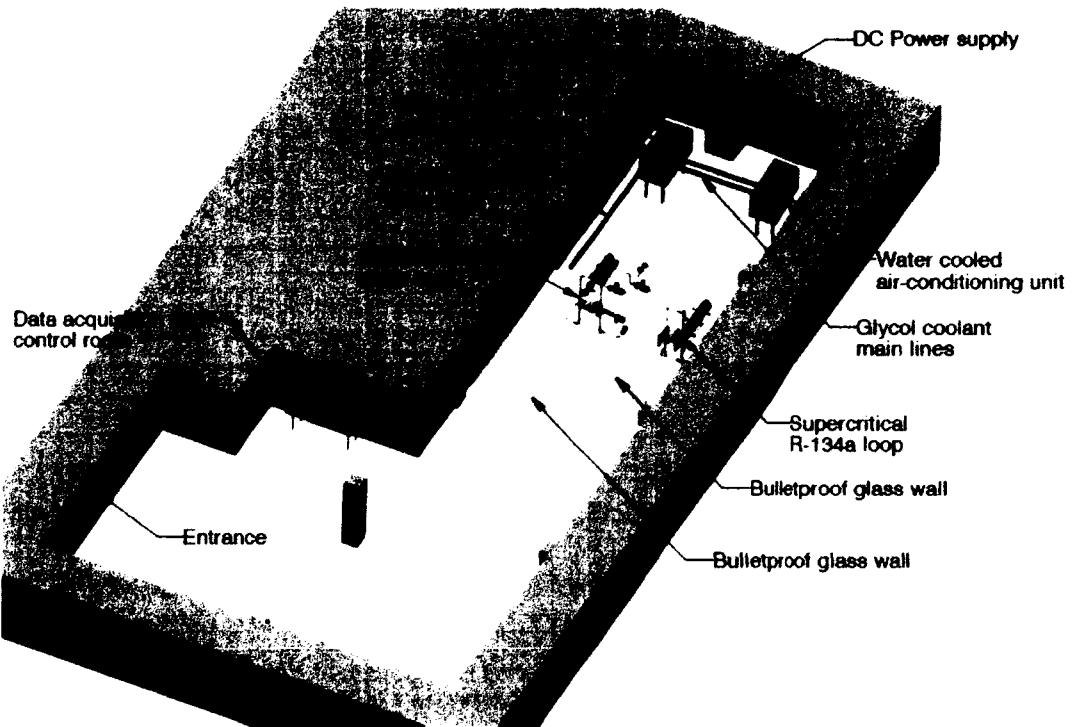


Figure 1-1: Supercritical Fluids Facility at Carleton [5]

Masih et al. have designed a thermal-hydraulics loop capable of meeting the experimental needs of the three planned test sections described in Chapter 6 [5]. A closed loop design is employed to minimize the extent of preheating upstream of the test section. The major loop components are detailed in Figure 1-2 below. A centrifugal pump is employed to provide variable flow rates, for the different experiments, with the necessary head rise at the loop's maximum operating pressure. The pump is rated to operate up to 28 MPa at its maximum operating temperature of 260 °C. A bypass line is employed to return any excess flow to the pump inlet without passing through the thermal-hydraulic loop to allow the loop to operate off

the pump's performance curves. This is especially important for low flow rate experiments. The control valves employed are globe valves, with solenoid actuators to allow for remote control of the flow at the data acquisition station. A commercially available turbine type flow meter was chosen for its operational rating that meets the loop's operating conditions, instead of a much more costly custom Coriolis mass flow meter. The heat exchanger, a U-tube type shell and tube heat exchanger, was designed by Advanced Industrial Components to interface with the glycol coolant lines and provide the capacity to reduce the working fluid from a maximum temperature of 600 °C to 260 °C. Downstream of the heat exchanger a twenty micron filter was installed to protect the pump from any particulate matter generated during loop operation. The loop is connected to an accumulator which provides pressure regulation and control for the loop.

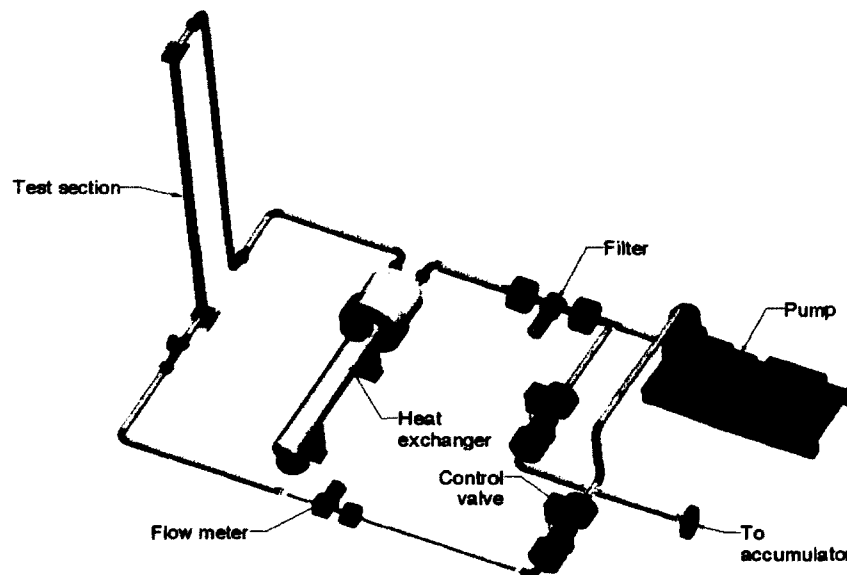


Figure 1-2: "Layout and Major Components of the SCW loop" [5]

The piping and fittings used to connect the various components were chosen to meet ASME power piping code. The majority of the piping is 316 SS NPS 1.5" schedule XXS, while NPS ¾" schedule 160 and reducers are used to interface the flow meter which requires a smaller

diameter fitting. The flanges are all of the ASME Class 2500 type, with the appropriate bore size to match the piping they are welded to. The additional connectors, shown in green in Figure 1-2, are Grayloc connectors (Figure 1-3). The Grayloc connectors are a proprietary flange design which provides superior performance in a smaller, lighter package and have been successfully employed in a previous SCW thermal-hydraulic design at the University of Wisconsin[5] [6] [7]. Grayloc connectors also have rotational freedom, allowing them to be installed with the bolts in any orientation. This allows the test section to be installed in the vertical or horizontal position, along with any variation in between. A complete list of the piping, fittings and components is provided in Appendix D

Test sections, for the purpose of heat transfer studies in SCW, have been designed to interface with the thermal-hydraulic SCW loop designed by Masih et al. The test section designs take advantage of the loop's modularity and the use of the Grayloc connectors to allow for the experiments to be carried out in the up-flow and down-flow vertical configuration, as well as the horizontal configuration. The specifics of the designs and their individual purposes are covered in Chapter 6.

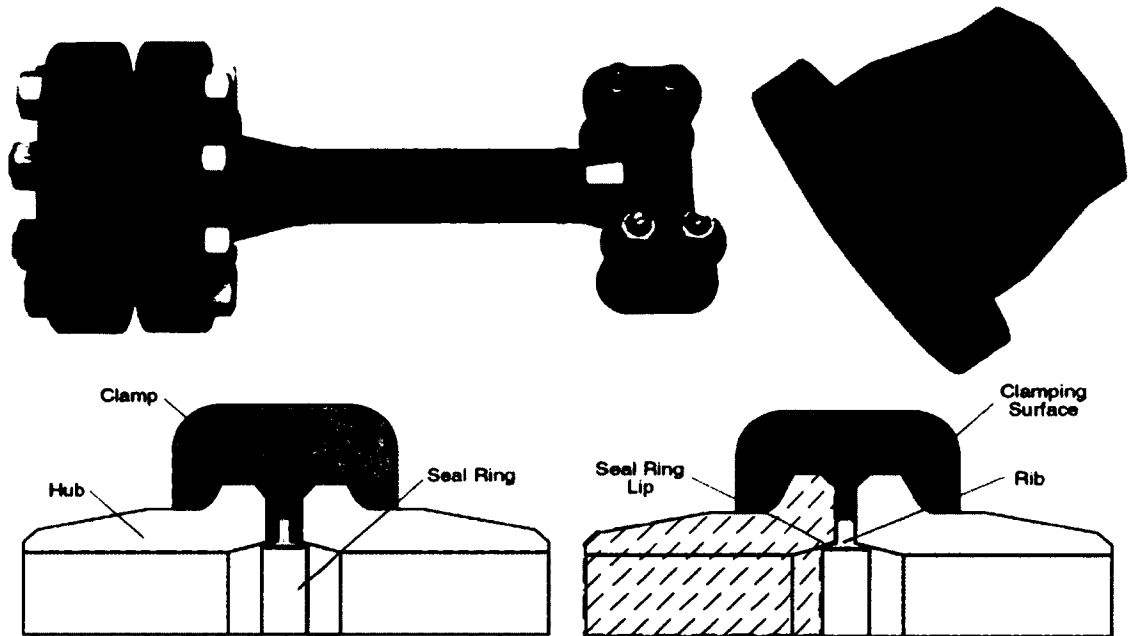


Figure 1-3: Grayloc Connector [5][6]

1.2 Objectives

While the supercritical facility was being built and the conceptual design of the supercritical thermal-hydraulic loop was carried out by the other members of Carleton's supercritical fluids research group, a need for an additional numerical tool capable of predicting the loop's transient thermal response was identified. Once the characterization of the loop's thermal properties were made available through the new numerical tool, the preliminary design of the initial set of test sections could be finalized to meet both the experimental goals and operational requirements of the thermal- hydraulic loop. This work presented herein describes the work performed by the authour to meet the two objectives of developing a suitable numerical tool and the completion of the preliminary design of a set of test sections.

1.2.1 Development of Predictive Tools

To support the design of the supercritical fluids facility and carry out preliminary investigations on the thermal-hydraulic loops' behaviour, a suitable numerical tool for investigating thermal response is required to complement the available tools for predicting a mechanical response and complement the experimental work. Modern computational fluid dynamic codes, based on the three-dimensional Navier-Stokes Equations, are unsuitable for this application, as described in Chapters 2 and 3, while current pipeline simulation codes lack the range of fluid handling and flexibility to cover the operational range and geometry of the proposed supercritical thermal-hydraulic loops. The lack of suitable numerical tools for predicting the transient thermal response of a supercritical thermal-hydraulics loop provided the motivation to develop a new computational tool that extends the current capability of pipeline simulation codes.

The input provided by thermal simulation results enables a mechanical solver to accurately predict the coupled thermal-mechanical behaviour of the thermal-hydraulic loop through its various operating modes, assisting in the validation and certification of the design. Beyond the design and validation process, the code provides for the ability to perform parametric studies on loop start-up and shut-down procedures or failure modes in support of the design and operation of a control system.

Detailed in Chapter 2, the inaccuracy of current heat transfer correlations for supercritical fluids necessitates the experimental work to be carried out at the Carleton supercritical fluids facilities. While these inaccuracies limit the accuracy of numerical solvers which rely on them, future experimental data can be used as part of the parametric studies carried out by the new code to improve both the heat transfer correlations and simulation accuracy. This iterative improvement will help advance the numerical tool's applicability to additional systems,

permitting the code to become an established resource for future work involving thermal-hydraulic systems.

1.2.2 Development of Test sections to meet Experimental Goals

With the preliminary design of a supercritical thermal-hydraulic loop complete, an appropriate set of test sections capable of interfacing with the thermal-hydraulic loop and meeting the experimental goals are required. Three test section designs were proposed to meet the initial set of experimental goals of studying heat transfer phenomena in supercritical fluid; a tubular test section for fundamental heat transfer studies; an annular test section for comparison purposes with previous work; a 7-rod-bundle configuration to investigate sub-channel and spacer design impact. The test section designs require a modularity that allows for their easy exchange and interpretability between different working fluids for future fluid-to-fluid modeling studies with the extension of the experiments to additional fluids. Using the code developed to simulate the thermal-hydraulic loop to provide expected operating conditions, the three test section designs were taken through the preliminary design phase.

A review of suitable materials was carried out to establish the necessary base materials of the components. A common interface was developed to accommodate the different test section designs and provide a standard interface to the thermal-hydraulic loop. The designs were optimized to use commercially available components where applicable and to maximize the supercritical facilities' capability. Temperature and pressure data from the thermal simulation carried out on the supercritical water thermal-hydraulic loop was used to define the material's stress state for the purpose of certification. The designs were checked against the American Society of Mechanical Engineers (ASME) Power Piping standards to ensure they would meet certification requirements and operational safety goals.

Chapter 2 Literature Survey

This literature survey covers the modeling of piping networks, and their components, with heat transfer. Early work on the topic, which defined future endeavors, will be reviewed followed by a discussion of the current state of thermal-hydraulic numerical tools for piping networks. The general assessment of the topic will be expanded upon with a more detailed examination of the numerical methods and treatment of the flow, and the handling of heat transfer effects as pertains to the thermal-hydraulics of piping networks.

The motivation for using low order simulations to model a system originated in infancy of computer aided simulation, the reduced computational requirements and time, remains unchanged today, and continues to drive development of modern simulation tools[8] [9] [10] [11] [12]. Despite the predictive power of modern three dimensional multi physics solvers, such as the ANSYS or COMSOL software suites, they are poorly suited to handling simulations involving very high aspect ratios. In piping networks, and similar thermal-hydraulic flows, the flow path length of the piping and components in spatial dimensions can be many orders of magnitude greater than the characteristic lengths in the other two orthogonal directions. To be able to capture the physics of the system using a three dimensional multi physics program, the grid spacing of the computational mesh is limited based on the minimum typical characteristic length of the system, resulting in computational problems that exceed our computational resources at present. The problem can be made tenable by reducing the order of the system until the defining characteristic length allows for a sufficiently compact problem to be simulated by the available computational resources. The one dimensional flow with conjugate heat transfer approach has seen excellent success in the Oil and Gas industry and district heating

applications, and this work aims to extend it to hydraulically more complex systems[9][10][11][12].

With the continuous increase in computational power, the impetuous for performing one dimensional flow simulations waned until an interest in modeling conjugated forced convective heat transfer in ducts in the late 1980s drove a resurgence in the interest of one dimensional viscous flows. The work progressed from flows with heat transfer due to viscous dissipation to include full conjugate heat transfer with a thermally dynamic wall [13] [14] [15] [16] [17] [18]. All the works used the same set of assumptions to define the flow, and reduce the dimensionality of the problem: steady, laminar, fully developed flow inside a duct. The conjugate heat transfer systems were further restricted to neglect viscous dissipation and axial heat conduction, and that the fluids properties were constant, with only the temperature allowed to vary with time [14][15][16][17][18]. These assumptions allowed the problem to be defined by a constant velocity profile (Couette flow) and described as a Sturm-Liouville problem.

2.1 Modeling the Transient Thermal Response of a Discretized System

The heat transfer was reduced to a one dimensional problem by numerically decoupling the fluid-to-fluid and fluid-to-wall heat transfer. Every solution reviewed followed the same approach to discretizing the governing Equations in a quasi-steady, finite volume solver. The quasi-steady approach was used to eliminate the time dependency in the Equations, with the assumption that the system was capable of re-establishing equilibrium between time steps for the given inputs. This approach relies on the lumped thermal capacitance model to be accurate throughout the system. The accuracy of this method was examined by comparing the difference between the exact solution and the quasi-steady solution (ϕ_d) to time dependent temperature, as the ratio of thermal energy storage capacity between the fluid and duct wall ($\hat{\alpha}$) approached

infinity [15]. Three different conditions, presented below, were examined that led to complete agreement between the exact and quasi-steady solutions.

$$\phi_d \rightarrow 0 \text{ as } S \rightarrow 0 \text{ for all } X, Fo$$

$$\phi_d \rightarrow 0 \text{ as } Fo \rightarrow \infty \text{ for all } S, X \text{ when } Fo < X \quad (2.1)$$

$$\phi_d \rightarrow 0 \text{ as } X \rightarrow \infty \text{ for all } S, Fo \text{ when } Fo > X$$

where: Fo : the Fourier number $\frac{\alpha t}{R^2}$; S : $\frac{UR}{k}$; X : $\frac{\alpha x}{R^2 u_m}$; α : thermal diffusivity of the fluid; t : time; R : half height of channel; U : heat transmission coefficient between ambient and duct wall; k : thermal conductivity of fluid; x : space coordinate along duct; u_m : mass averaged fluid velocity.

The first case represents the trivial solution for zero heat flux, where the ambient-wall interface is adiabatic and the wall itself has no thermal storage capacity, since $\hat{a} \rightarrow \infty$. The second case represents when the Courant number (2.2) is less than unity and the third case greater than unity. Where the Courant number is sufficiently small such that convective heat transfer due to fluid propagation is limited to the neighboring cell, the thermal diffusion in the fluid becomes the limiting factor in reaching convergence for a given time step.

$$C = \frac{u\Delta t}{\Delta x} \quad (2.2)$$

By allowing the Fourier number to approach infinity for a finite time step, thermal diffusion becomes instantaneous and therefore radial heat transfer in the system as well. The third case also represents a trivial solution where the mass averaged velocity is required to approach zero when the Courant number is greater than unity for the quasi-static solution to converge to the exact solution. For the Courant number to be greater than unity while the velocity approaches zero either the time step must approach infinity, or the mass acted on (represented by Δx) approach zero; both conditions representing trivial solutions. These three cases can be fully described by the lumped capacitance model of heat transfer for a general system [19]. While the assumption of uniform temperature distribution is valid, defined by $Bi < 0.1$, transient

conduction problems can be expressed in terms of their Biot and Fourier number as shown below.

$$Bi = \frac{h_{conv}L_c}{k} \quad (2.3)$$

$$\frac{T-T_\infty}{T_o-T_\infty} = \exp(-Bi \cdot Fo) \quad (2.4)$$

where: h_{conv} : convective heat transfer coefficient; L_c : characteristic length; k : thermal conductivity, T : temperature.

The temperature response is exponential, and given sufficient time it will reach the ambient, or forcing, temperature where the exact and quasi-steady solutions collapse to the same result. All three conditions outlined by Sucec are captured in the modified transient temperature Equation (2.5) [15]; the first case represents an adiabatic boundary condition, $T \equiv T_\infty$; the second is defined for $Fo \rightarrow \infty$; the third can be examined by using the alternate definition for the exponential term shown below:

$$Bi \cdot Fo = \frac{h_{conv}A_s t}{\rho V c} \quad (2.5)$$

where: h_{conv} : convective heat transfer coefficient; A_s : heat transfer surface area, t : time; ρ : density; V : volume of material; c : specific heat capacity.

In case three where the Courant number must be greater than unity while the fluid velocity approaches zero forces the time step or the cell size to approach infinity or zero respectively, and either of these will result in $Bi \cdot Fo \rightarrow \infty$. Therefore, all three conditions proposed by Sucec result in Equation 2.1 generating a value of zero, as defined by reaching steady state [15].

A concern using the lumped capacitance model for heat transfer not discussed in any of the literature reviewed, but encountered by the authour and Gabrielaitiene, is the error that may arise through applying the classic heat transfer Equation to a lumped heat capacitance model over a time step that is greater than necessary to reach steady state [12]. While Equation 2.5 accounts for the exponential temperature response of the system, the finite difference methods

employed assume that the temperature difference is constant over the time step. In the situation where the rate of heat transfer is large compared to the thermal capacity of a component (or discretized cell), the component can be heated or cooled beyond the driving temperature if the time step is too large. The finite volume solution to one-dimensional fluid flow and heat transfer in a pipe presented by Gabrielaitiene attempts to deal with a specific version of this error by reusing the previous time step's solution when a singularity condition is found [12]. While apparently addressing a stability concern with the numerical solver, this approach does not address why the solver would allow the solution to reach a non-physical state for a 'grid-independent' solution. The solver was developed at the Technical University of Denmark with a focus on tracking the time a mass of water requires to propagate between various nodes [20] [21]. The Equations presented for the conservation of energy in the system are all steady state Equations, and the forcing temperatures are "constant in each time period." As discussed above, for this interpretation, the Biot-Fourier condition must be met to accurately model transient behaviour with the lumped capacitance model. Benonysson et al. propose that given a "sufficiently small" time step, this error will become insignificant, however they also state that "it is impossible to determine what 'sufficiently small' means without experimentation" [20]. This is incorrect for two reasons, as the lumped capacitance model defines an analytical measure of an appropriate time step for a given expected temperature change, and it is not a maximum time step that is required, but rather a minimum time step defined by the temperature change and system parameters. The correct approach is defining an appropriately small node spacing, such that the finite volume defined matches the desired time step to meet the Biot-Fourier condition for necessary temperature change. This issue was addressed in the development of transient thermal solver in the present work, and will be discussed in Chapter 4.

Since all the flows considered by the authors discussed above are steady with constant properties, excluding temperature, Gabrielaitiene also used a finite element method to model a pipe flow with heat transfer by reducing the advection terms to an effective conduction coefficient and treating the system as purely diffusive[12]. The multi physics structural solver ANSYS was used to solve the modeled system with a second-order-accurate, implicit scheme [12]. Grid size was optimized based on the system's Reynolds number to produce grid independent results. While this should provide sufficient consideration for the Courant number, it does not address the concerns raised by using the lumped capacitance heat transfer model, for which no discussion was provided. The two different approaches, finite element versus finite volume were then compared to experimental data to determine which approach was more accurate. It was found that the finite element method (pseudo-transient) was superior in predicting the temperature field, while the finite volume method (node) is more accurate at predicting the transient trends of the temperature, shown in Figure 2-1 and 2-2 below [12].

The finite volume method was developed to solve a system dominated by advection, hence tends to capture the sudden change in temperature, shown in the experimental data, better than a purely diffusive approach employed by the finite element method. The finite element method demonstrates typical smoothing of the temperature gradient during a sharp transition, such as the arrival of the temperature wave, that is characteristic of a diffusive system. Both approaches over predict the peak temperature by 15% to 25%. The error is greatest where the temperature gradient (peak of temperature wave) is greatest, which correlates to an inaccuracy in the lumped capacitance model. If the Biot-Fourier number is not well matched to the system for the expected temperature change, the solver will over or under predict the heat transfer coefficient, and the error will be amplified by the temperature gradient. Based on the curves shown in Figures 2-1 and 2-2, it appears that the average heat transfer coefficient at each time

step is being over predicted yielding stronger heating and thus over predicting the peak temperature. While the finite element approach was better at predicting the heat transfer effects of the system, it does not appear to address the issue of using the lumped capacitance model introduced in the finite volume approach, but rather diffuses the effect over the simulation time instead of concentrating it at the peak temperature value. The finite volume method employed by Gabrielaitiene has the advantage of being able to differentiate between the advection and diffusion terms, and so better capture the time response of the system.

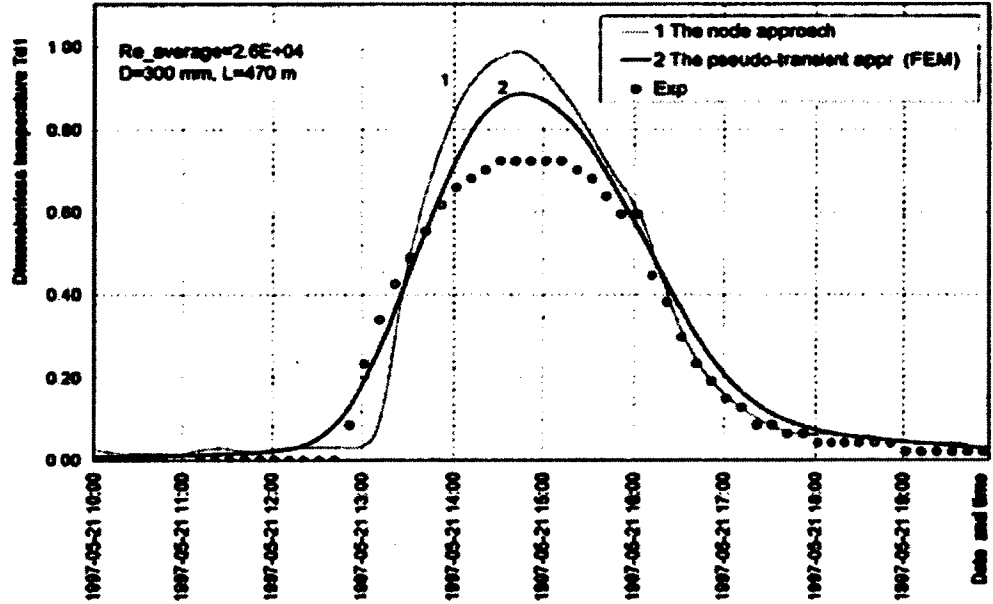


Figure 2-1: "Dimensionless temperature $\left[\frac{T_n - T_{ref}}{T_{max} - T_{ref}} \right]$ profile at the outlet of the supply pipe" [12]

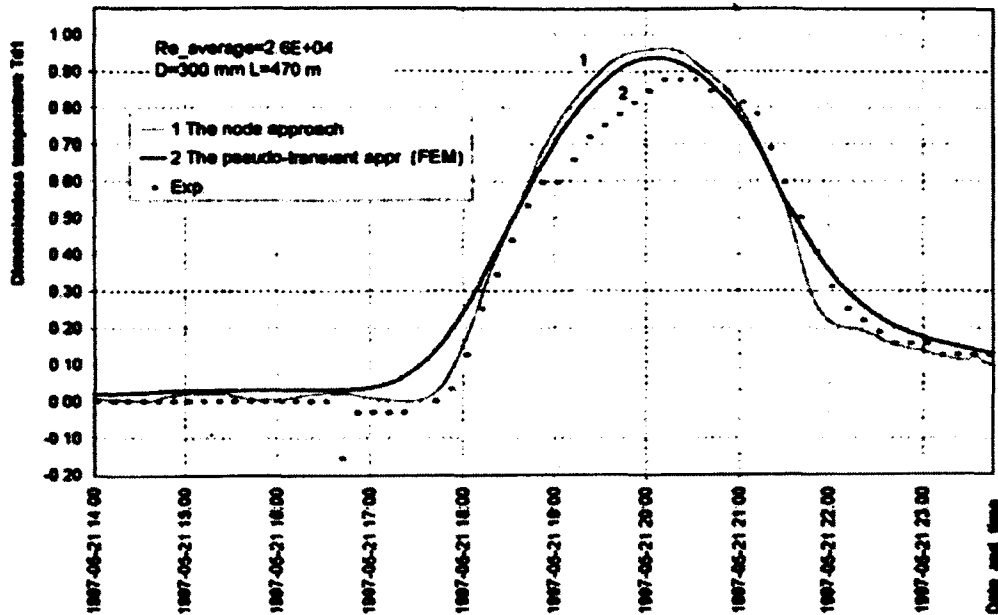


Figure 2-2: "Dimensionless temperature $\left[\frac{T_n - T_{ref}}{T_{max} - T_{ref}} \right]$ profile at the outlet of the return pipe" [12]

2.2 Modeling One-Dimensional, Compressible Flow

The literature reviewed above is limited to steady incompressible flows. This results in a constant velocity profile along the length of the system. Thus the variation in velocity along a dimension that is studied occurs in the radial direction of the flow. Defining the radial velocity profile for a laminar, incompressible flow allowed researchers to study conjugate heat transfer effects directly from the physics of the problem [13][14][15][16][17][18]. This approach is not appropriate for turbulent, unsteady or compressible flows, where information about the velocity in additional directions is important to the physics of the problem. Pipeline network thermal hydraulic simulation codes such as the one developed at the Technical University of Denmark, TERMIS (from 7 Technologies) and Pipeline Studio (from Energy Solutions International LTD) define the velocity in the major axis, and use a convective heat transfer coefficient to model the heat transfer due to turbulence and the radial velocity profile [10][11][12]. The academic code developed by the Technical University of Denmark assumes a

constant mass flow throughout the pipe network, with a constant density, resulting in velocity only varying with cross sectional area. TERMIS, while still assuming constant density, uses a coupled velocity-pressure solver to determine the flow field around the pipe network. Pipeline Studio, whose capability extends to modeling gases, allows for compressible flow when running a transient simulation. The Pipeline Studio approach represents the most complete model, and is capable of providing more accurate results for a broad range of scenarios suitable for the transient thermal simulations to be performed for the proposed thermal-hydraulics loop at Carleton. Modisette presented five numerical approaches to solving fluid-thermal piping models; coupled transient thermal and hydraulic; isothermal approximation; succession of steady states; leapfrog; pseudo-steady model with moving knots [9]. The fully coupled model is used as the standard to which the other models are compared, as its accuracy is only limited by the numerical scheme chosen to solve the fully coupled system. The isothermal approximation, while suitable for some simplistic pipeline simulations where there is no formal thermal model, it is not suitable for thermal simulations and will not be discussed further. Many of the limitations of the use of steady state Equations for modeling transient have been detailed above, and Modisette's conclusion supports that it is an inappropriate approach to a transient system for "its unique ability to instantly (and wrongly) propagate a short-lived temperature increase down the entire line... [the] modeler would probably be better off with an isothermal approximation" [9]. The pseudo-steady model with moving knots uses a mix of steady-state approximations while retaining some transient terms in the energy Equation. While computationally faster than the fully coupled model, it is unsuitable for use in highly compressible systems since it cannot accurately model the $\frac{dp}{dt}$ term in the energy Equation, which is critical for the thermal simulations to be carried out at Carleton.

The final alternative to the fully coupled model discussed is the leapfrog method. The leapfrog method differs from the fully coupled model in that while solving each Equation exactly, the thermal and hydraulic Equations are solved independently instead of simultaneously. This is done by solving the temperature from the pressure and velocity of the previous time step, and the pressure and velocity from the previous time step's temperature. For fully implicit schemes, this is faster as two smaller matrices are inverted instead of one large matrix; explicit schemes benefit by reducing the number of Equations that need to be iterated over. Depending on the leapfrog scheme implemented, a lead-lag error may be introduced by approximating the temperature, pressure or flow variables from the previous time step, and care must be taken to avoid this. In the leapfrog scheme used by Modisette, for his implicit scheme, "a linear extrapolation of the next-step temperature from the previous two steps" was necessary to avoid significant error in the results of the hydraulic model. Unlike the other simplified approaches presented, the leapfrog model was proven to be as accurate as the fully coupled model while retaining its computational speed advantage. Shown in the Table 2-1 comparing a steady state and transient simulation, the leapfrog model was able to produce the same results as the fully coupled model. The tests were carried out against typical pipeline scenarios, where Linepack refers to the storage capacity of a pipeline by varying the pressure, and survival time refers to the transient response of a system before an over demand at the delivery end causes supply pressure to fall below a defined value.

Table 2-1: Transient Thermal-Hydraulic Model Capability [9]

2.1.a: Steady State			2.1.b: Transient	
Model	Throughput [mmscfd]	Linepack [mmscf]	Model	Survival Time [min]
Correct	557.03	40.28	Correct	12:00
Leapfrog	557.03	40.28	Leapfrog	12:00
Steady State	557.03	40.28	Steady State	15:30
Isothermal	562.44	41.04	Isothermal	14:00
Moving Knots	558.35	40.45	Moving Knots	14:00

The computational speed advantage of the leapfrog method, which does not suffer for any of the approximation-induced error like the other methods, makes it the natural choice for a transient thermal-hydraulic solver for pipe flow simulation. The technical overview provided by Energy Solutions International details that Pipeline Studio uses a dynamic time step to maintain accuracy and stability [11]. The methods developed by Modisette, who developed the Pipeline Studio simulation engine, are all implicit, which have no time dependant stability criterion. Therefore the need to adjust the time step size would be derived from the use of the lumped capacitance heat transfer model as described above. This is further supported by the heat transfer model adopted by the various pipe line simulation models, including Pipeline Studio, and how they handle complex turbulent flow while retaining their one-dimensionality for the hydraulics.

2.2.1 Capturing Turbulence Effects

Detailed knowledge of the flow field's structure and local velocities are both unnecessary to characterize a typical pipe line flow with heat addition problem. Capturing the detailed flow structure requires many orders of magnitude more computational resources and computational time due to the increased node density and additional information that requires tracking. The additional information about the system being simulated gained for the increased computational cost and time does not necessarily improve the accuracy of the results that are of

interest in a pipe line simulation. This computational penalty provides the motivation to develop application-specific tools to handle large-aspect-ratio problems, where the characteristic spatial dimension is orders of magnitude larger than the other spatial dimensions. While commercial, three-dimensional computational fluid dynamic programs are readily available, and capable of simulating the thermal-hydraulic flows considered, they are poorly suited to the task due to their enforced higher dimensionality, such as CFX. The increased computational resources and time required to simulate the problems under consideration make the use of a program such as CFX infeasible.

Friction and Static Pressure Losses

While detailed knowledge of the flow structure is unnecessary, such details affect heat transfer and frictional losses, both which are information that is desired from the simulation. To accurately capture these effects without increasing the dimensionality of the simulation, one-dimensional thermal-hydraulic models use empirical correlations to determine local effects from bulk flow properties; these include convective heat transfer and pressure loss due to friction models [9][10][11][12][20][21].

The bulk velocity of the flow is tracked, and with knowledge of the fluids state, can be used to predict the local pressure loss due to friction effects using a friction factor correlation. The common approach to predicting the pressure loss is through the use of the Darcy-Weisbach Equation (Eqn. 2.6), where the friction factor is defined by a user specified correlation [9][10][11] [22]. The most common definition of the friction factor comes from Colebrook (Eqn. 2.7) that uses an interpolation formula, so was plotted by Moody to create the universally known *Moody chart* [22].

$$\Delta p = f \frac{L\rho u^2}{2D_h} \quad (2.6)$$

$$\frac{1}{f^{1/2}} = -2.0 \log \left(\frac{\epsilon}{3.7D_h} + \frac{2.51}{Re_{D_h} f^{1/2}} \right) \quad (2.7)$$

where: Δp : the pressure loss; f : the friction factor; L : the length over which the pressure drop is calculated; ρ : density; u : velocity; D_h : hydraulic diameter; ϵ : surface roughness of duct; Re_{D_h} : Reynolds number.

The Colebrook Equation has been found to be accurate to $\pm 15\%$ for design calculations for Reynolds' numbers up to 10^8 [22]. The primary limitation of the Darcy-Weisbach Equation is that it assumes incompressible flow. Additional correlations for the friction factor exist which may be more suitable for specific fluids and applications. For compressible flow where pressure drop along the calculated length results in significant compressibility effects, the use of the Weymouth, Panhandle A or B Equations may be more suitable [11] [23]. For small pressure drops, under 10% of the inlet pressure, the Darcy-Weisbach Equation can be as accurate as, or more accurate than, the compressible correlations [23] [24]. An explicit formula was presented by Haaland (Eqn. 2.8) instead of the Colebrook Equation (Eqn. 2.7), which varies from the implicit Equation by less than 2% [22]. The explicit version of the Darcy-Weisbach Equation is preferable where applicable due to its simplicity.

$$\frac{1}{f^{1/2}} = -1.8 \log \left(\left(\frac{\epsilon}{3.7D_h} \right)^{1.1} + \frac{6.9}{Re_{D_h}} \right) \quad (2.8)$$

Heat Transfer

Based on the heat transfer theory described in Appendix A, the complex heat transfer mechanisms between the fluid and surrounding solid in turbulent flow may be captured using a convective heat transfer coefficient with Newton's law of cooling. This approach is commonly employed and appears in both commercial and academic pipeline simulation models [10][11][12]. The accuracy of this approach lies with the correlation chosen to model the

convective heat transfer coefficient. For classic heat transfer systems, involving subcritical fluids, there are numerous well developed correlations for different geometries, boundary conditions and fluid Prandtl numbers. The Dittus-Boelter Equation is frequently used as the standard correlation for predicting the convective heat transfer coefficient and as such is the correlation most commonly compared to experimental results [4] [7] [25]. There are two problems using the Dittus-Boelter Equation; it requires previous knowledge of the system to satisfy a condition regarding the direction of heat transfer; it is not very accurate. Described by Kays et al. "it tends to over predict the Nusselt number for gases by at least 20 percent, and to under predict [the] Nusselt number for the higher-Prandtl-number fluids by 7-10 percent" [26]. The inability of the Dittus-Boelter Equation to accurately capture heat transfer behaviour in supercritical fluids is also highlighted by the work of Licht et al. and Li et al. on heat transfer in supercritical water [7][25]. When they compared their experimental data to the theoretical value derived from the Dittus-Boelter Equation, approximately 80% of the data was captured within an error of $\pm 25\%$, shown in Figure 2-3 below. The experimental data is also distributed around the correlation such that the Dittus-Boelter Equation cannot be modified to handle the behaviour of supercritical fluids as it both over and under predicts the experimental results simultaneously. This suggests that the physics of the problem are not well understood, and requires additional experimental work to understand the phenomena driving the heat transfer in supercritical fluid.

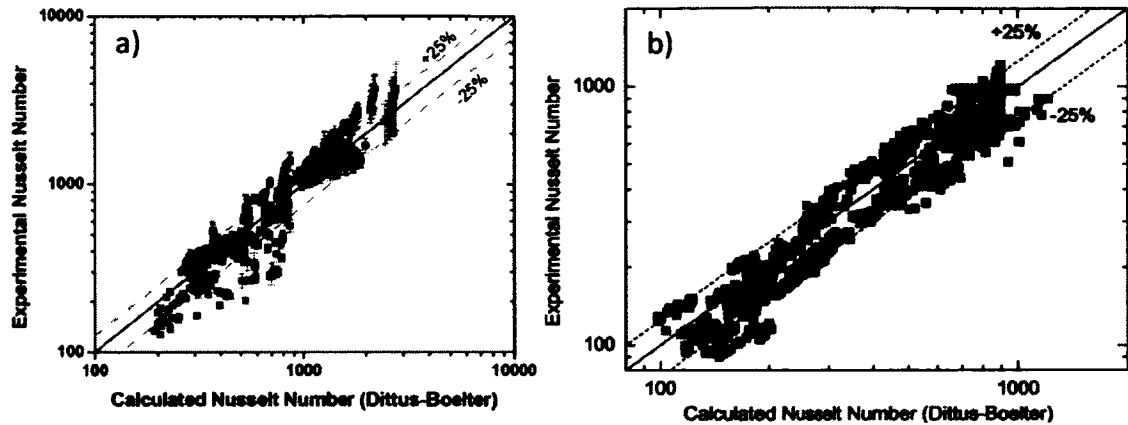


Figure 2-3: "Comparison of experimental Nusselt number and Dittus-Boelter correlation" [7][25]

Many additional correlations have been developed to better capture the heat transfer behaviour of supercritical fluid, with Jackson's (Eqn. 2.9) proving to be the most accurate predictions [7][27]. The Jackson correlation, along with other successful correlations, has the advantage of collapsing to a line when compared to experimental data and demonstrating a consistent bias (Figure 2-4).

$$Nu = 0.0183 Re_b^{0.82} Pr_b^{0.5} \left(\frac{\rho_w}{\rho_b}\right)^{0.3} \left(\frac{\bar{c}_p}{c_{p,b}}\right)^n \quad (2.9)$$

where: Re : Reynolds number based on the inside diameter; Pr : Prandtl number, ρ : density, \bar{c}_p : area averaged specific heat at constant pressure; c_p : specific heat; n : coefficient defined by the temperature gradient as shown below.

Exponent n is:

$$n = 0.4 \quad \text{for } T_b < T_w < T_{pc} \text{ and for } 1.2 T_{pc} < T_b < T_w;$$

$$n = 0.4 + 0.2 \left(\frac{T_w}{T_{pc}} - 1\right) \quad \text{for } T_b < T_{pc} < T_w; \text{ and}$$

$$n = 0.4 + 0.2 \left(\frac{T_w}{T_{pc}} - 1\right) \left[1 - 5 \left(\frac{T_b}{T_{pc}} - 1\right)\right] \quad \text{for } T_{pc} < T_b < 1.2 T_{pc}; \text{ and } T_b < T_w.$$

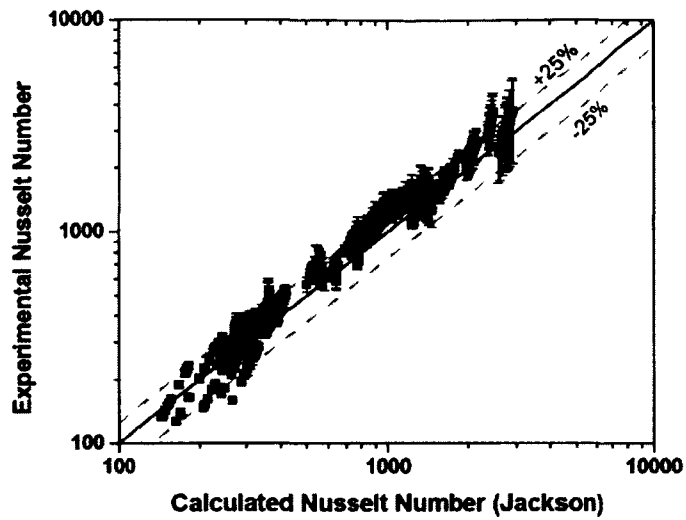


Figure 2-4: "Comparison of experimental Nusselt number and Jackson correlation" [7]

All of the advanced correlations proposed for supercritical fluids with superior accuracy share a common flaw; they are all fit Equations, where there are more assigned constants than independent variables. Examining the generalized form of the Nusselt Equation (Eqn. 2.10) of the considered correlations as presented by Pirot et al versus the table of coefficients (Table 2-2), there are four independent variables and up to seven coefficients. The Jackson correlation, presented above, uses five coefficients.

$$Nu_{t,x} = C_1 Re_{t,x}^{m_1} Pr_{t,x}^{m_2} \left(\frac{\rho_w}{\rho_b}\right)_x^{m_3} \left(\frac{\mu_w}{\mu_b}\right)_x^{m_4} \left(\frac{k_w}{k_b}\right)_x^{m_5} \left(\frac{\bar{c}_p}{c_{p,b}}\right)_x^{m_6} \left(1 + C_2 \frac{D_h}{L}\right)^{m_7} \quad (2.10)$$

Where: Re : Reynolds number based on the inside diameter; Pr : Prandtl number, ρ : density; μ : dynamic viscosity; k : thermal conductivity; \bar{c}_p : area averaged specific heat at constant pressure; c_p : specific heat; D_h : hydraulic diameter; L : heated length

Table 2-2: "Trends in generalizing heat transfer rate at supercritical pressures" [27]

Reference	Flow geometry	Characteristic parameters in Nu , Re and Pr		m_1	m_2	m_3	m_4	m_5	m_6	m_7
		t ($^{\circ}C$)	Length							
McAdams et al. (1950)	Annulus	$t_f = (t_b + t_w)/2$	D_{hy}	0.8	0.33	0	0	0	0	1
Bringer and Smith (1957)	Tube	t_b , t_{pc} or t_w	D	0.77	0.55, t_w	0	0	0	0	0
Shitsman (1959, 1974)	Tube	t_b	D	0.8	0.8, t_b or t_w	0	0	0	0	0
Krasnoshechekov and Protopopov (1959)	Tube	t_b	D	-0.8	-0.33	0	0.11, t_b/t_w	-0.33, t_b/t_w	0.35	0
Svensson et al. (1965)	Tube	t_w	D	0.923	0.613 based on \bar{c}_p	-0.231, t_b/t_w	0.231, t_b/t_w	0	0	0
Kondrat'ev (1969)	Tube, annulus	t_b	D_{hy}	0.8	0	0	0	0	0	0
Ornatsky et al. (1970)	Tube	t_b	D	0.8	0.8, t_b or t_w	-0.3, t_b/t_w	0	0	0	0
Ornatsky et al. (1972)	Annulus	t_b	D_{hy}	0.8	0.4	0	0	0	0	0
Yamagata et al. (1972)	Tube	t_b	D	0.85	0.8 and Pr_{pc}^*	0	0	0	0 or n_1	0
Dyadyakin and Popov (1977)	Bundle	t_b	D_{hy}	0.8	0.7 based on \bar{c}_p	-0.45, t_b/t_w	0.2, t_b/t_w	0	0	1
Kirillov et al. (1990)	Tube	t_b	D	-0.8	-0.33 or 0.4	- n_1	0	0	n_2	0
Gorbun' et al. (1990)	Tube	t_b	D	0.9	-0.12	0	0	0	0	0

Based on the significant amount of hand tuning that is required to capture the experimental data with any of the correlations for a given pressure range, and the significant uncertainty, $\pm 25\%$, that remains in the data, there is little motivation to use a specific correlation for a general code that is required to handle sub- and supercritical fluid. Kays suggests the use of a convenient empirical formula by Sleicher and Rouse for use with gases and higher Prandtl-number fluids for both heating and cooling with either constant heat flux or constant wall temperature, with the applicable range of Prandtl and Reynolds numbers provided with the Equation 2.11, below [26]. The Equation relies on three constants, of which two are dependent on the fluid properties, to predict the Nusselt number over the range of validity.

$$Nu = 5 + 0.015Re^a Pr^b$$

$$a = 0.88 - \frac{0.24}{4 + Pr}; b = 0.333 + 0.5e^{-0.6Pr} \quad (2.11)$$

$$0.1 < Pr < 10^4 \text{ and } 10^4 < Re < 10^6$$

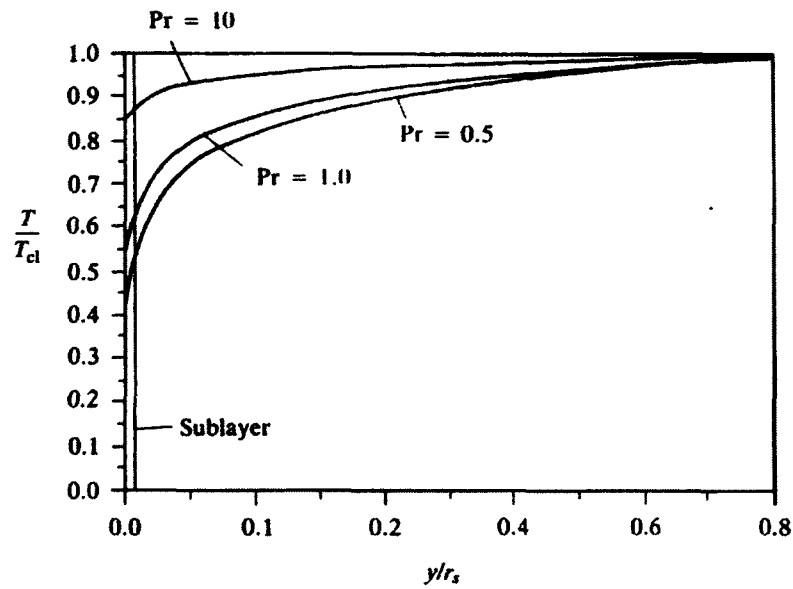


Figure 2-5: “Effect of Prandtl number on turbulent flow temperature distribution; $Re = 100,000$ ” [26]

The Sleicher and Rouse correlation was compared to the Jackson correlation (Figure 2-6) over a wide range of temperatures, for the Carleton supercritical water thermal-hydraulic loop’s typical operating pressure, 28 MPa. The compressibility effects captured by the density ratio ($\frac{\rho_w}{\rho_b}$) for the Jackson correlation were taken from given temperature variation for turbulent flow from Kays (Figure 2-5) to determine the bulk-to-wall density ratio at each temperature [26].

Examining Figure 2-5 it is apparent for turbulent flow that the area averaged specific heat tends to the bulk specific heat value, especially for higher Prandtl number fluids. Therefore, the ratio of specific heat term in the Jackson correlation will be assumed to have a negligible influence and be ignored when using the Jackson correlation.

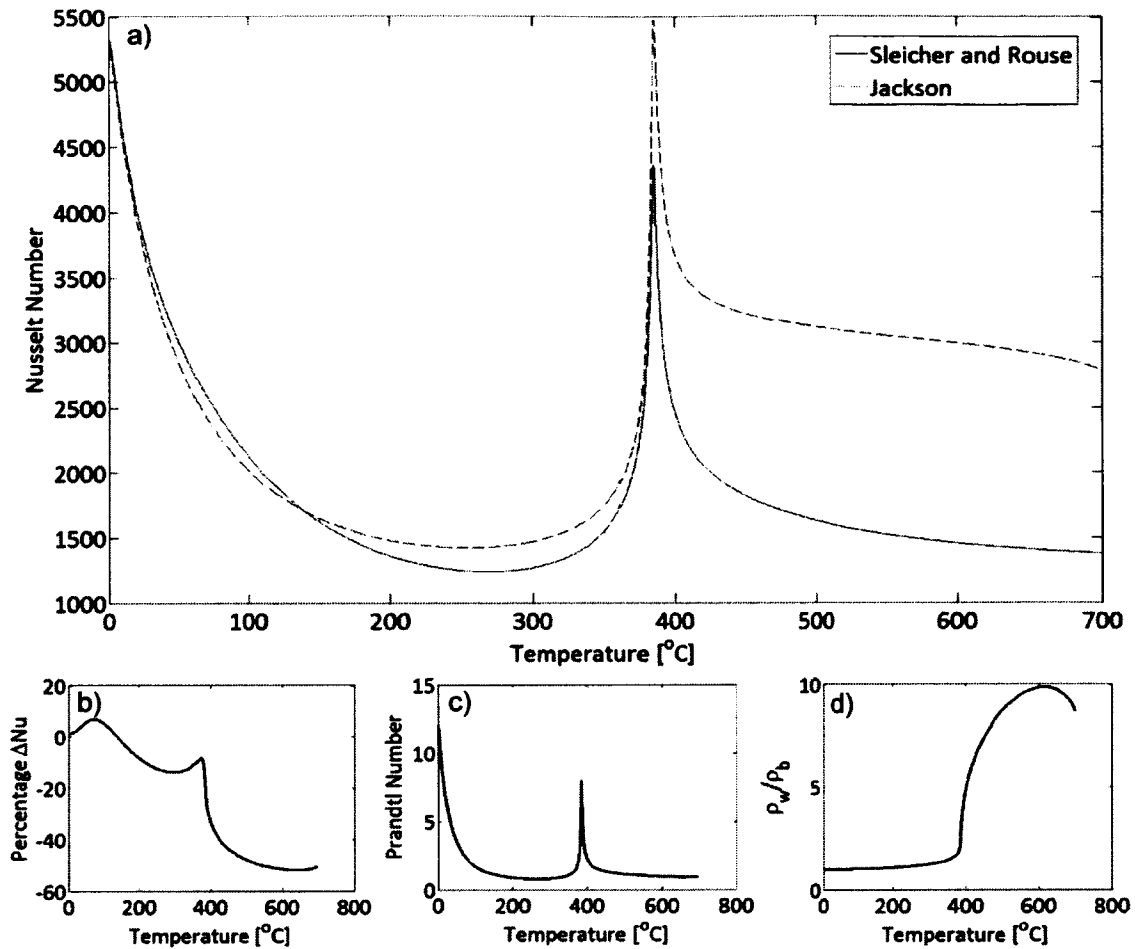


Figure 2-6: Sleicher and Rouse vs Jackson, Nusselt Correlations for $Re = 100000$ at 25 MPa

Comparing the two correlations shown in Figure 2-6, for turbulent sub critical flow, both correlations produce very similar results. Despite having very different forms, where the density ratio remains close to unity, both correlations suggest the same variation with Prandtl number and track in a nearly identical matter. After spiking through the pseudo-critical point, the Prandtl number returns to near unity values while the bulk density drops by nearly an order of magnitude. Based on the turbulent flow temperature profiles (Figure 2-5), the wall temperature can be as little as half the bulk temperature. In this case the fluid's density near the wall will have significantly different properties than the bulk fluid as it transitions through the pseudo-

critical point. The Jackson correlation suggests that a region of enhanced heat transfer will be extended well past the pseudo-critical point, until the temperature profile results in a lower density ratio. Experimental work suggests that once away from the pseudo-critical or critical point, heat transfer effects do not vary significantly from standard liquid or gas behaviour [7][25]. The heat transfer behaviour, based on the Jackson correlation, would expect to be severely degraded in the alternate scenario where the fluid was being heated by the wall, where the fluid density near the wall would drop before the bulk density as the fluid approached the pseudo-critical or critical temperature. This is found to be inconsistent with the data compiled by Diamond from Brookhaven National Laboratory, shown below in Figure 2-7, where the variation of the heat transfer coefficient is dominated by the heat flux rather than the direction of heat transfer, and is maximized prior to reaching the pseudo-critical point while the fluid is being heated [4].

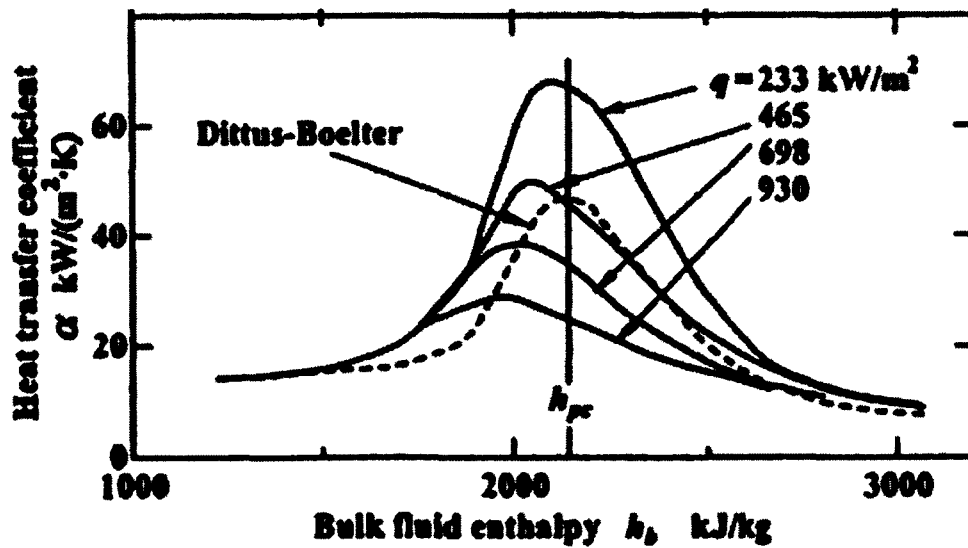


Figure 2-7: "Single-phase heat transfer at prototypical SCWR conditions" [4]

While the Jackson correlation may be well optimized for use with heat transfer scenarios considered by Licht et al. and Li et al. and reviewed by Piore et al., its applicability as a correlation for a general pipeline simulation code remains an open question. Given the recommendation by Kays et al., and the wide range of applicability, the Sleicher and Rouse correlation, while may not be more accurate than the Jackson correlation, provides a more suitable correlation to use for heat transfer effects while the outstanding questions about heat transfer in supercritical fluids are answered. The wide range of proposed correlations and their limited success serve to impress the need to perform additional detailed experiments on heat transfer in supercritical fluids across a wide range of conditions and geometries.

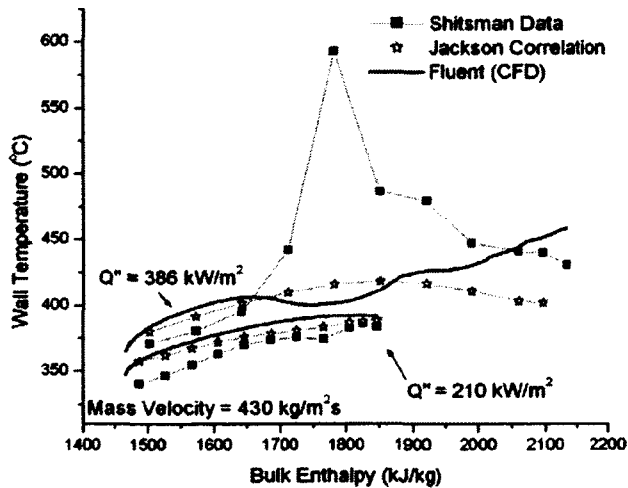


Figure 2-8: "CFD and Nusselt correlation in comparison to Shitsman experiment" [7]

It is worth noting that additional help is not available from the current computational simulations, as they have not proven more successful in predicting deterioration in heat transfer for supercritical fluid with their models[7][28][29][30][31]. Using commercial codes such as Fluent, Figure 2-8, CFX or Stars-CD, Figure 2-9, it has been shown the turbulence modeling, and its accuracy, present the main difficulties when performing numerical analysis of supercritical

fluids. Cheng et al. mention that for capturing the deteriorated heat transfer effects in supercritical flows, while qualitatively the current models provide good agreement with the available experimental data, quantitatively a significant deviation remains between the numerical and experimental results; Licht et al. are more blunt, "this effect has not yet been adequately captured with any CFD method"[7][31].

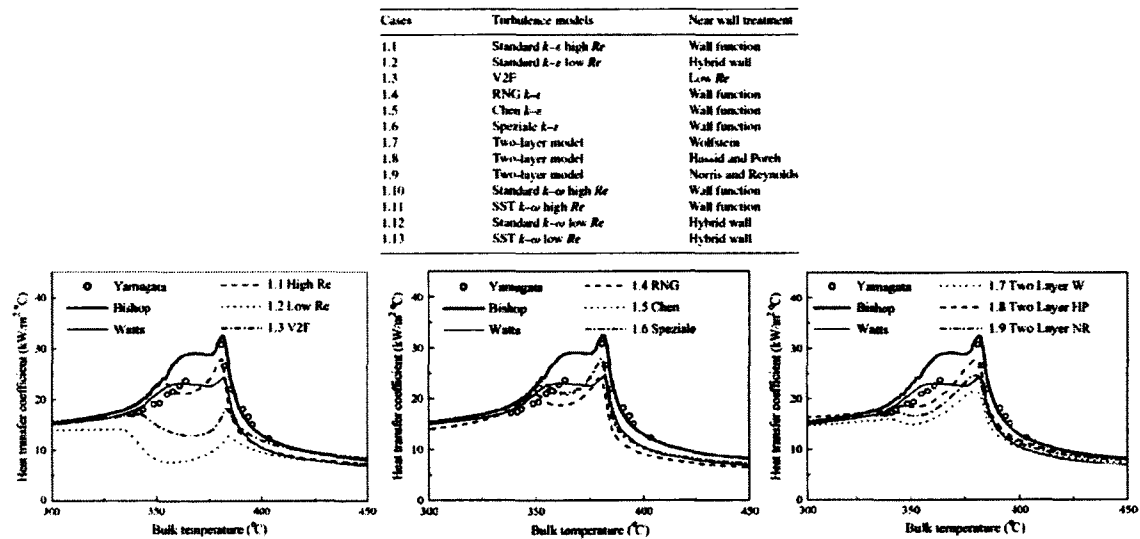


Figure 2-9: "Heat transfer coefficient in the low bulk temperature region" [31]

Yang et al., supported by the other reviewed authors, suggest that the standard $k-\epsilon$ high Re model using the standard wall functions for near wall treatment, show acceptable correlation to the data set they are compared against; at least as good as any of the experimentally derived correlations [28][30][31]. All of the numerical work shares the same limitations as the experimentally derived correlations, namely the data set available for comparison is limited and none of the work accurately captures the deterioration heat transfer effect present in certain flow arrangements.

The limitations of both the numerical analysis and the experimental correlations reinforce the need to carry out additional heat transfer experiments in supercritical fluid over a wide range of flow and geometry configurations to improve the data set available as well as improving the understanding of the underlying physics. To this end, heat transfer studies, both numerically and experimentally, remain an active field of research, and the need to build additional experimental facilities, and develop the tools necessary to support them from design through operation has not abated.

2.3 Test Section Design

A review of the previous and current work regarding the design of a thermal hydraulic test section for use with supercritical fluids will follow in Chapter 6, presented preceding the test section design there within.

Chapter 3 Modeling a Thermal-Hydraulics Loop

To predict the transient thermal behaviour of the proposed supercritical thermal-hydraulic loop a numerical tool was developed with the capability of accurately simulating the transient thermal response of a thermal-hydraulics loop involving heat addition and removal. The modeling of the thermal-hydraulic loop and its thermal behaviour utilizes a number of assumptions based on the geometry and fluid flow field to simplify the numerics. These assumptions, and their validity, are discussed below.

- Axisymmetry exists in every loop component
- The fluid flow field is one-dimensional
- The acoustic terms and advection terms are completely decoupled
- Compressibility effects are purely temperature dependant
- The outer surface of the pipe system is adiabatic

The simplified model used to represent the different components that comprise the thermal-hydraulics loop is shown in Figure 3-1 below. The schematic describes a typical segment of a component, which is subdivided into a solid and fluid domain. The solid domain supports two-dimensional conduction. The fluid domain, which is assumed to be one-dimensional, also supports two dimensional heat transfer through the use of empirical correlations. The thermal-hydraulic loop is to be well insulated, so the exterior of the solid domain is considered to be adiabatic. *The inner surface of the fluid domain, if it exists, is also taken as adiabatic.* This is done to allow the user to independently control the hydraulic diameter and heat transfer surface area, rather than representing a physical interface that would provide a heat transfer path. Each domain is established by a number of parameters that allow their transient thermal behaviour to be fully characterized. The fluid domain's geometry is defined by an annular configuration, with the radius ratio (Eqn. 3.1) varying from zero to one. The outer radius (r_o) is set to match the desired heat transfer area, and the inner radius (r_i) is used to set the hydraulic

diameter. To represent a circular cross section, such as a pipe, the inner radius is set to zero. The fluid's properties defining the thermodynamic state are defined at the center of the fluid segment, while the fluid velocity is defined at the segment's inlet and outlet. The solid domain is defined by adding an appropriate thickness of the appropriate material around the fluid domain. The temperature distribution of the solid domain is tracked, and the remaining properties derived as necessary on the basis that they are purely a function of temperature.

$$r^* = \frac{r_i}{r_o} \tag{3.1}$$

where: r_i : pipe inner radius; r_o : pipe outer radius

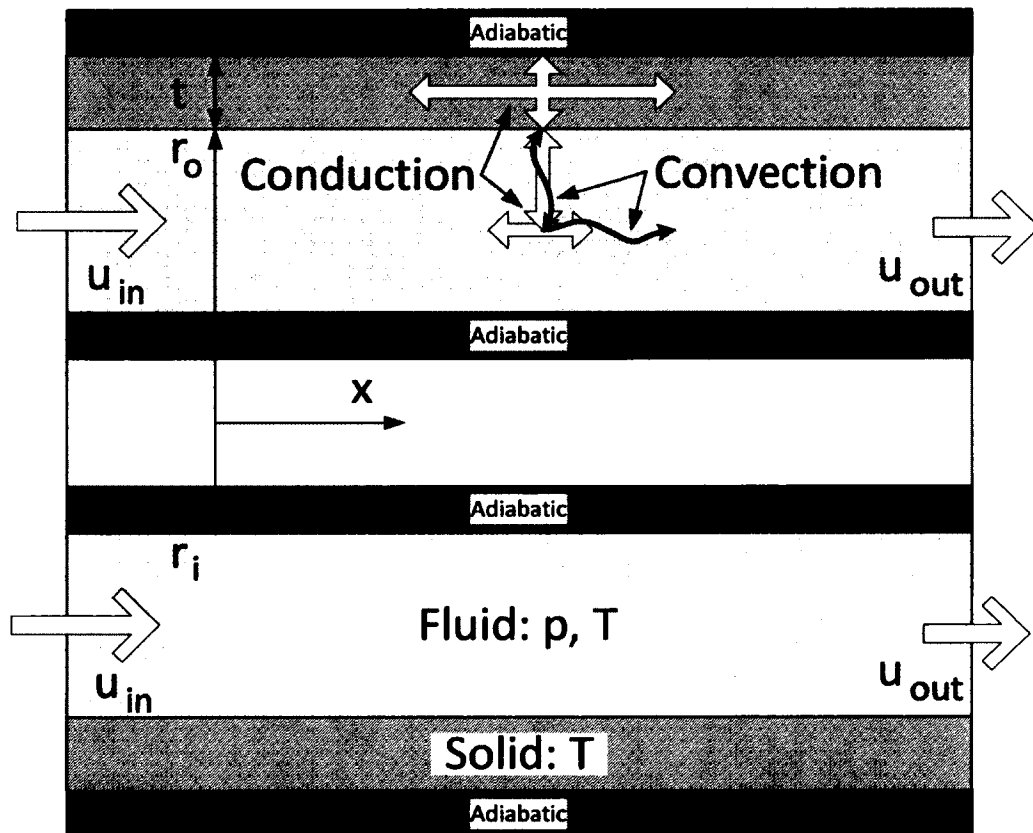


Figure 3-1: General Component Segment Model

The methodology of defining the geometry and primitive variables in this way will be described in Section 3.4 below. The model representing the thermal-hydraulic loop yields a multi-physics

numerical solver that is capable of simulating time dependant, two dimensional heat transfer effects, including conduction and convection, and time dependant, one dimensional fluid flow.

3.1 Numerical Methods

With a strict focus on the transient thermal response of the thermal-hydraulics loop, the system of Equations may be dimensionally reduced while still providing sufficient detail of the system's behavior. This approach reduces computational demands, and simplifies aspects of the simulation by eliminating issues arising from turbulence modeling and complex flow field modeling. In exchange for these simplifications a different set challenges must be addressed to ensure accuracy in the numerical results. Some of these issues, such as heat transfer correlations, require additional experimental work to improve the accuracy of the tools (discussed in Chapter 4). Others, such as the *decoupling of the acoustics and advection* or ensuring the boundedness of compressible Navier-Stokes systems in one dimension, need to be addressed.

Compressibility of a substance is defined by its relative volume change as a response to a pressure change at constant temperature. In fluids, due to their ability to rapidly modify their state and physical shape, this effect is typically classified by the fluid's velocity in relationship to the speed at which information propagates (local speed of sound) in the fluid, defined by the Mach number. Where the fluid's velocity is sufficiently lower than its speed of sound, the entire fluid field will respond to accommodate a local pressure perturbation, rather than see a localized change in density. In this situation the advection terms (velocity) are considered decoupled from the acoustic terms (information propagation at the speed of sound), and the fluid is classified as incompressible. Nonetheless, low-speed flows with variable density exist where large variations in temperature occur, such as in a strongly heated flow, or in the case of

supercritical fluid, even with small temperature or pressure fluctuations near the critical or pseudo-critical point. In these flows, compressibility effects must be accounted for despite the large disparity between advection and acoustic speeds. This disparity results in an increased stiffness of the numerical problem when using the fully compressible Navier-Stokes Equations [32]. This increased stiffness can be handled by using high order methods to improve accuracy in regions where strong gradients exist or by reducing the grid size until it matches the stiffness of the numerics to capture these gradients [32][33][34] [35][36]. As described below, an explicit method was chosen for the solver, which resulted in a grid with sufficient stiffness to handle the compressibility effects despite the advection and acoustic decoupling.

The algorithm used to solve the discretized set of Equations (see Section 3.7 below) necessitates the use of split leading and lagging variables in the explicit Equation. While each Equation remains fully explicit, due to the coupling of the momentum and mass conservation Equations, the solution becomes semi-implicit with an iterative solution. To ensure the problem remains bounded with a singular solution, the work of Mucha, and Jiang et al. was used [37][38]. Mucha proves the asymptotic behaviour of a compressible, viscous, barotropic one dimensional system, and the global boundedness for a Neumann boundary condition [37]. The work applies to atmospheric science, however can be directly related to the numerical model developed herein. As the temperature field is solved initially (a leading variable) and then held constant through the iterative portion of the solution, the system can be treated as barotropic through the iterations. The interface between the fluid and the surrounding wall employs the Neumann boundary condition conserving the heat flux at the cell interface. Therefore, the system of Equations developed below meet the criteria of his model and as such his proof of universal boundedness of the solution may be applied to the present iterative solver. Jiang et al. explore the asymptotic behaviour of a one dimensional, compressible, heat-conducting fluid where the

viscosity and heat-conduction tend to zero [38]. They show that for discontinuous initial data there is a time-asymptotic state for the solution. This provides a lower bound for the vanishing limit of viscosity and heat transfer, ensures that a unique solution exists, and that the solution will not diverge, even through the entire critical region where near-zero values exist for fluid properties.

Based on the literature reviewed, the reduced set of Equations should prove capable of accurately simulating the thermal response of the system to within the limits of the chosen correlations.

3.2 Fluid Modeling

The behaviour of a Newtonian fluid is described by a set of Equations commonly known as the Navier-Stokes Equations. Together they comprise of the three conservation Equations for mass, momentum and energy. Their derivation and general application lies outside of the scope of this work; the reader is directed to any introductory fluid dynamics or computational fluid dynamics text for their derivation [22][39]. The transient thermal behavior of the thermal-hydraulic loop is the primary focus and so the interest in the fluid flow is restricted insomuch. To simplify the problem, the fluid flow in the thermal-hydraulic loop will be treated as one dimensional. The radial symmetry of the components and pipe flow path inherently reduce the dimensional order of the problem. Gradients in the radial direction are treated using well established correlations to derive the pertinent results such as pressure drop and heat transfer without having to calculate the gradients. This approach also removes the need for turbulence modeling. Thus the conservation Equations will be limited to their one dimensional form, which for cylindrical coordinates, along the major axis, reduce to:

$$\text{Mass Conservation: } \frac{\partial \rho}{\partial t} + \frac{\partial}{\partial x}(\rho u) = 0 \quad (3.2)$$

$$\text{Momentum Conservation: } \frac{\partial(\rho u)}{\partial t} + u \frac{\partial u}{\partial x} - \frac{1}{r} \frac{\partial}{\partial r} \left(r \mu \frac{\partial u}{\partial r} \right) - \frac{\partial}{\partial x} \left(-p + \frac{2}{3} \mu \left\{ 2 \frac{\partial u}{\partial x} - \frac{u}{r} \right\} \right) = \rho f_x \quad (3.3)$$

$$\text{Energy Conservation: } \frac{\partial E_t}{\partial t} - \frac{\partial Q}{\partial t} + \frac{\partial}{\partial x} \left(E_t u + p u - u \tau_{xx} + \frac{\partial}{\partial x} (-k \nabla T) \right) = \rho f_x u \quad (3.4)$$

where: ρ : density; t : time; u : velocity; p : pressure; μ : dynamic viscosity; f_x : body force; E_t : total stored energy; Q : heat addition; τ : shear stress; k : thermal conductivity; T : temperature; the coefficient of bulk viscosity is assumed to be zero, thus the second coefficient of viscosity becomes $\mu' = -\frac{2}{3}\mu$.

The system may be treated as acoustically incompressible, due to the low Mach number across all operating conditions. Since the Mach number will never exceed 0.04, the acoustic response around the loop will be effectively instantaneous compared to the advection terms. Comparing the loop's total flow path length of approximately 17.5m to the fluid's speed of sound around the loop, as given in Table 3-1, shows that any transient pressure fluctuation will propagate around the loop faster than the imposed time step (see Chapter 5), and therefore appearing instantaneous. The acoustic effects on compressibility due to the thermal excitation of the fluid are also insignificant compared to the effects of pump; therefore, the acoustic effects on compressibility and the pressure field may be ignored without loss of accuracy.

Table 3-1: Loop Acoustic Data

Typical Average Speed of Sound	Typical Average Fluid Velocity	Acoustic Propagation Time	Advection Propagation Time
840 [m/s]	4.5 [m/s]	0.02 [s]	3.8 [s]

With the fluid being treated as incompressible based on the Mach number, and local acoustics being ignored, compressibility effects become dependent on heating alone. Therefore density changes in time are a function of the Equation of state only, with the required temperature information solved for by the energy conservation Equation, shown below. Given the volumetric flow rate is a known parameter at the pump exit, the velocity, and subsequently the mass flux there is known, allowing the mass conservation Equation to update the velocity field.

The simplification of the acoustics has the additional advantage in that the pressure gradient around the loop becomes a pure function of friction effects. In the inviscid limit, since any pressure fluctuations are propagated instantaneously, the loop's pressure is uniform and purely dependant on the Equation of state. This allows for the replacement of the conservation of momentum Equation (Eqn. 3.3) with a one dimensional form defining the pressure gradient due to friction effects while ignoring height change (Eqn. 3.5, 3.6) [22].

$$\frac{dp}{dx} = f \frac{\rho u^2}{2D_h} \quad (3.5)$$

$$\frac{1}{f^{1/2}} = -2.0 \log \left(\frac{\frac{\epsilon}{D_h}}{3.7} + \frac{2.51}{Re D_h f^{1/2}} \right) \quad (3.6)$$

where: ρ : density; u : velocity; p : pressure; D_h : hydraulic diameter; f : friction factor; Re : Reynolds number; ϵ : surface roughness.

The friction factor (Eqn. 3.6) is an interpolation formula by Colebrook which combines both the derived laminar and experimental turbulent results [22]. The solution of the friction factor is typically plotted as the familiar Moody chart for pipe friction to avoid having to iterate when using the formula. The results of the formula are accepted for design calculations and will be used to determine the frictional effects for one dimensional flow simulation. Therefore by coupling the Equation of state and the pressure gradient due to frictional losses, the mass and momentum conservation Equations (Eqn. 3.2, 3.3) may be solved for iteratively by assuming the temperature remains constant over the course of the iteration.

The pressure loss due to friction around the loop is equal to the heat generation due to viscous effects (Eqn. 3.7); the pumping power required for a given flow rate is the sum of viscous heating. Comparing the maximum required pumping power to the power input at the test section the viscous effects in the energy conservation Equation (Eqn. 3.4) are insignificant and may be ignored.

$$\dot{Q}_{viscous} = \Delta p \dot{V} \quad (3.7)$$

where: \dot{Q} : heat rate; p : pressure; \dot{V} : volumetric flow rate.

Table 3-2: Viscous Heating Data

Max Pump \dot{V}	Max Δp	Max Pump Power	Test section Power Delivery
1.55e-4 [m ³ /s]	0.57 [bar]	8.8e-3 [kW]	300 [kW]

Using the convective heat transfer coefficient, developed in Appendix A, to account for heat transfer in the radial direction, and ignoring the viscous heating effects, the energy conservation Equation may be replaced with the Equation for the first law of thermodynamics for a one-dimensional open system (Eqn. 3.8) as demonstrated in Appendix B.

$$\frac{\partial E}{\partial t} = \sum -k \frac{\partial T}{\partial x_i} dA_i + \sum h_{conv} (T_{s_j} - T_{\infty}) dA_j + \dot{Q}_{source} + \sum \dot{m} \left(h + \frac{u^2}{2} \right) \quad (3.8)$$

where: E : energy; t : time; k : thermal conductivity; T : temperature; A : area; h_{conv} : convective heat transfer coefficient; \dot{m} : mass flow; \dot{Q} : heat rate; h : specific enthalpy; u : velocity.

3.3 Solid Material Modeling

The solid material comprising the piping walls and components is assumed to be homogeneous. The heat transfer effects are limited to conduction internally resulting in a two dimensional diffusion Equation to capture the heat transfer. Applying Gauss' law yields a similar Equation to the fluid field (Eqn. 3.8), without the convection terms. Neither work nor advection applies to the solid material so these terms are neglected entirely. The resulting time dependant energy Equation (Eqn. 3.9) is used in favour of the classic heat Equation to retain internal consistency between the fluid and solid domain solvers.

$$\frac{\partial E}{\partial t} = \sum -k \frac{\partial T}{\partial x_i} dA_i \quad (3.9)$$

where: E : energy; t : time; k : thermal conductivity; T : temperature; A : area

3.4 Discretization and Numerical Stability Analysis

When deciding on a discretization scheme an initial choice between an explicit or implicit method must be made. Many modern computational schemes and commercial programs favour implicit schemes for their unconditional stability allowing for larger step sizes and potentially reducing total computational time. Implicit schemes have the disadvantage that they require the entire solution matrix to be inverted as the system as a whole is determinant, rather than each cell. Establishing the coefficient matrix and conditioning it for inversion adds coding complexity to the problem. The size of the solution space is also limited by the available RAM to store the matrices and perform the inversion. Explicit schemes have the advantage of each cell being determinant as the solution relies only on previous in time information. These schemes are simpler to implement, however have the disadvantage that they are only conditionally stable. Their conditional stability restricts the maximum permissible time step for a given discretization scheme. Stability considerations will be investigated in detail below.

Implementation of the numerical simulation was chosen to occur in the program Matlab. Matlab is a technical computing software package initially designed to specialize in handling complex linear algebra. The Matlab environment has its own programming language that is based on the Java environment that Matlab runs in. Code written in the Matlab language is compiled and run in the Matlab environment. Matlab has been extended to handle fully parallel and distributed computing. The Matlab environment was chosen to implement the numerical simulation as it has robust linear algebra math libraries well suited to solving the numerical simulation proposed, and the author was familiar with code development in the Matlab language. As Matlab is a standard academic software package, the requirement for the simulation to run inside the Matlab environment is not seen as a limitation to the numerical simulations generality.

The choice of development environment factored into the choice of discretization schemes, as Matlab is a vector math program, the difference in implementing either a implicit or explicit method is minimized. For reasons that are outside the scope of this work, Matlab requires computations over the solution space (mesh) to be vectorized for the solver is to remain efficient. The determining criteria was the desire to capture the transient behaviour of the system, which requires a fine resolution in the time domain. Since the time step size was chosen to capture transient phenomena, the advantage of using an implicit scheme would not be realized. An explicit scheme for the numerical solver was chosen since its stability limitations would not impose an additional computational penalty on the solution time, and the simplification of the solution algorithm resulting from using an explicit scheme proved desirable compared to an implicit scheme. The density-pressure field is a coupled system solved for explicitly, while the conservation of mass is used to solve for the resultant velocity field explicitly as well. Since the pressure field is derived from the head losses, it is dependent on the velocity field and therefore the density-pressure field becomes coupled with the velocity field, resulting in a semi-implicit solution. While each solution step remains explicit, the coupling creates a weakly implicit set of Equations that are subsequently solved by iterating on the explicit solutions until converging to a solution that satisfies the coupled implicit set of Equations. The scheme is similar to the iterative time-advancing scheme described by Kim et al. [40].

3.4.1 Discretization of Governing Equations

Examining the partial differential Equations in the governing Equations for both the fluid and solid domains (Eqn. 3.8, 3.9), they are limited to first order in space and time. Given their low order in space, the spatial discretization is limited to the Euler Explicit method. Given non-uniform grid spacing and linear gradients, the diffusion terms may only be between two adjacent nodes. Figure 3-2 shows a general node distribution for a solid medium. The

temperature gradient between nodes in the solid is limited by the first order heat conduction

Equation (Eqn. 3.10), so there is no physical difference between tracking the temperature at the nodes or their faces.

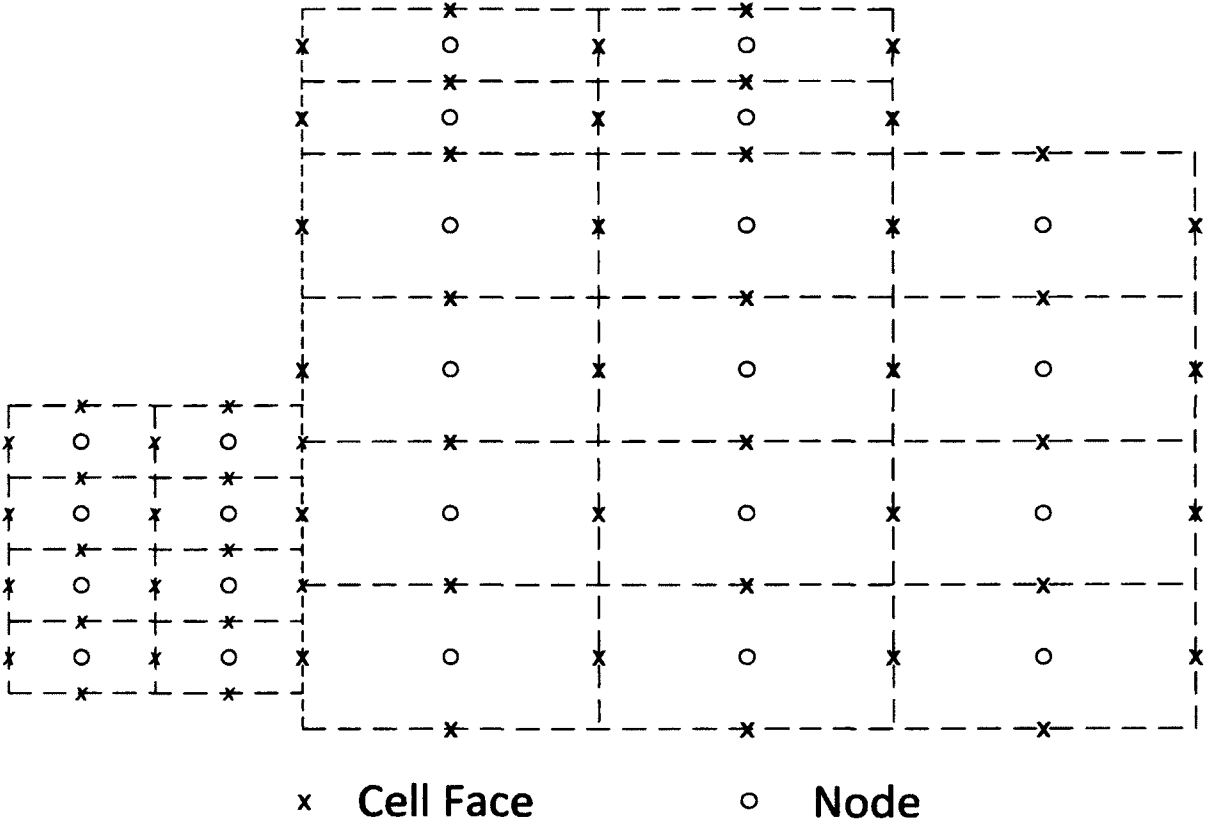


Figure 3-2: General Node Distribution for a Solid Material

Given that the cells need not be equal-sized nor uniformly distributed, to simplify book keeping, the temperature values are stored at the nodes, so the flux is determined from node to node as shown in the discretized form of Fourier's law (Eqn. 3.10). Additional conditioning is used to accurately capture the flux between cells of different face size, which is detailed below in the description of the solution algorithm.

$$\dot{q}''_{cond} = -k \frac{T_{i+1} - T_i}{\frac{1}{2}(\Delta x_{i+1} + \Delta x_i)} \quad (3.10)$$

where: \dot{q}'' : specific heat flux; k : thermal conductivity; T : temperature.

Storing the temperature at the mid cell nodes is also advantageous since for turbulent flows (see Figure 2-5) the centerline temperature is a good approximation of the bulk temperature.

The node temperature, representing the bulk temperature, can then be used accurately for determining fluid properties, such as enthalpy, for advection heat transfer. For these reasons, all fluid properties are stored at the node and, except for temperature, considered uniform, as the average value, across the fluid cell. The affect of this will be investigated in the grid independence study. The remaining fluid information, specifically velocity and its dependants, is stored as face values. This is appropriate since they pertain primarily to a flux at the face. Where it is necessary for a node value to be used at a face, or vice versa, the value is assumed to vary linearly node-to-node or face-to-face.

Given the discretization scheme chosen, Euler explicit, time discretization uses a simple one step method, shown in Equation 3.11. The energy term itself is of little interest, and is therefore replaced with the definition of energy in terms of temperature, mass and specific heat capacity (Eqn. 3.12).

$$\frac{\partial E}{\partial t} = \frac{E_i^{n+1} - E_i^n}{\Delta t} \quad (3.11)$$

$$\Delta E = (Tmc)_2 - (Tmc)_1 \quad (3.12)$$

where: E : energy; t : time; T : temperature; m : mass; c : specific heat capacity

The specific heat capacity is a function of temperature, and for fluid cells, the mass as well, since it is dependent on the pressure, which defines the fluid density along with temperature.

Implementing Equation 3.11 directly would then change the scheme to implicit as the temperature at time step $n+1$ would have to be known for the specific heat capacity, and

possibly other variables, to solve Equation 3.8 and 3.9. Since the properties are assumed to remain constant over the time step for the right-hand terms of Equation 3.8 and 3.9, the same assumption can be applied to the properties in the left-hand terms without changing the accuracy of the discretization. By holding the mass and specific heat constant over the time step, the modified form of the change of energy is used to isolate the desired change of temperature term (Eqn. 3.13).

$$\Delta E = \Delta T m c \quad (3.13)$$

Applying the discretization scheme in space and time shown above to the fluid and solid governing Equations yields their discretized form shown below. These Equations have truncation errors of $O[\Delta t, \Delta x]$ and are first-order accurate.

$$\frac{\rho_i^{n+1} - \rho_i^n}{\Delta t} + \frac{(\rho u)_{i-1}^{n+1} - (\rho u)_i^{n+1}}{1/2(\Delta x_{i-1} + \Delta x_i)} = 0 \quad (3.14)$$

$$\frac{p_{i-1}^n - p_i^n}{1/2(\Delta x_{i-1} + \Delta x_i)} = f_i \frac{\rho_{face} u_i^2}{2D_h} \quad (3.15)$$

$$\begin{aligned} \frac{(T_i^{n+1} - T_i^n) m c p_i}{\Delta t} = & -k_i \frac{T_{i-1}^n - T_i^n}{1/2(\Delta x_{i-1} + \Delta x_i)} dA_i - k_i \frac{T_{i+1}^n - T_i^n}{1/2(\Delta x_{i+1} + \Delta x_i)} dA_{i+1} + h_{conv} (T_{s_i}^n - T_i^n) dA_j + \\ & \dot{m}_i \left(h_{i-1}^n + \frac{(u_i^n)^2}{2} \right) - \dot{m}_{i+1} \left(h_i^n + \frac{(u_{i+1}^n)^2}{2} \right) + \dot{Q}_{source} \end{aligned} \quad (3.16)$$

where: E : energy; t : time; k : thermal conductivity; T : temperature; A : area;
 h_{conv} : convective heat transfer coefficient; \dot{m} : mass flow; \dot{Q} : heat rate; h : specific enthalpy;
 u : velocity; n : time step.

3.4.2 Stability Analysis

Having settled on an explicit scheme, a von Neumann stability analysis was performed on selected explicit schemes for the two-dimensional heat Equation. The Explicit Euler, with known stability criterion, was compared to the DuFort-Frankel method (Appendix C) [39]. For a detailed explanation of the procedure used in the von Neumann stability analysis the reader should refer to an introductory computational fluid dynamics text, such as that of Anderson, *Computational Fluid Mechanics and Heat Transfer* [39]. The Explicit Euler is a one-step, single time level

method. DuFort-Frankel's method is a higher order method using a modified one-step, three time level method. The local spatial term to be solved is replaced with a time averaged term that modifies the spatial discretization compared to the Euler method.

The stability criterion for the two-dimensional Dufort-Frankel method cannot be expressed as a convenient equality like the simple explicit case (Eqn. 3.17) shown below. Stability for the Dufort-Frankel method is better represented graphically as developed in Appendix C.

$$\alpha\Delta t \left[\frac{1}{(\Delta x)^2} + \frac{1}{(\Delta y)^2} \right] \leq \frac{1}{2} \tag{3.17}$$

where: α : thermal diffusivity; t : time.

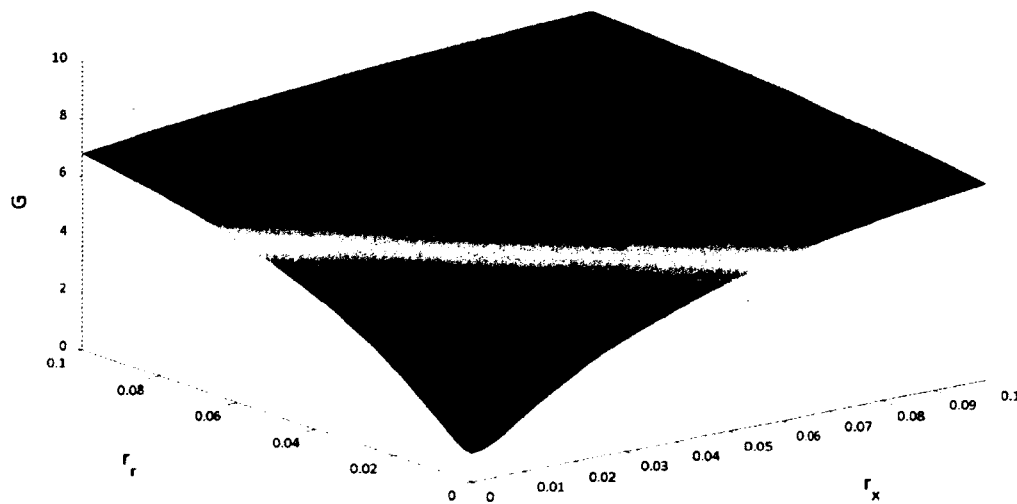


Figure 3-3: Magnitude of Stability Criterion for the limiting values of β_1 and β_2 for the Two-Dimensional DuFort-Frankel Method

As can be seen in Figure 3.3, the two dimensional Dufort-Frankel Method becomes unconditionally unstable, as the stability criterion is greater than one for any grid size greater than zero. While higher-order methods can be desirable for their higher-order accuracies, the increased complexity in determining their universal stability, as well as the potential change from unconditionally stable to unconditionally unstable when transitioning from one-

dimensional to two-dimensional, can result in a low order method more suitable. The problems discussed above prompted the Explicit Euler method to be the preferred choice in the present instance.

3.5 Modeling and Meshing of Loop Components

The loop is divided into two major classes, components and piping. The components are modeled with priority given to match their thermal inertial and heat transfer characteristics. Component's geometries are simplified to reduce computational resource requirements and time while simplifying user input. The piping runs are precisely modeled both in geometry and heat transfer characteristics.

Components use the simplified geometry of an annular tube, with the allowance of having an inner radius of zero. This allows the user to accurately model the component's hydraulic diameter and surface area for heat transfer without having to generate a complex mesh; the inner surface of the annular tube is treated as adiabatic to provide the necessary control. The component's length remains an independent variable, allowing the user to use the component's true flow path length, with the tube's outer wall thickness being defined by the appropriate mass relating to the component's thermal inertia.

The entire loop is covered in sufficient insulation to treat any surface exposed to the atmosphere as adiabatic. This defines the general exterior boundary condition for each part unless otherwise specified.

3.5.1 Piping Modeling

Piping runs are defined by uniform lengths of pipe broken up with features of varying thickness and internal diameter. To capture the thermal inertia of the loop, the additional mass and its

distribution due to these features needs to be modeled accurately. The features include joints and flanges, along with elbows, valves and sensor housings. Shown in Figure 3-4, the features can include complicated geometry with curves and blends. Representing the geometry as manufactured would require an advanced meshing tool and unnecessary computational resources. A simplified version of the geometry is capable of accurately representing the thermal inertia and heat transfer characteristics of the piping feature. Since no stress analysis is being done on the model, the change in geometry will have no impact on the quality of the results. To achieve similarity between the actual part shown at the top of Figure 3-4 and the modeled feature in the piping run, an appropriate distribution of mass is added to the modeled piping run. Along the entire length of the run, the wall thickness may be considered constant, with any additional thickness being described locally where appropriate. Demonstrated in Figure 3-4 below, at the location where a butt weld hub is used to join a pipe length to another part, there is a variation in wall thickness and internal diameter. Starting at the origin of the local coordinate system, the wall thickness at the flange joint is greater than in the pipe wall, while the internal diameter is also significantly greater. The flange is modeled as a 'component' separately from the rest of the pipe, represented in the backwards hash shading in Figure 3-4. This allows for the length, thickness and increased inner diameter to be modeled precisely. After length x_1 , the butt weld hub's outer diameter has a step change reduction followed by a taper to the pipe's outer diameter. Show in Figure 3-4, the added thickness (y_2) between the flange and pipe (x_2) models the part's thermal inertia precisely.

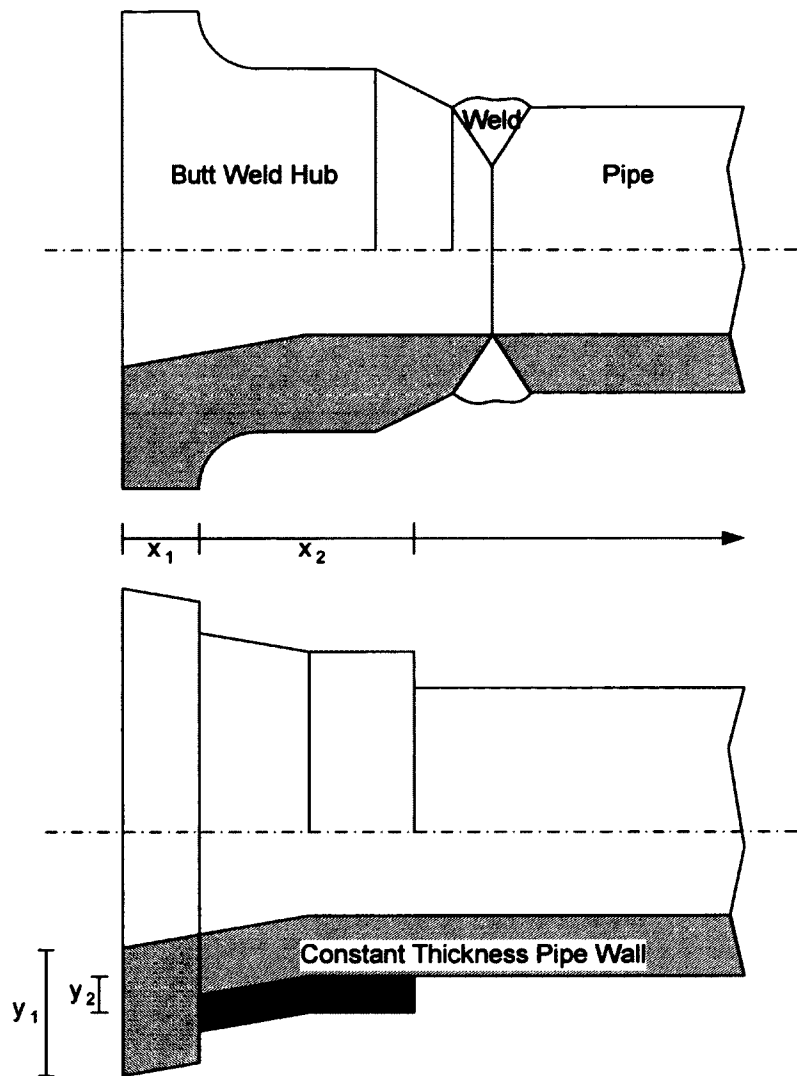


Figure 3-4: Feature Modeling of a Butt Weld Hub and Pipe

The precision using a constant-thickness addition can be set by the user by controlling x_2 and y_2 to cause areas A, B, C, and D in Figure 3-5, to sum to zero. The software developed herein this work linearly blends different internal diameters between components and piping segments, creating a smooth transition. Interchanging component and pipe segments this way allows an accurate model of a piping run's thermal inertial and heat transfer characteristics to be quickly and easily generated by the user for the numerical solver.

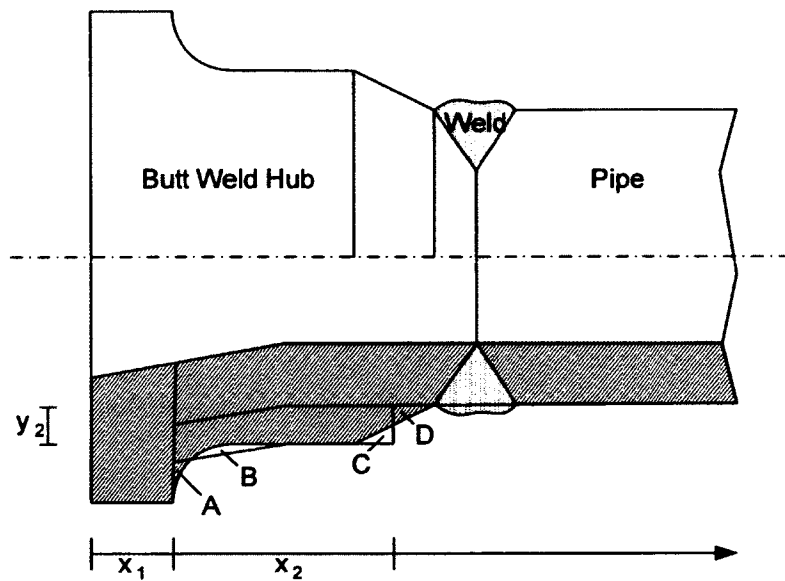


Figure 3-5: Determining Additional Thickness Distribution for Piping Features

3.5.2 Component Modeling

Test sections

The loop is designed to investigate three different types of test sections, namely tubular, annular and rod bundles. Each of the test section designs are described in detail in Chapter 5. For the purpose of the thermal modeling of the entire loop, their defining characteristics are sufficient to achieve the necessary simulation accuracy. Both the tubular and annular test sections can be described exactly by the component modeling scheme.

The tubular test section has a uniform wall thickness with the pressure vessel also acting as the resistive heating element. The unheated and heated sections are geometrically identical. The heated section has a uniform heat source applied though the wall to represent the resistive electric heating. The inlet and outlet blocks, since they are unheated and have an uneven mass distribution, are best modeled as an additional set of piping parts. The inlet and outlet blocks are also common between each test section.

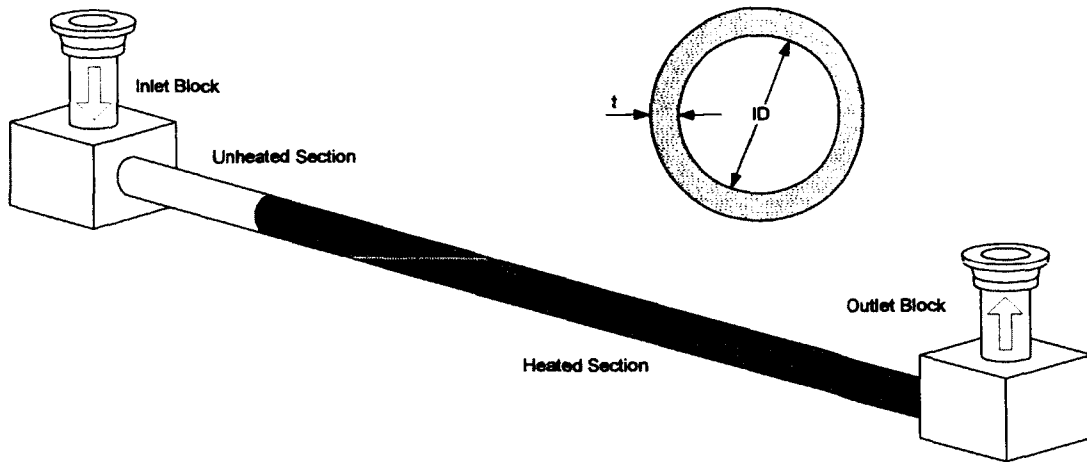


Figure 3-6: Tubular Test section Schematic

The annular test section's geometry can also be directly modeled by the components modeling scheme. The outer pressure vessel is unheated for the annular test section, with the internal rod providing the resistive heating element. Due to the design of the test section's internal rod, stray heat transfer from the heating element to the atmosphere is negligible. This gives an adiabatic internal boundary condition, resulting in all the generated heat being transferred directly to the fluid. The computational model is not designed to provide a detailed investigation of the heat transfer process, which is the purpose of the test sections. Given that all the heat generated is transferred to the fluid, and the fluid simulation is one dimensional, the heat source in the modeled annular test section is assumed to occur directly in the fluid. Based on the adiabatic and one dimensionality assumptions, this does not affect the validity of the simulation, while simplifying the computation.

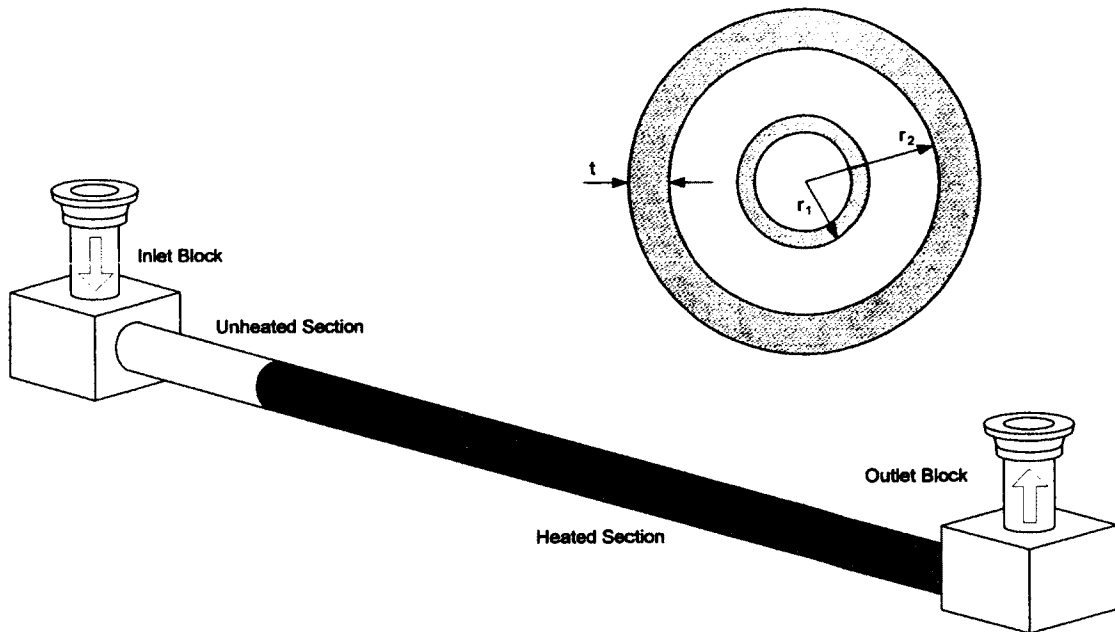


Figure 3-7: Annular Test section Schematic

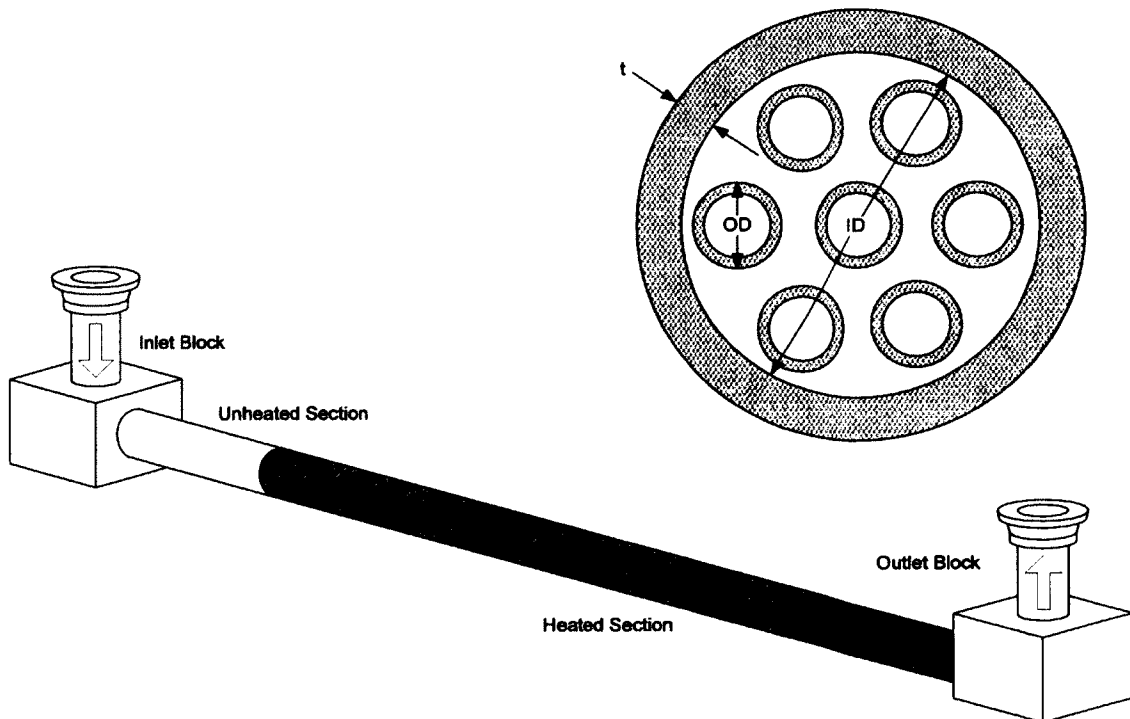


Figure 3-8: 7 Rod Bundle Test section Schematic

A rod bundle configuration of the test section is more complicated using an annular component geometry than either of the previous test section designs. However, given the same assumptions of one dimensional flow and inner surface of the rods being adiabatic, allows the test section to be represented accurately as an annular tube for the simulation. The simplifications result in only the inner surface area of the pressure vessel being of interest for heat transfer effects with the fluid, while the fluid's heat transfer characteristics defined by the geometry, as characterized by the Reynolds number, are captured with the use of a proper hydraulic diameter. Since both of these variables are independently controlled by the component modeling scheme, for the phenomena of interest in the simulation, there is no loss of accuracy modeling a rod bundle this way.

Heat Exchanger

The heat exchanger used in the thermal-hydraulics loop is a shell-and-tube type with a U-bundle arrangement as shown in the schematic below. The heat exchanger design and construction was contracted out, so the design and performance characteristics are fixed for the simulation.

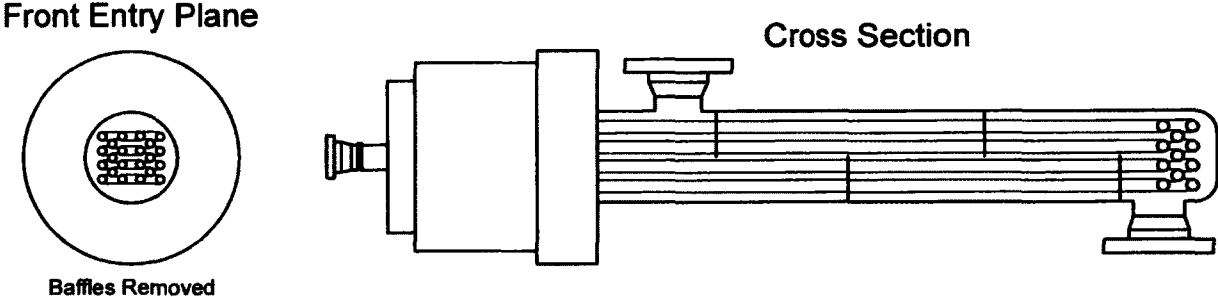


Figure 3-9: Heat Exchanger Schematic

The U-bundle and baffle arrangement results in a complex flow field with complex heat transfer. Both the hot and cold streams on the loop side run parallel such that the cooling flow initially contacts the hot entrance and cold exit simultaneously. The cooling flow continues to cool both

streams in parallel as it progresses along its flow path before exiting at the end of the heat exchanger. The software is limited to handling a single pass design for cooling fluids, as it does not have the capability to simulate three dimensional flows. Accurate handling of the loop side stream is possible using the component model, setting an appropriate heat transfer area and flow area along with the correct flow path length; however, as the performance of the heat exchanger is known, it is more desirable to match that for a thermal simulation, instead of respecting the loop-side flow geometry. To capture the heat exchanger's performance while respecting the thermal inertia the loop experiences due to the heat exchanger, the area available for heat transfer on the loop side must be adjusted. Holding the mass, length and hydraulic diameter of the bundle constant, the area for heat transfer was varied until the desired performance, specified by the manufacture, was met [41].

The cold side flow is modeled to match either the heat exchanger's steady state inlet condition or a stagnant, pre-start-up state. This allows the user to set a conditional start temperature for the loop fluid exit temperature before the heat exchanger is turned on while capturing its thermal inertia. The cold side flow and structure uses the same thermal model and discretization as developed for the rest of the loop.

Pump

The pump chosen is a sealless centrifugal pump from Klaus Union. Seen in the cut away of the pump, Figure 3-10, the flow path consists of a constant area duct leading to the inducer, the impeller itself, and finally through the volute to the constant area discharge nozzle. Both the inlet duct and discharge nozzle are constant area and as such can be modeled as simple pipes. The impeller and volute represent a significant challenge in precisely modeling the pump's thermal inertia due to the impeller's highly complex geometry and uneven mass distribution.

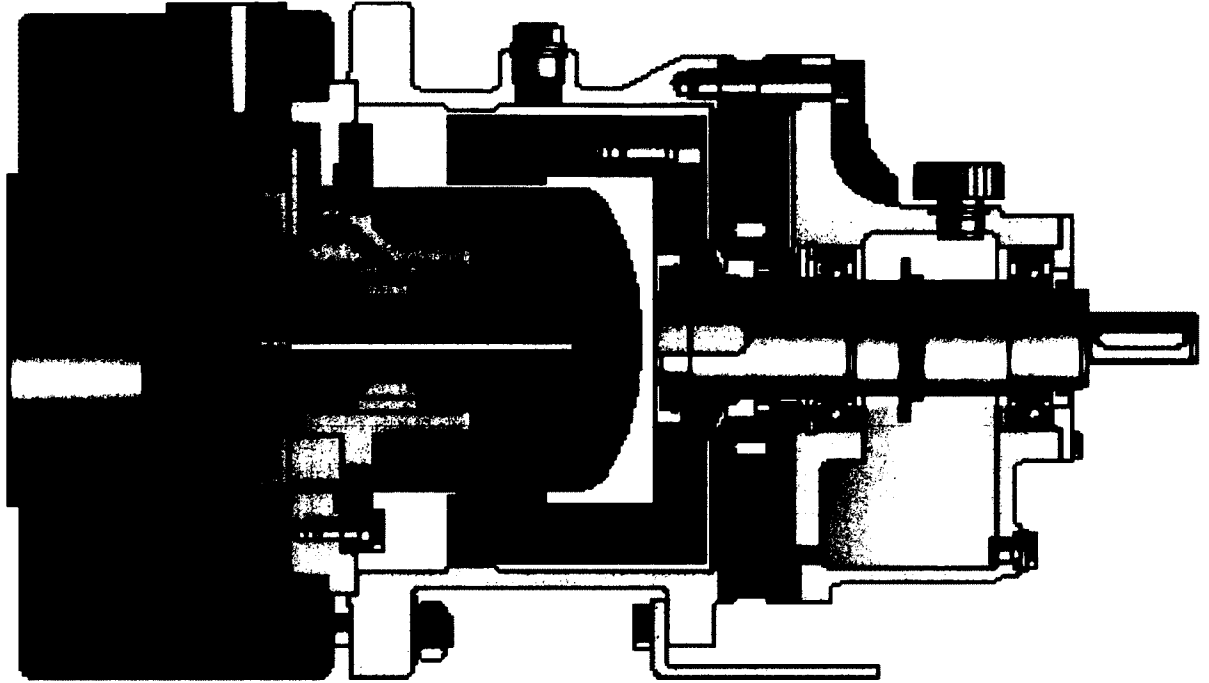


Figure 3-10: Cut away of SLM-NVE pump from Klaus Union [24]

The fluid is accelerated through the impeller along with the static pressure being increased, while the volute subsequently turns and diffuses the flow. This process generates a very complicated flow field that is three dimensional. Modeling the impeller and volute fluid dynamics is beyond the scope of this work, and the pipe flow correlations for convective heat transfer are unlikely to be accurate. However, compared to the thermal inertial of the pump casing, the large red section in Figure 3-10, and the rest of the loop, any inaccuracy regarding the impeller will have a negligible effect on the results of the simulation. Therefore the impeller and volute's mass will be estimated and be subsequently modeled as an annular component with an outer diameter that is an average between the inlet duct's diameter and the discharge nozzle's diameter. The impeller and volute's hydraulic diameter will be derived from the estimated average cross sectional flow area and perimeter.

3.5.3 Meshing

With the various parts of the loop modeled, each part requires an appropriate mesh to capture the geometry and accurately model the heat transfer. Each component and piping run is meshed independently; the user being required to input the desired number of x-direction nodes in each component and the order of accuracy of the length scale at which to capture the x-direction location of features on the piping runs. To satisfy the solver, a minimum of three x-direction nodes are required for each component. Since the fluid is being modeled as one dimensional, once the user has defined the x-direction spacing at the input stage, no further discretization is required.

The components, with a uniform wall thickness and defined x-direction spacing, require a radial node distribution in the wall to complete their discretization. While heat transfer in the wall nodes is limited to conduction, it is still possible to characterize a cell's response using the Biot number (Eqn. 3.18).

$$Bi = \frac{h_{conv}V_{body}}{k_b A_s} \quad (3.18)$$

where: h_{conv} : convective heat transfer coefficient; V_{body} : volume; k_b : thermal conductivity; A_s : surface area.

Using the Biot number allows the cells to be sized such that any error introduced by the discretization to be mitigated. As the Biot number gives the ratio of internal to external thermal resistance of a body, it determines if the temperature will vary in space for the body. The discretization of the material results in the assumption that the temperature can only vary linearly between cell nodes and follows a lumped capacitance model in time. For this model to be accurate, the material must be thermally thin so that heat may be taken as constant throughout its volume. Materials are described as being thermally thin when the Biot number is less than 0.1 [19]; satisfying this condition for every cell enforces global accuracy of the model.

By equating the conductive heat flux to an equivalent convective heat transfer coefficient for the same temperature difference (Eqn.3.19) one can find an effective Biot number (Eqn. 3.20) for a given cell size, which reduces to a simple directionally scaled volume to area ratio for a spatially invariant thermal conductivity.

$$h_{eff} = \left(\frac{k}{\Delta x_i} \right)_{avg} \quad (3.19)$$

$$Bi = \frac{V_{body}}{(\Delta x_i)_{avg} A_{surf}} \quad (3.20)$$

Using the rotational symmetry of the modeled parts, the Equation reduces to two dimensions, and simplifies to a two variable Equation. Since Δx is fixed by the user, using the condition that $Bi < 0.1$ the maximum Δr for each component may be solved (Eqn. 3.21).

$$Bi = \frac{2\pi[(r+\Delta r)^2 - r^2]\Delta x}{(\Delta x + \Delta r)(2\pi[(r+\Delta r)^2 - r^2] + 2\pi\Delta x(2r + \Delta r))} \quad (3.21)$$

This reduces to Equation 3.22, which can be solved for any given radial position in the pipe wall and Δx . Since $r, \Delta x \in [0, \infty)$ and $Bi \leq 0.1$, there exists a real positive solution for Δr that satisfies the necessary condition on the Biot number for any combination.

$$(1 - 2Bi)^2 r^2 - 6Bi(1 - 2Bi)r + Bi^2 \geq 0 \quad (3.22)$$

Solving the Biot number across the wall fixes the upper bound for Δr and the result is compared to the wall thickness. If this would result in a radial node distribution of less than three nodes, the radial node count is increased to three. A minimum of three radial nodes is imposed to capture any non linear effects while providing independence from discretization for the two boundary conditions. The potential increase in node count per part was found to have a negligible impact on solution time.

In the piping runs, where features are present, to simplify the solver, uniform x-direction spacing is imposed to capture each feature to the order of accuracy defined by the user input. The x-

direction spacing is determined by finding the largest common multiple of each feature and interspliced pipe segment's length. If this results in an x-direction node count less than the user defined number of nodes for the adjoining component, the originally calculated node count is doubled until it meets or exceeds the user defined node count. The same analysis using the Biot number is applied to determine the radial node spacing in the walls.

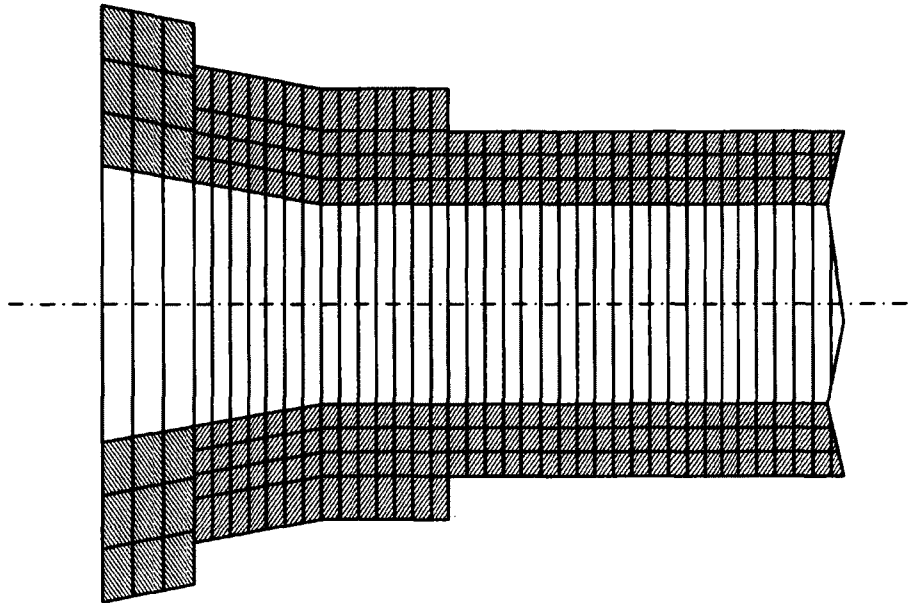


Figure 3-11: Typical Mesh for a Component and Piping Run

Continuing the example initially presented in Figure 3-4, a typical mesh for the component and piping run that comprises the hub welded to the pipe is shown in Figure 3-11. In this case, the added thickness due to the feature satisfies the thermally thin condition and so is represented by a single node since the three node minimum is already satisfied by the constant thickness pipe wall. The minimum calculated x-direction nodes in the piping run exceed the user defined three nodes in the adjoining component, so they are not increased.

After the meshing scheme is applied to each component and piping run, the individual fluid meshes are joined to create a continuous fluid domain. Each solid domain mesh remains

separate as the node connections at the boundaries between components and piping runs are unlikely to map one-to-one. To handle the solid domain interfaces, a coefficient matrix is used to map the temperature gradient from the source side to a set of ghost cells on the target side that map one-to-one to generate the appropriate boundary condition. This allows for handling any interface geometry while preserving the adiabatic boundary condition for any external exposed surface.

3.6 Algorithm

A flow chart, spanning the six following pages, is used to demonstrate the algorithms used to solve the set of Equations described above and their implementation in the code. The code is laid out by Matlab functions (self contained, executable code) and looping structures. Necessary supporting data is added to this general structure where necessary. The blocks used in the flow chart are of standard design, and defined below in Figure 3-12: Flow Chart Key for convenience.

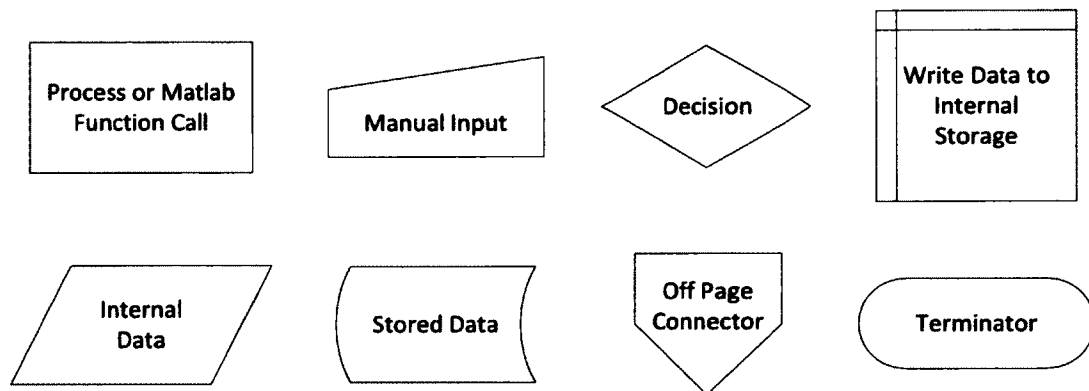
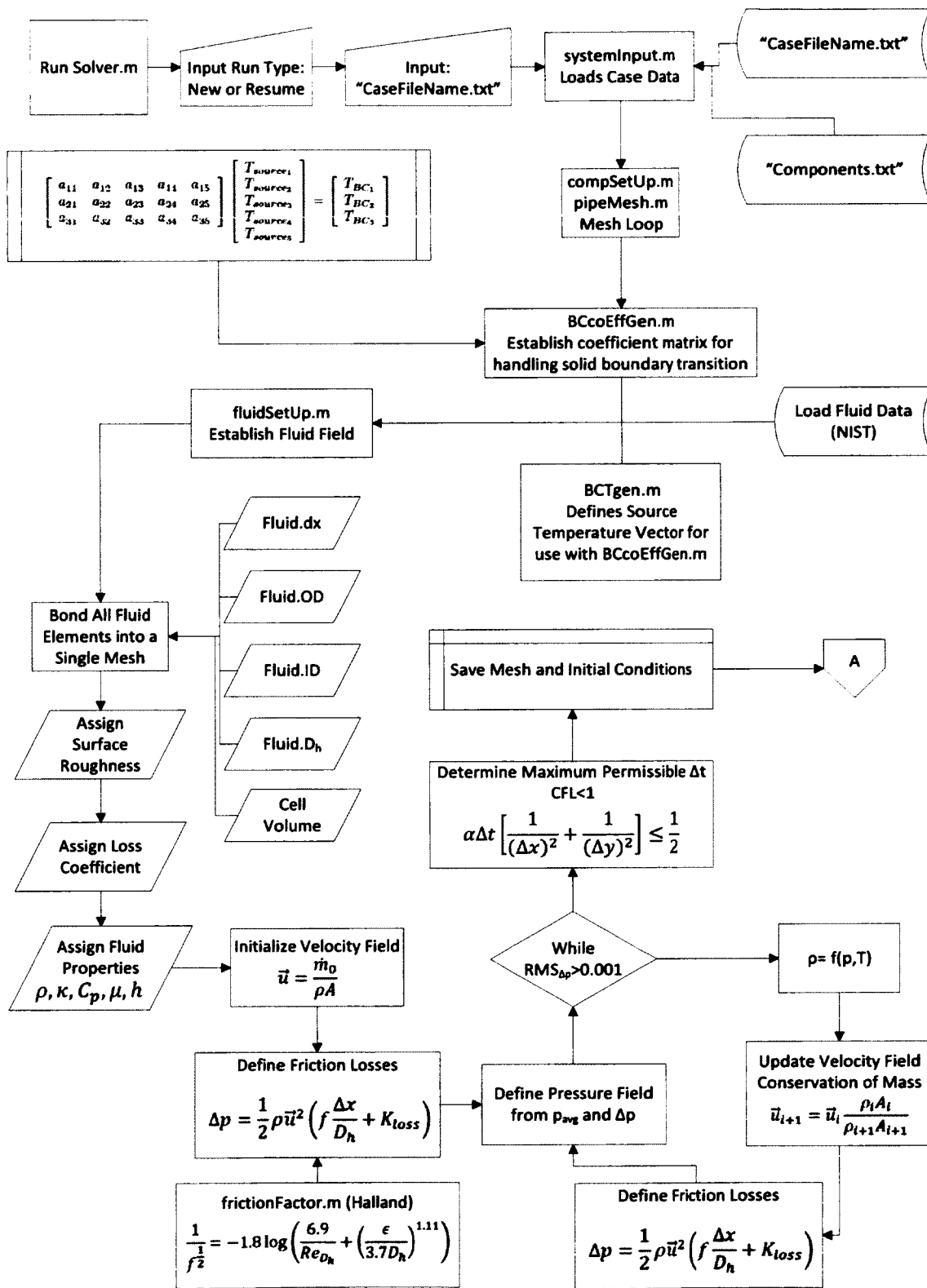
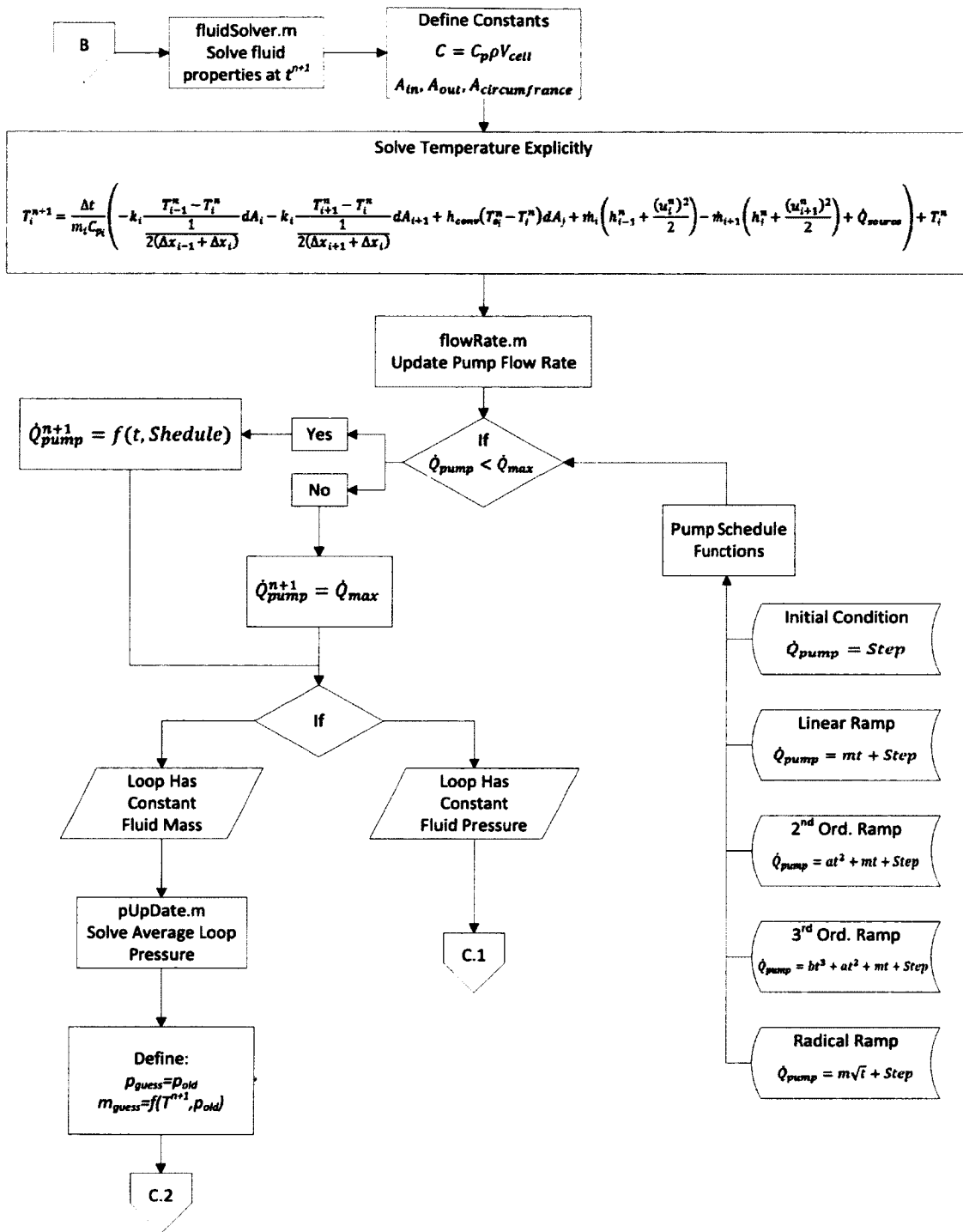
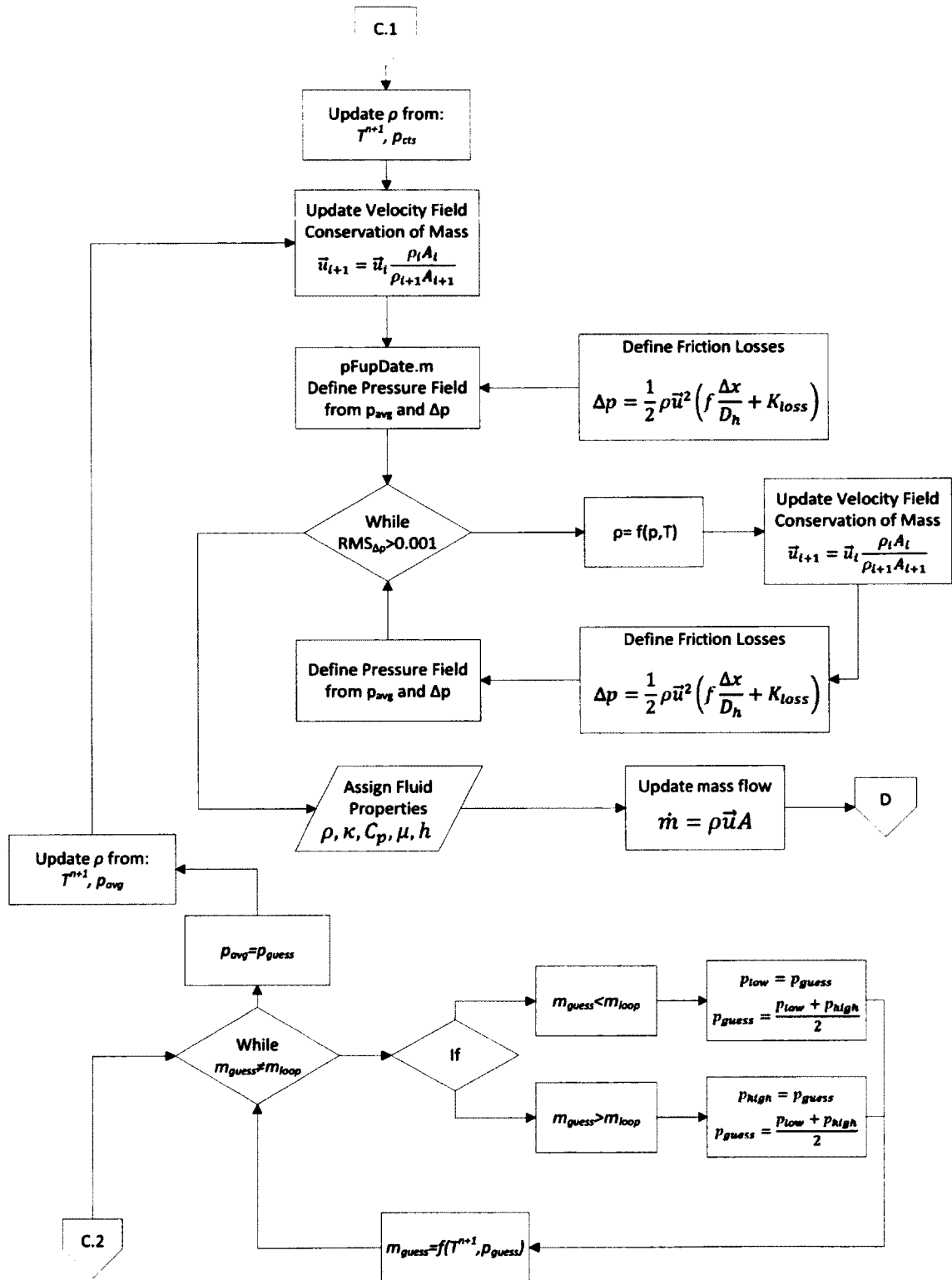
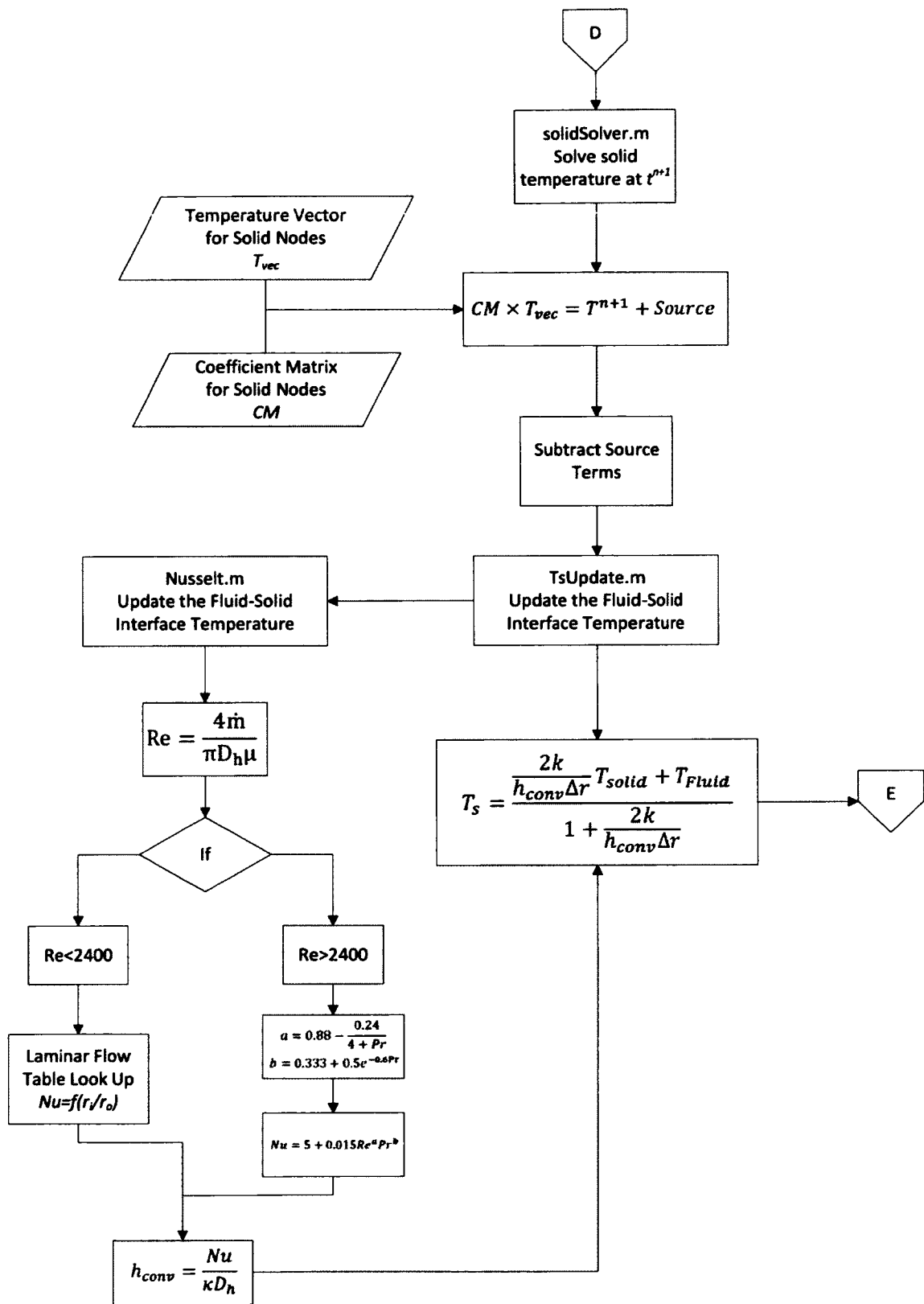


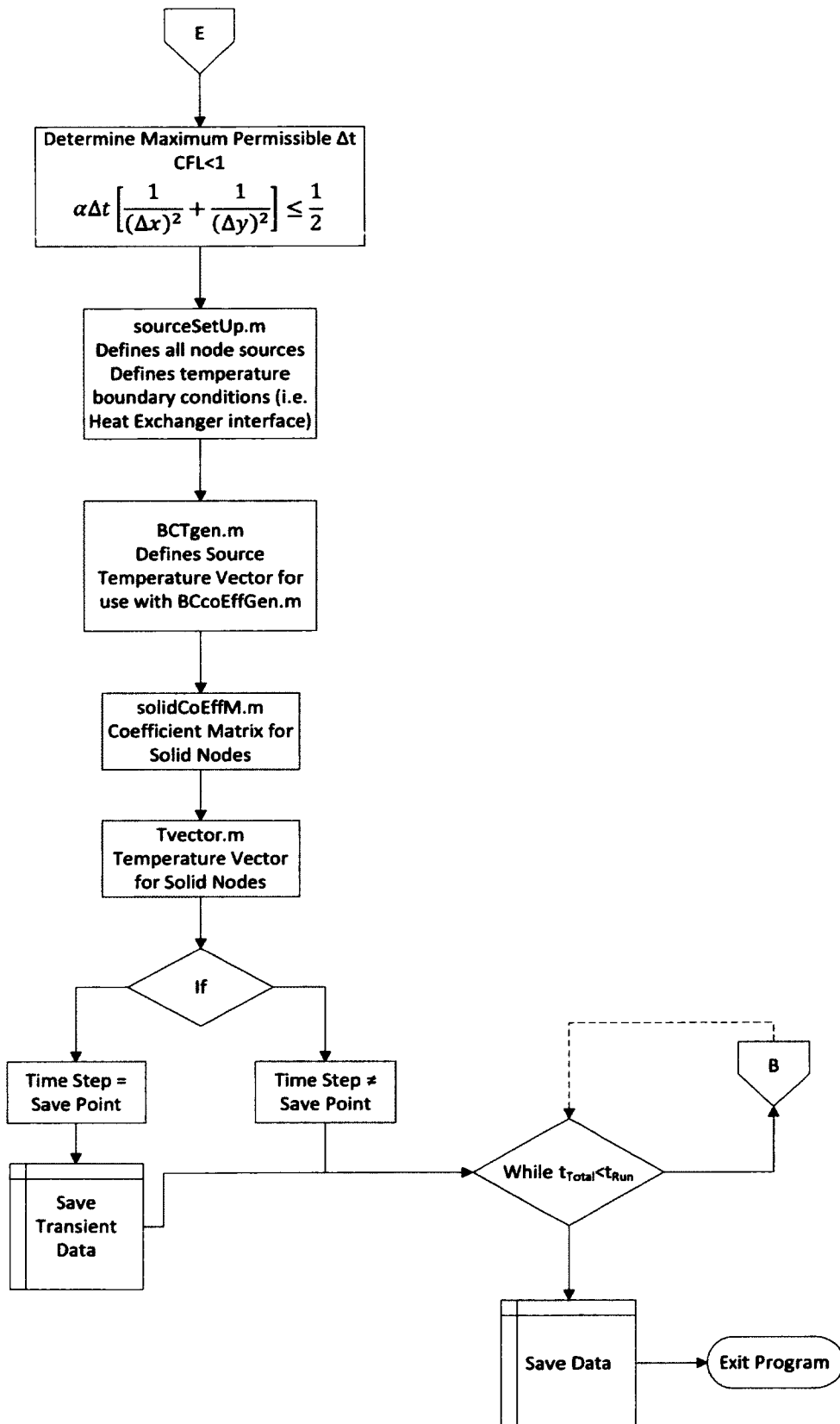
Figure 3-12: Flow Chart Key











3.7 Conclusion

The model developed provides the necessary tools to model the defining features of a pipe network with distinct components containing a generic compressible, subsonic fluid. Mesh generation is handled automatically based on geometric inputs and accuracy requirements. A transient explicit solver is utilized to capture the transient thermal-hydraulic behaviour of the fluid-solid system, with the time step dynamically optimized to maintain stability while minimizing solution time.

Each component, such as a pump or heat exchanger, is modeled separately to account for its individual heat transfer characteristics and thermal inertia. The piping segments between each component are defined independently as well to allow for the variation of piping in the network. The piping network may exchange heat with its environment through components specified as heat exchanges, while all other components are assumed to be well insulated and adiabatic. This was chosen to optimize the code for use in regards to designing the super-critical thermal hydraulic loops at Carleton, as discussed above. For future, generic use, this can be modified by using the thermally communicative boundary conditions of the heat exchanger component across all elements of the pipe network.

Once the geometry of the pipe network is defined by the user, the code automatically generates a mesh of the solid and fluid domains that respects the requirements of the lumped thermal capacitance model using the Biot number. The time step is then determined based on the imposed stability criteria of the mesh for an explicit solver and the CFL number. The time step is updated dynamically to ensure the CFL number restriction is met as the velocity field of the fluid changes.

The algorithm uses real fluid properties from a look up table, and is capable of handling any single phase real fluid that remains subsonic. Thermal compressibility and frictional effects are solved along with heat transfer for the fluid. The solid domain is limited to solving the variation in the temperature field, though the solid material may be specified and its temperature dependent thermal conductivity will be used. All cases are run as transient simulations with solution criterion being defined as either time elapsed, or a steady state situation being achieved as defined by the change in temperature in time, either at individual nodes or a global average, being less than a user defined threshold.

The time history of the fluid's defining properties and the solid's temperature are stored as the results of the simulation.

Chapter 4 Numerical Simulation Results

With the numerical solver developed the optimal time step and grid independence are established. The code is then checked across a variety of cases to ensure the numerical response is the same as the analytical. Once the behaviour of the numerical model is established, the results of a start up simulation are presented.

4.1 Time Step Size

The code automatically selects the largest permissible time step based on the von Neumann stability criterion and the Courant number (Eqn. 4.1) [39]. As described in Section 3.5.2, the time step must be limited based on the mesh stiffness to ensure stability. While this ensures that the numerics remain convergent, it does not describe the fluid's behaviour in any way. No provision was made to handle fluid passing through multiple cells in a single time step, as the time step was expected to be sufficiently small that this would not happen.

$$C = \frac{u\Delta t}{\Delta x_i} \quad (4.1)$$

where: C : Courant number; u : velocity; Δt : time step; Δx_i : node spacing

To prevent errors or instabilities from developing due to fluid passing through a cell unaccounted, due to the time step being too large, a maximum Courant number of unity is imposed globally. As the velocity field varies in time and space, the code is able to dynamically update the time step as necessary before solving the system of Equations. In practice, with the grids used, the von Neumann stability criterion is the limiting factor on the time step, so the Courant number remains below unity.

4.2 Grid Independence

During benchmarking, where temperature gradients remained small, the results were found to be insensitive to the grid-node spacing. The code imposes a minimum node count for each loop component, of 3 in each direction, which is sufficient to capture linear and near-linear trending. The solid nodes are spaced based on the Biot number, ensuring a universal compliance with the lumped-capacitance model used for material response to heat transfer. Thus the only limitation on grid size lies with the fluid, and the assumption that the average bulk temperature sufficiently represents the fluid field inside the cell. At a sufficiently high Reynolds number the bulk temperature and centerline temperature collapse to the same value for a radial temperature profile, as demonstrated in Figure 2-5. Typical flow conditions, under which the simulations were run, have a Reynolds number in excess of what is necessary to generate this flat radial temperature profile. Therefore only axial gradients will impose a limitation on the fluid cell size, specifically on the axial spacing since the diameter is fixed from the geometry. Examining the fluid cell's thermal time constant (Eqn. 4.2), a maximum fluid volume may be imposed such that the cell's response is on the same order of magnitude as the time step, and the lumped-capacitance model be used with minimum error [19].

$$\tau = \frac{\rho V c_p}{h_{conv} A_s} \quad (4.2)$$

$$Fo = \frac{\alpha t A_s}{V} \quad (4.3)$$

where: ρ : density; V : volume; c_p : specific heat capacity at constant pressure; h_{conv} : convective heat transfer coefficient; A_s : surface area; α : thermal diffusivity; t : time; Fo : Fourier number; τ : thermal time constant.

The thermal time constant is traditionally defined by the Biot number and the Fourier number (Eqn. 4.3). Since the Biot number is not calculated for the fluid cell, it is simpler to examine the thermal time constant directly. Rearranging Equation 4.2 and applying the definition of hydraulic

diameter $D_h = \frac{4A_c}{P}$ to the volume-to-surface area ratio yields the time constant in terms of the hydraulic diameter (Eqn. 4.6) which is a known input parameter defined independently of the axial spacing.

$$V = A_c \Delta x \quad (4.4)$$

$$A_s = P \Delta x \quad (4.5)$$

$$\tau = \frac{\rho D_h C_p}{4h_{conv}} \quad (4.6)$$

where: ρ : density; V : volume; c_p : specific heat capacity at constant pressure; h_{conv} - convective heat transfer coefficient; A_s : surface area; A_c : cross sectional area; P : perimeter; D_h : hydraulic diameter; τ : thermal time constant; Δx : spacing along principle axis.

While the density, specific heat capacity and convective heat transfer coefficient all vary during the simulation, a worse case thermal time constant may be derived for the temperature and pressure range covered by the simulation. For the 7-rod-bundle test section, under typical experimental conditions, the maximum thermal time constant exists as the fluid passes through the pseudo-critical point, where it reaches a maximum of 0.0135.

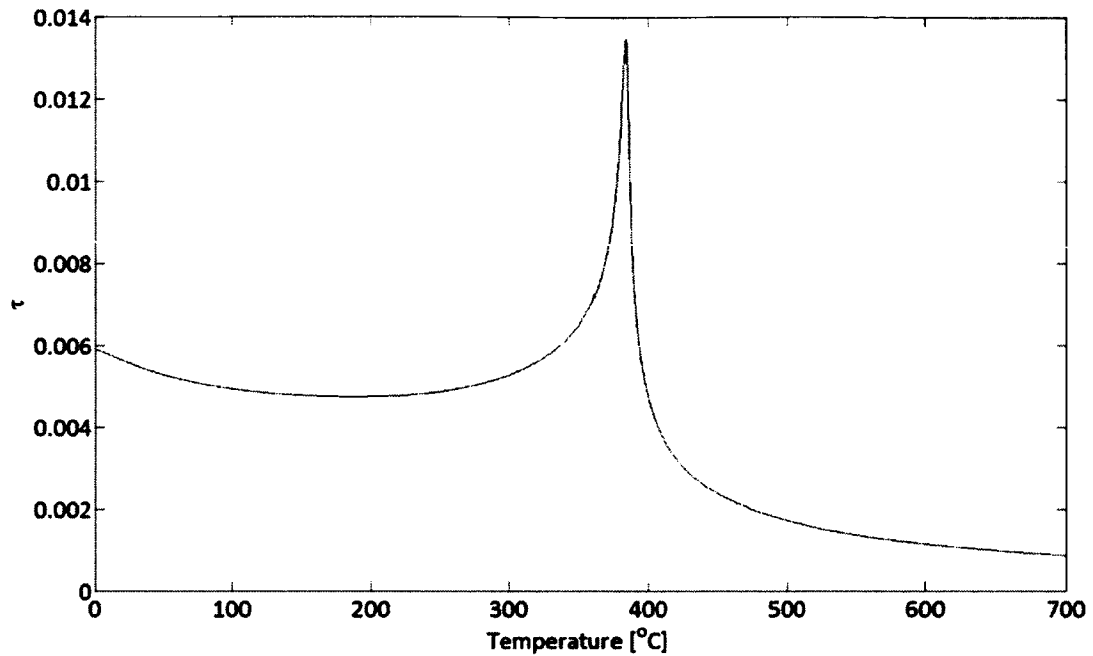


Figure 4-1: Thermal Time Constant versus Temperature for 7-Rod-Bundle Test section at 25 MPa and Mass Flow Rate of 0.127 kg/s

The thermal time constant varies from $O(-3)$ to $O(-2)$, while a typical time step size is $O(-3)$.

Using these values to determine the right-hand-side (RHS) in Equation 4.7, transient heat transfer with convection, the maximum supported temperature gradient may be determined for

fluid. In regions of weak heating or cooling, such that $\frac{\partial T}{\partial t}$ approaches zero, the left-hand-side

(LHS) collapses to unity, so that the time required goes to zero. In regions of strong heating,

such as the test section, the source term defining the heat input dominates so that the other heat transfer terms may be ignored for the purpose of defining the required axial spacing.

Rearranging Equation 4.7 to isolate the temperature difference, and replacing the temperature

derivative with the definition of the source term per Equation 4.8 and 4.9 yields a definition for

the maximum permissible axial spacing defined exclusively in terms of user defined input variables, Equation 4.10.

$$\frac{\frac{\partial T}{\partial t} \Delta t}{T_i - T_\infty} + 1 = \exp\left(-\frac{t}{\tau}\right) \quad (4.7)$$

$$\dot{Q} = \dot{m} c_p \Delta T \quad (4.8)$$

$$\frac{\partial T}{\partial t} = \frac{\dot{Q}}{\dot{m} c_p \Delta t} \quad (4.9)$$

$$|T_i - T_\infty| = \left| \frac{\dot{Q}}{\dot{m} c_p} \left(1 - \exp\left(-\frac{\Delta t}{\tau}\right)\right)^{-1} \right| \quad (4.10)$$

where: T : temperature; t : time; τ : thermal time constant; \dot{Q} : heat rate; \dot{m} : mass flow; c_p : specific heat capacity at constant pressure.

At the pseudo-critical point, where τ is maximized, using the same fluid properties and time step as above, produces the limiting case of $|T_i - T_\infty| = 4.75 \times 10^{-4} \dot{Q}_i$. For a total heat source of 300 kW (the maximum available), the permissible temperature rise for various node schemes are presented in Table 4-1 below. A minimum necessary temperature gradient is given by the total temperature rise though the test section applied with a linear profile. This somewhat under predicts the maximum temperature gradient as demonstrated below, but is sufficient as a first order estimate.

Table 4-1: Maximum Permissible Temperature Gradient for Different Axial Spacing

Number of Cells	Cell Heat Source [kW]	ΔT_{max} [°C]	ΔT_{min} [°C]	% of ΔT_{min}
1	300	142.5	340	57.3
3	100	47.5	113	58.0
10	30.0	14.25	34	58.1
50	6.00	2.85	6.8	58.1
100	3.00	1.425	3.4	58.1
200	1.50	0.7125	1.7	58.1
500	0.60	0.285	0.68	58.1

Increasing the number of cells used to discretize the test section has a limited effect on improving the model's ability to meet the requirements for the lumped-capacitance model. The response to increasing the cell count is asymptotic, reaching the limit at ten cells. The only option to reduce the error using the lumped-capacitance model at the stated conditions would

be to increase the time step, which is limited by the von Nueman stability criterion. While the time step cannot be increased, the worse case scenario presented above, does not occur in the simulation, as the temperature profile through the test section at steady state is not linear. Instead, where the thermal time constant is the worst near the pseudo-critical point, the temperature profile flattens, thus the minimum temperature difference required approaches zero. Away from the pseudo-critical point the fluid's specific heat capacity drops by an order of magnitude. In turn maximum allowable temperature gradient increases by an order of magnitude which is more than sufficient to account for any of the temperature gradients found in the thermal-hydraulics loop. While ten nodes would be sufficient to satisfy the requirements of the lumped-capacitive model and make the solution grid independent, in practice one hundred nodes were used for the major components to provide a finer resolution of the temperature gradients. No variation in the simulation results was found by either doubling or halving the node count to two hundred or fifty, respectively.

4.3 Benchmarks and Quality Assurance

Three benchmarks were carried out to evaluate the numerical solver's capability to handle the heat transfer phenomena prescribed by the system of Equations it is to solve. Conduction effects in the solid and fluid domains are examined independently, and convection in the fluid is tested. The code's ability to handle the large variations in fluid properties near the critical and pseudo-critical point are also discussed. The benchmarks carried out all involve first order systems (Eqn. 4.11) with a unit step applied; the correct response to the unit input is given by Ogata, and demonstrated in Figure 4-2 below [42].

$$\frac{C(s)}{R(s)} = \frac{1}{\tau s + 1} \quad (4.11)$$

where: C : energy storage term; R : energy dissipative term; τ : time constant; s : time.

The transient response of each benchmark will be compared to the analytical response, demonstrated in the figure, to determine the numerical solver's capability to accurately handle the different Equations that comprise heat transfer effects in the loop.

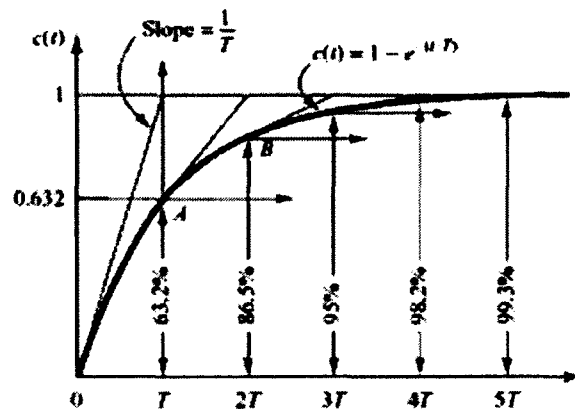
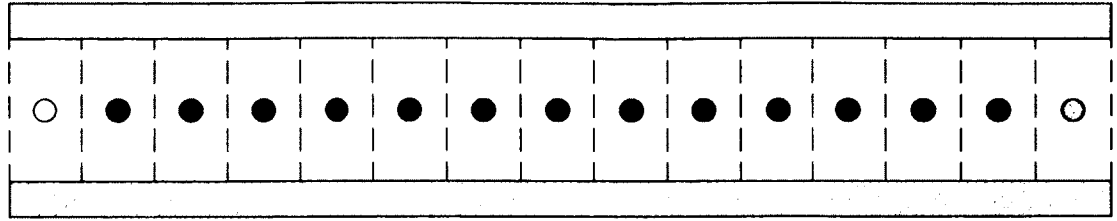


Figure 4-2: "Exponential response curve [1st Order]" [42]

4.3.1 Conduction in the Fluid Domain

In a general flow situation conduction effects will have a negligible impact on heat transfer in the fluid with the obvious exception of right by solid boundaries where convection mode heat transfer disappears. To test the accuracy of conduction in the fluid domain, due to its minimal effect, the system was modified and the conductivity of the fluid increased by an order of magnitude. The fluid domain was isolated between two cells with fixed temperature while the fluid-solid interface was made adiabatic. With the flow velocity set to zero, the fluid domain was made to mimic the classic one dimensional heat transfer problem of a bar with fixed end temperatures. The effective set up is described in Figure 4-3 below, with the defining properties given in Table 4-2. The fluid was held at very high pressure to ensure that it remained in the fluid domain across all temperatures, so that the properties would not vary significantly with temperature.



○ $T_{\text{Hot}} = 100\text{ }^{\circ}\text{C}$

○ $T_{\text{Cold}} = 25\text{ }^{\circ}\text{C}$

Figure 4-3: Axial Conduction in the Fluid Domain

Table 4-2: Axial Conduction Fluid Domain Properties

Pressure [MPa]	Conductivity [W/mK]	OD [mm]	Δx [mm]	# of Nodes	T_{Hot} [$^{\circ}\text{C}$]	T_{Cold} [$^{\circ}\text{C}$]
25	6.9 to 6.2	25.4	2.0	50	100	25

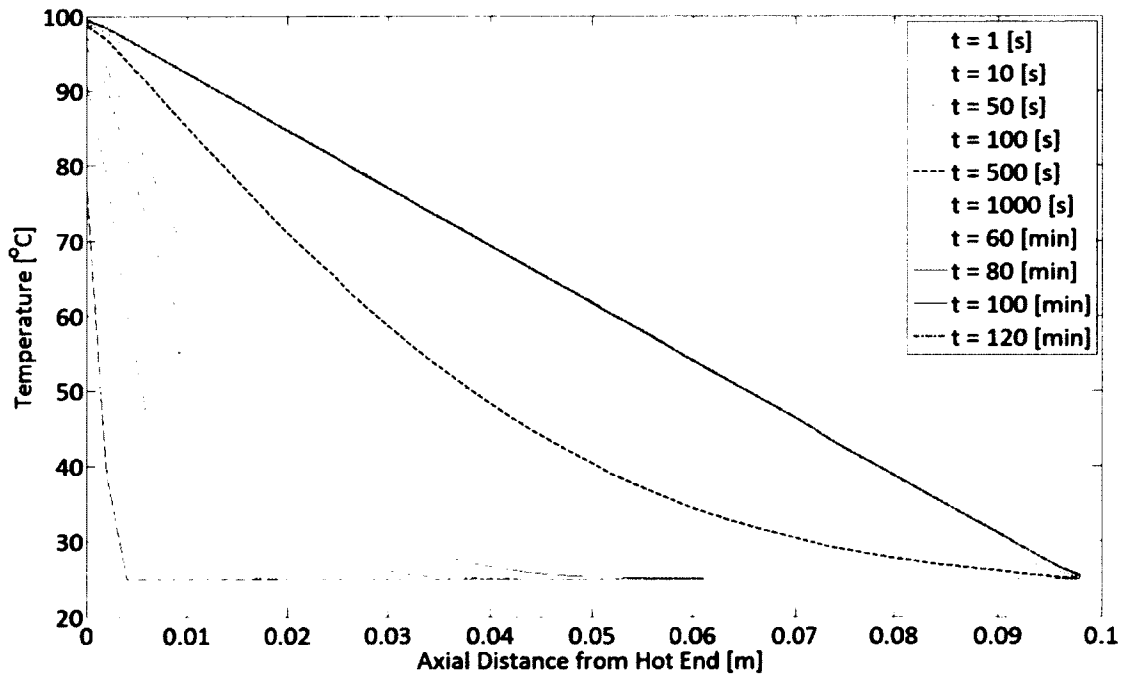


Figure 4-4: Fluid Temperature Profile at Selected Times

The fluid, black nodes in Figure 4-3, was initialized at $25\text{ }^{\circ}\text{C}$ and the simulation was run to a total time of 120 simulated minutes. The time step determined by the stability criterion was 0.5004 s.

The temperature profile of the fluid is plotted above (Figure 4-4) for ten time slices to show the

fluid's thermal response to pure axial conduction. The conduction problem solved is a first order Equation exposed to a unit step, so the fluid is expected to respond as the analytical solution in Figure 4-2. As the heat flows from the hot end, the temperature profile develops as expected, with the sharp knee originally present between the hot fluid and the still unheated fluid flattening out as the temperature gradient lessens. After 500 seconds has elapsed, the second boundary condition imposes itself on the system, and the profile continues to flatten until steady state is reached, and the temperature profile is fully linear matching the Fourier's conduction Equation. Figure 4-5 tracks the first fluid cell's response to the step function which matches a first order system response perfectly.

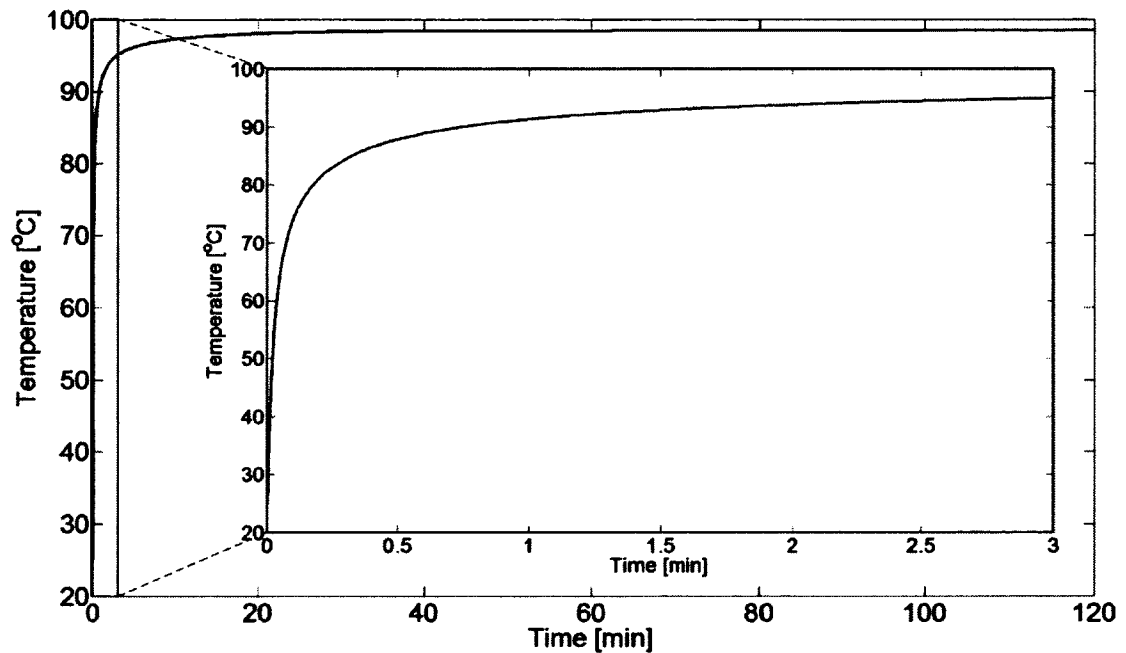


Figure 4-5: First Fluid Cell's Temperature Response to a Step Input, Axial Conduction

4.3.2 Convection in the Fluid Domain

Convective heat transfer from the fluid to the solid is tested by modeling a uniform torus, which meets the numerical solver's closed loop model while providing an effective infinite fluid path.

This produces an identical response in each fluid cell. The fluid-solid interface temperature is held constant, and the fluid's response to the resulting convective heat transfer is observed. Since each cell is identical in time, there can be no axial conduction as no axial temperature gradient exists in the torus. The conditions used for the simulation are given in Table 4-3 below. The initial temperature difference was intentionally kept small as the simulation was run at constant pressure, the same as the simulations run on the thermal-hydraulic loop, and a significant temperature difference would result in compressibility effects, altering the velocity field in time and therefore the convective heat transfer coefficient. The convective heat transfer coefficient is required to remain constant for the system to be first order. The fluid's temperature response to applying the step function at the surface is plotted in Figure 4-6 below; the computed response matches the analytical response for the first order system.

Table 4-3: Convective Heat Transfer Fluid Domain Properties

Pressure [MPa]	Velocity [m/s]	Reynolds Number	Prandlt Number	h_{conv} [W/m ² K]	T _s [°C]	T _o [°C]
25	0.2467	8000	5.23	1560	30	25

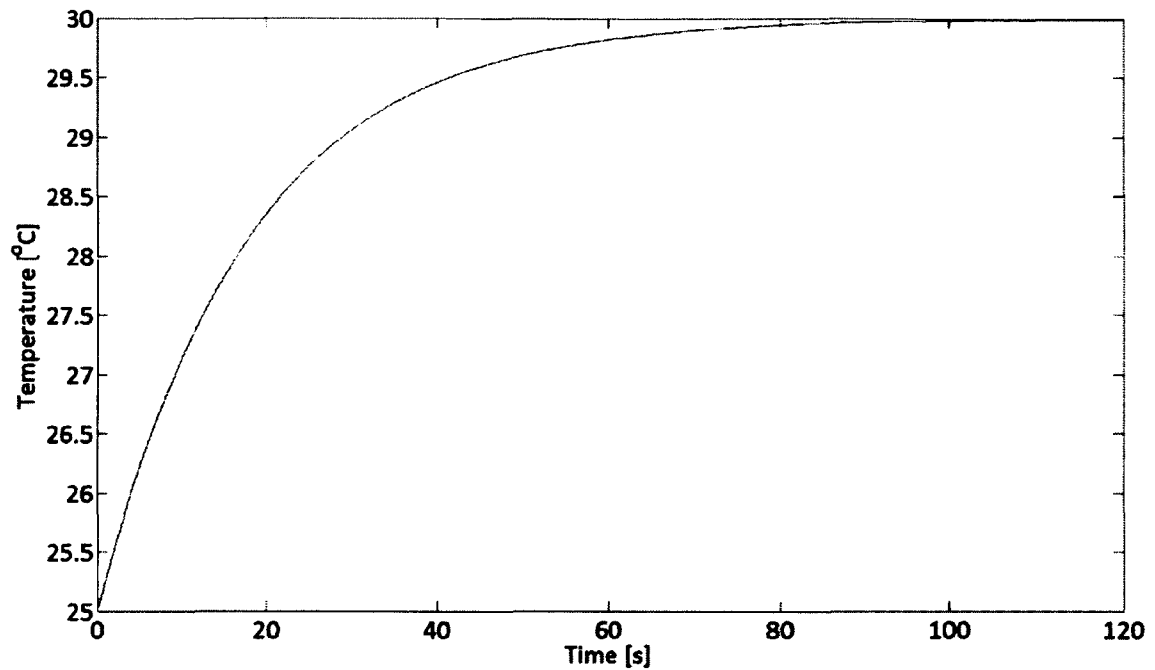


Figure 4-6: Fluid's Temperature Response to a Step Input, Convective Heat Transfer

4.3.3 Conduction in the Solid Domain

Conduction in the solid domain uses the same conduction model as the fluid; however, the conduction is two dimensional. The discretized version of the conduction Equation in the axial direction is identical to the version used for the fluid cells. Since conduction in the fluid was found to be correct, the test need not be repeated in the solid domain. Qualifying the radial conduction of the numerical solver will complete the verification of the two dimensional conduction in the solid domain. The torus model was employed again to provide an infinite solution space, and eliminate any axial conduction effects. A constant temperature was applied to the fluid-solid interface, and the default adiabatic condition was used along the outer surface. The resultant one dimensional system is illustrated in Figure 4-7 below.

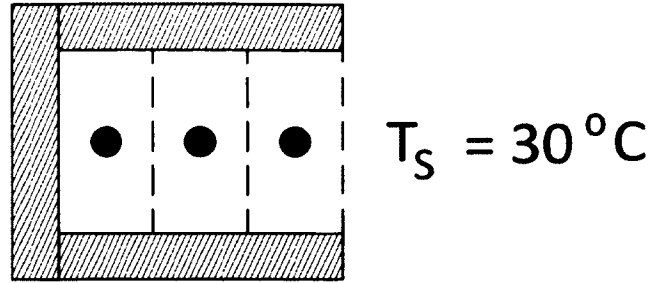


Figure 4-7: One Dimensional Radial Conduction in the Solid Domain

Table 4-4: Radial Conduction Solid Domain Properties

Conductivity [W/mK]	Δx [mm]	Δr [mm]	# of Nodes	T_o [°C]	T_s [°C]
9.9344 to 9.8995	20	10	3	25	30

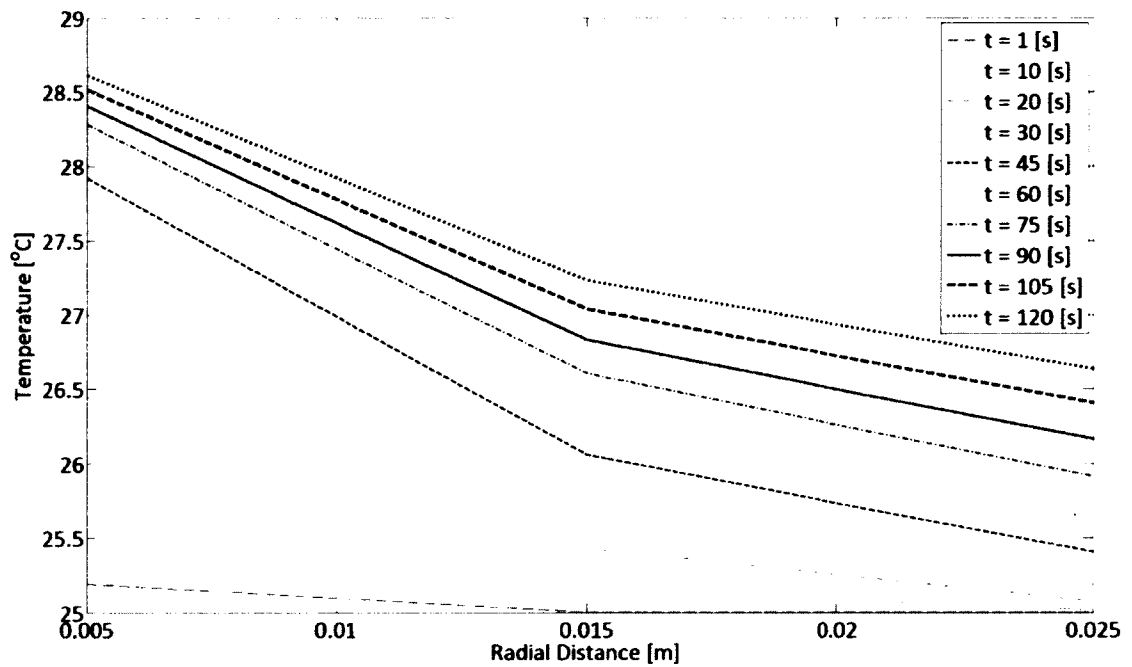


Figure 4-8: Solid Temperature Profile at Selected Times

The pipe wall comprising the solid domain is relatively thin, requiring only three nodes to meet the Biot number requirement. The linear behaviour of Fourier's heat transfer Equation is very apparent due to the coarseness of the temperature profile compared to the axial conduction case with its higher node count. The transient response between the constant temperature wall

and adiabatic wall behaves as expected, with strong thermal gradient developing between the first and second node based on their thermal inertia. As time progresses and the first node approaches the surface temperature, the first node sees less heat input, while the other nodes' temperature begins to catch up to the first node's temperature due to the adiabatic boundaries, and the temperature profile continues to flatten. Run to steady state all the nodes would reach the surface temperature producing a uniform temperature field.

The first cell's temperature response to applying the step function at the surface is plotted in Figure 4-9 below; the computed response matches the analytical response for the first order system.

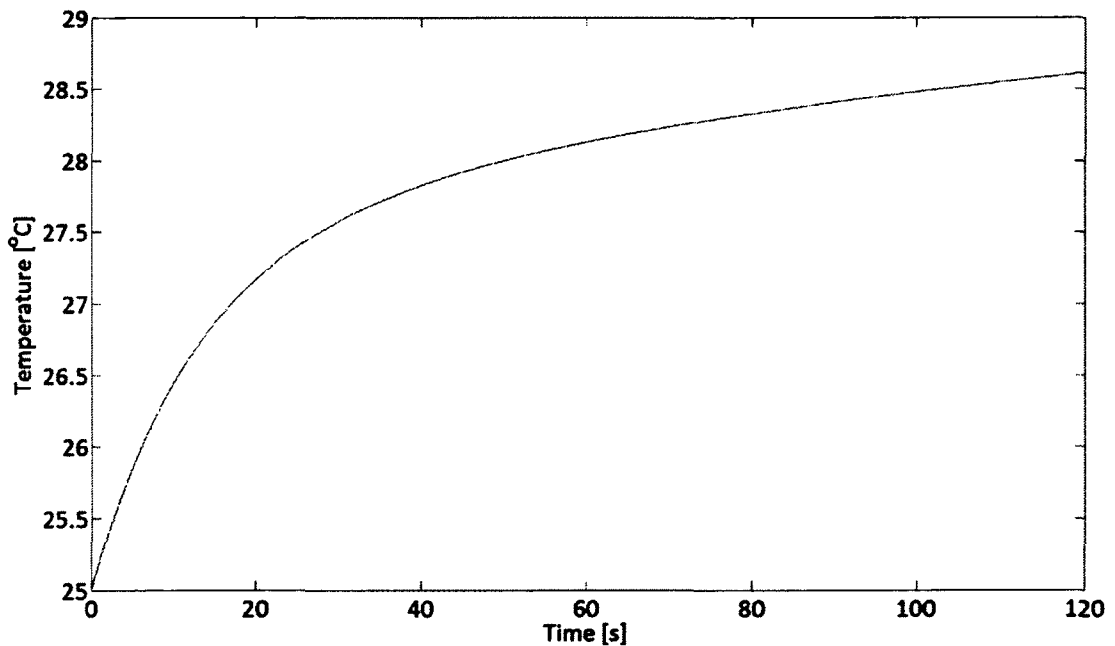


Figure 4-9: First Solid Cell's Temperature Response to a Step Input, Radial Conduction

4.3.4 Fluid Property Handling

Accurately modeling the fluid's behaviour, and capturing the thermal effects due to property change in the near critical region is challenging for numerical simulations due to the extreme property gradients. The numeric solver uses a look up table based on NIST data to ensure accuracy of the fluid properties; however, the use of a look up table requires the data resolution to be finite. Away from the pseudo-critical point, where the fluid's properties vary nearly linearly, the data is relatively coarse, using 10 °C and 1 bar step sizes between data points. Near the pseudo-critical point, the data is refined to use 0.2 °C and 1 bar step sizes based on the work of John [43]. This provides sufficient data resolution to the look up table to ensure accurate handling of the fluid properties throughout the entire range of temperature and pressures experience by the simulation. The method of interpolation between data points, using one of the Matlab built-in functions requires consideration. The function *interp2* allows for four different two dimensional interpolation methods to be utilized: nearest neighbour, linear (default), cubic spline, cubic. All the methods require the data to be monotonic. This creates a problem when the data points being interpolated over lie on either side of a pseudo-critical isotherm or isobar, where the data is no long monotonic since the property gradient changes sign between data points.

Investigating this issue, it was found that using linear interpolation was the most sensitive, and would randomly fail first, causing the simulation to crash due to unuseable results being returned (Not A Number). Using the cubic spline interpolation method is much more robust, but introduces an over-shoot, under-shoot problem with the interpolation. In regions of strong property gradients but small absolute values, such as found with the fluid's viscosity in the near critical region, the cubic spline method would return negative viscosity values, which is

physically impossible. The error with the over-shoot was equal in magnitude to the under-shoot error. For this reason the cubic spline method cannot be used to interpolate the data.

The look up table data is sufficiently fine in the near critical region that linear interpolation can be used accurately between data points, as described above, so the linear interpolation method was used despite its tendency to occasionally crash the simulation. Despite numerous hours of investigation, exact, repeatable conditions that would cause the linear method of *interp2* to crash could not be identified. Since the conditions to cause the simulation to crash could not be identified to be coded around, the numerical code was made robust enough to allow for the instability caused by linear interpolation. The numerical solver is capable of resuming a simulation from a previous time step, allowing the simulation to be restarted after crashing or continuing from the end of a previous simulation. The user is able to define the frequency that transient data is stored providing control over the impact on simulation time due to any instability present in the simulation.

4.4 Simulation Results

A model of the supercritical water thermal-hydraulics loop incorporating the 7-rod-bundle test section was developed for the simulation presented in this section. The models of the major components were used as presented in Section 3.6, with their specifications listed in Table 4-5. The frictional loss coefficient is based on the manufacture's data where available or estimated from standards provided by White [22]. The piping is 1.5" schedule XXS around the loop with ¾" schedule 160 bracketing the flow meter, as described in Chapter 1. The additional mass distribution due to the fittings was modeled by defining appropriately sized features along the piping segments. Elbows, T-joints and other fittings were also modeled as features, to account for their loss co-efficient, even though they do not change the mass distribution from the pipe.

The piping runs are detailed in Table 4-6. A surface roughness of 3.0 μm was chosen for all components and piping, representing new stainless steel commercial ducting [22].

Table 4-5: Simulation Model Component Definition

Component	Mass [kg]	V_{fluid} [m^3]	D_h [mm]	OD [mm]	Loss Coefficient	Axial Nodes
Pump	2	2.18×10^{-5}	18.63	27.94	0	10
Globe Valve	27	1.74×10^{-4}	27.94	27.94	0.2	10
Reducer	0.0204	1.30×10^{-6}	21.77	21.77	0.1	3
Flow Meter	0.6	2.06×10^{-5}	15.6	15.9	1.0	10
Reducer	0.0204	1.30×10^{-6}	21.77	21.77	0.1	3
Test section	35.12	1.10×10^{-3}	4.56	38.18	-	100
Heat Exchanger	1.626	1.11×10^{-3}	3.35	176	1.35×10^4	100
Filter	5	3.68×10^{-4}	18.63	27.94	0.06	10

The thermal hydraulic loop simulated has a total flow path length of 18.57 m, which contains 72 kg of water at the initial conditions. The simulation is run at constant mean pressure as the loop uses an accumulator to vary the mass of fluid in the loop to achieve this. The proposed start up procedure has the loop pressurized with steady flow before heating is applied to the test section. The pump operation schedule is held constant for the simulation. While the volumetric flow rate needs to be increased by 25% over the temperature rise from initial to steady state conditions to maintain constant mass flow, the time required for this, and therefore the scheduling function is unknown before the simulation is run. The effect of the reduced mass flow with time on the startup procedure will be compared to the constant mass flow case in future simulations. The heat exchanger is also required to be active whenever heat addition to the loop is present. Therefore, despite the energy penalty, and increased initialization time, cooling flow in the heat exchanger is present from the beginning of the simulation. The power applied to the test section is ramped linearly in time, increasing from 0 to 300 kW over 5 minutes. The defining parameters of the simulation are given in Table 4-7 below.

Table 4-6: Simulation Model Piping Definition

Part	ID [mm]	Wall Thickness [mm]	Added Thickness [mm]	Loss Coefficient
1.5" XXS Pipe	27.94	10.16	0	0
¾" 160 Pipe	15.6	5.535	0	0
90° Elbow	27.94	10.16	0	0.45
Grayloc T-joint	27.94	10.16	0	0.2
Grayloc Hub	27.94	10.16	2.41-15.6	0
1.5" XXS Flange	27.94	10.16	8.04-78.4	0
¾" 160 Flange	15.6	5.535	6.67-56.7	0

The temperature profile of the fluid in the loop, over time is presented in Figure 4-10 below. As the fluid is heated through the test section, the hot fluid exiting the test section is initially cooled by the piping connecting the test section to the heat exchanger. Once the pipe wall is sufficiently heated so that the temperature lag due to the pipe's thermal inertia is overcome, the hot fluid is able to start heating the heat exchanger. The heat exchanger has a thermal inertia that is greater than any of the other components, and is being actively cooled. This requires sufficient thermal inertia to be built up in the solid domain between the test section inlet and the heat exchanger inlet before the heat input in the test section is capable of raising the temperature of the heat exchanger's solid domain (480 s, Figure 10-3,j). Once the temperature of the heat exchanger begins to rise, the fluid temperature entering the test section is allowed to increase, and the loop resumes general heating.

Table 4-7: Simulation Parameters

Thermal-hydraulic Loop Characteristics			
T_o [°C]	p_o [MPa]	Flow Path Length [m]	Initial Fluid Mass [kg]
25	25	18.57	72.48
Forcing Functions			
	Initial Value	Max Value	Schedule
Pump [m^3/s]	1.24×10^{-4}	1.24×10^{-4}	$\dot{V} = \dot{V}_o$
Heater [kW]	0	300	$\dot{Q} = 1 \cdot t(s) + \dot{Q}_o$
Heat Exchanger Characteristics			
T_{in} [°C]	p_{in} [MPa]	Mass Flow [kg/s]	Shell Mass [kg]
29.5	0.1	1.25	60

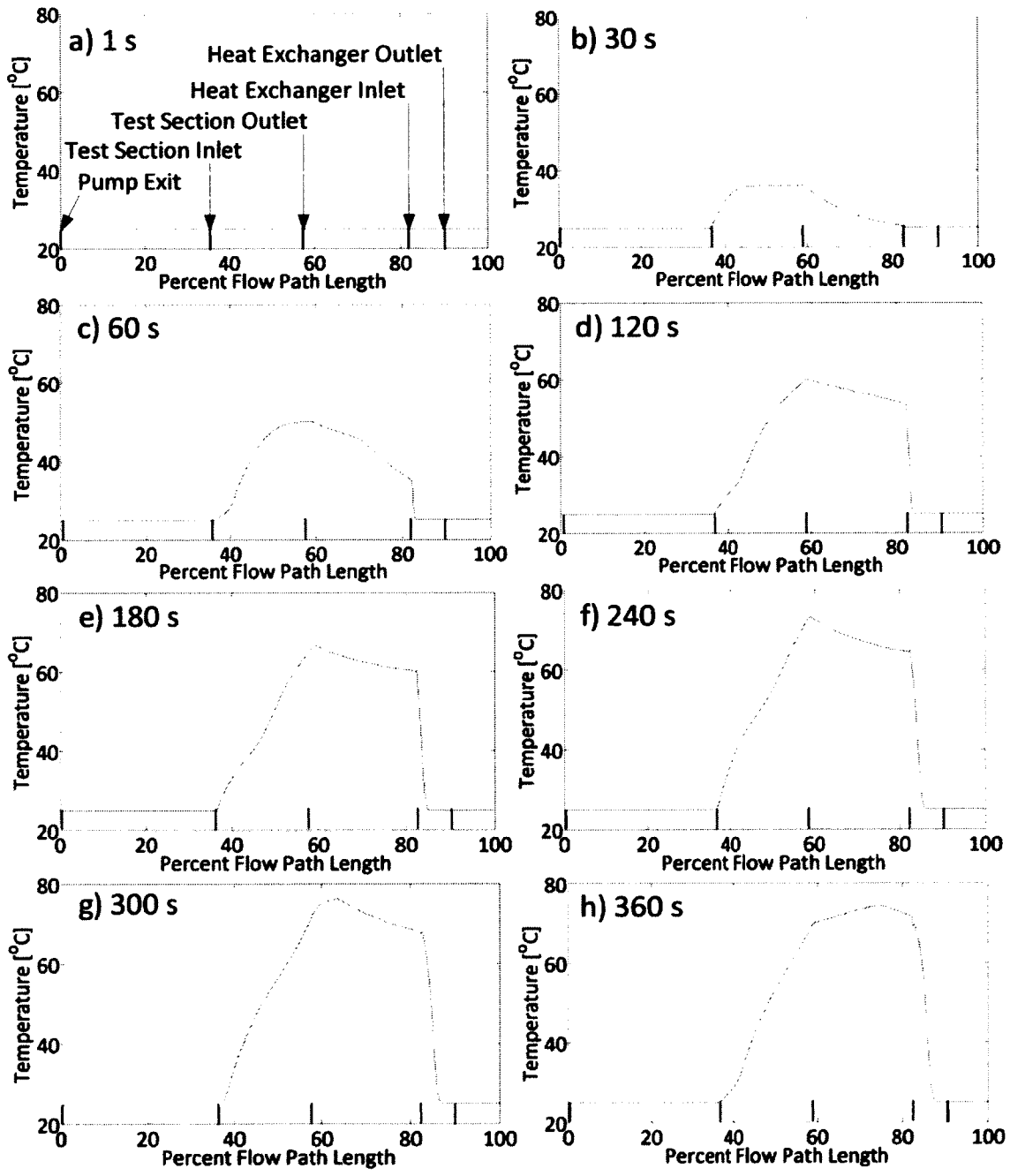


Figure 4-10: Fluid Temperature Profile

a) t=1 s, b) t=30 s, c) t=60 s, d) t=120 s, e) t=180 s, f) t=240 s, g) t=300, h) t=360 s

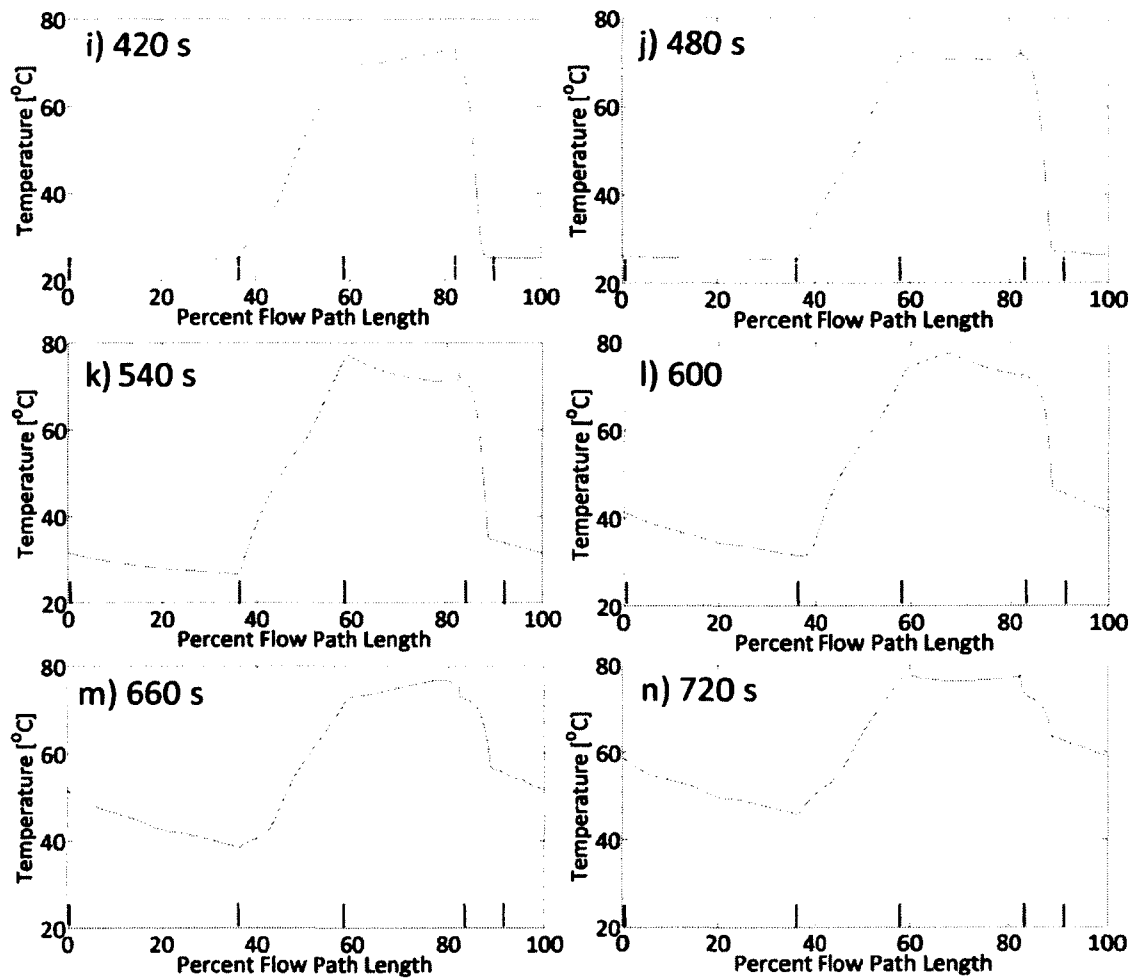


Figure 4-10: Fluid Temperature Profile

i) $t=420$ s, j) $t=480$ s, k) $t=540$ s, l) $t=600$ s, m) $t=660$ s, n) $t=720$ s

Focusing on the inlet and outlet nodes for the test section (Figure 4-11) and heat exchanger (Figure 4-12) the temperature response to the increasing heating with time is oscillatory in time. This is due to the lead-lag offset between the fluid with a direct heat source, and the solid wall that is heated by the fluid, each with their own thermal inertias. Demonstrated in Section 4.2 the fluid has a thermal time constant that determines maximum temperature change over a given time step. As the fluid is directly heated in the test section by a forcing function, this limitation is ignored. The effect of applying this forcing function is demonstrated in Figure 4-11. Modifying the model by moving the source function from the fluid to the component being

heated (heat rod or shroud) would remove the harmonics seen in the fluid temperature through the test section and should be implemented for future simulations.

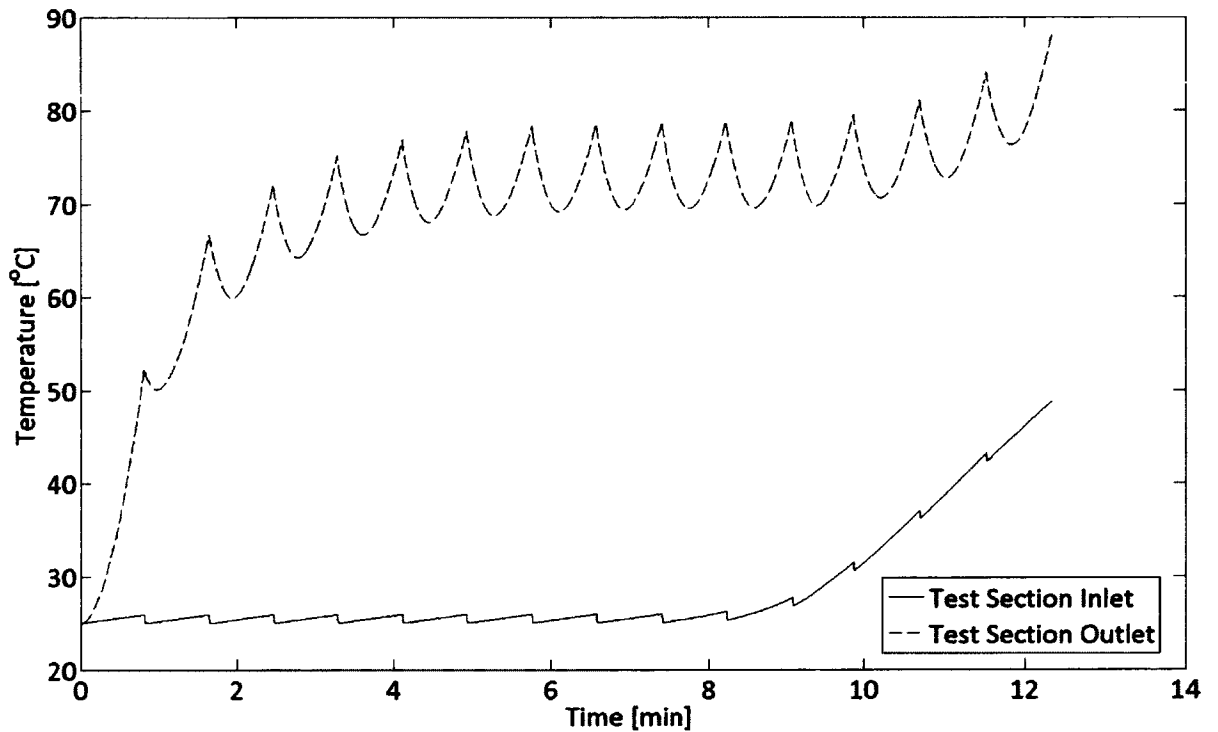


Figure 4-11: Temperature versus Time, Test section

The general trend of a sharp temperature rise, followed by a stable period while the thermal inertia induced lag in the heat exchanger is overcome, then resumed heating matches the behaviour seen in the overall fluid temperature profile. At the test section inlet the temperature is not perfectly constant with time as axial conduction in the solid domain allows heat to flow back to the cooler upstream region, where it preheats the fluid entering the test section until the fluid's heat source is no longer great enough to overcome the heat transfer from the fluid to the solid and the inlet temperature falls, starving the preheat effect. Thus the preheat effect due to conduction through the solid follows the oscillatory nature of the fluid heating. The diffusion effects due to conduction in the fluid are clearly seen comparing the fluid temperature at the test section outlet to the heat exchanger inlet. While the same oscillatory pattern is present at

the heat exchanger inlet, it has been diffused, removing the sharp peaks and valleys. The temperature oscillations are fully damped through the heat exchanger as seen by the smooth curve through time at the heat exchanger outlet, even after the temperature begins to rise.

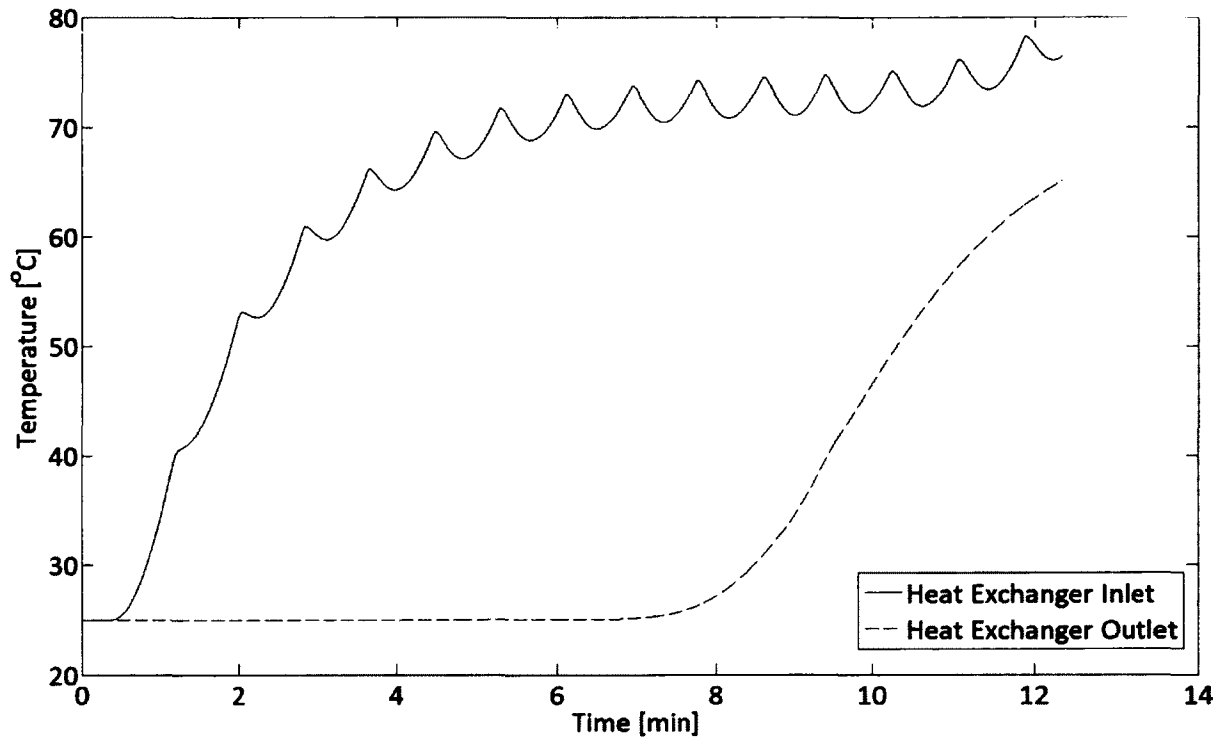


Figure 4-12: Temperature versus Time, Heat Exchanger

The results of the startup simulation demonstrate the general response of the thermal hydraulic loop as heat is applied to the loop initially at room temperature. The choice of applying a heat source to the fluid directly results in a numerically induced temperature oscillation in the fluid between the test section and the heat exchanger. This oscillation, while not changing the general response of the thermal hydraulics loop, is purely numerical and must be removed by modifying the location of the heat source before the results can be used for predictive purposes.

Chapter 5 Material Selection

5.1 High Temperature Alloys

The test section in the thermo-hydraulic loop will be subjected to extreme working conditions and will be expected to withstand both the thermo-mechanical loads and corrosive attack due to supercritical water being used as the working fluid. The base material of the loop must therefore have superior high temperature yield strength as well as exhibiting good corrosion resistance across all potential operating conditions (see Chapter 1). To simplify certification, material selection will be limited to those found in the ASME Boiler, Pressure Vessel, and Pressure Piping Code. With a maximum operating temperature of 650°C (1200°F), a survey of materials certified for this temperature for use in seamless pipe and tube produced the potential candidate materials; the top ten based on maximum allowable stress at 650°C are listed below in Table 5-1. On a pure strength basis, Inconel 625 is the best candidate due to its superior strength at elevated temperatures.

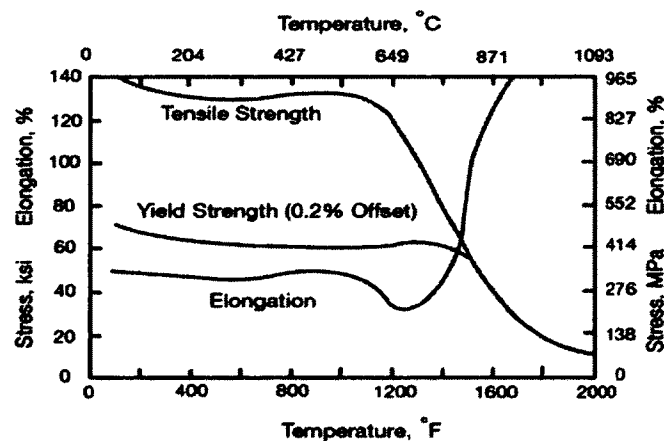


Figure 5-1: Tensile Properties of Annealed IN625 [44]

Comparing it to the other candidates it only stands out for its comparatively high Niobium concentration. Niobium is typically used for precipitation hardening in high temperature

superalloys [45][46][47][48]; however exhibits a phase change from γ'' -Ni₃(Nb,Ti,Al) to δ -Ni₃Nb at 650°C, resulting in a loss of the strengthening phase, shown in the knee of the tensile strength in Figure 5-1 above [44] [45][48]. To use a precipitation hardened alloy above its phase change temperature requires additional consideration to handle the large increase in deformation that accompanies loading at the elevated temperature, though it remains mechanically viable.

Table 5-1: Top Ten ASME Rated Materials at 650°C [49]

UNS Alloy Number Trade Name	Maximum Allowable Stress [MPa]	Nominal Composition (%wt) (B: balance) [44][50][51]										
		Al	C	Co	Cr	Fe	Mn	Mo	Nb	Ni	Ti	W
N06625 <i>Inconel 625</i>	133	0.40	0.10	1.0	20-23	5.0	0.50	8-10	3.15-4.15	B	0.40	-
N06617 <i>Inconel 617</i>	125	0.80-1.50	0.15	10-15	20-24	3.0	1.0	8-10	-	B	0.60	-
R30556 <i>Haynes 556</i>	94	0.2	0.10	18	22	B	1.0	3.0	-	20	-	2.5
S34809 <i>SS 348-H</i>	54	-	0.08	0.20	19	B	2.0	-	0.80	11	-	-
S34709 <i>SS 647-H</i>	54	-	0.08	-	17	B	2.0	-	0.80	11	-	-
S31700 <i>SS 317</i>	51	-	0.08	-	19	B	2.0	3.5	-	13	-	-
N08810 <i>Inconel 800-H</i>	51	0.15-0.60	0.10	-	19-23	B	1.5	-	-	30-35	0.15-0.60	-
S31651 <i>SS 316-N</i>	51	-	0.08	-	17	B	2	2.5	-	12	-	-
S30400 <i>SS 304</i>	42	-	0.08	-	18-20	B	2.0	-	-	8-11	-	-
N06600 <i>Inconel 600</i>	14	-	0.15	-	14-17	6-10	1.0	-	-	B	-	-

5.2 Corrosion

Additional requirements for a suitable material beyond strength are corrosion resistance and electrical resistivity behavior for any material to be directly heated. Corrosion resistance is crucial for safe long term operation of the loop. While corrosion behavior in water at subcritical temperatures is well understood, in the supercritical regime classically stable oxides may become soluble and therefore unsuitable. Studies on the formation of oxides and their stability

in a supercritical water environment suggest that constituents of the base material that are preferentially oxidized, such as Cr, to provide a stable passivation layer, are unstable across a temperature band seen by the test section resulting in a loss of the oxide and its protective effects. The results are demonstrated in Figure 5-2, showing the primary oxide growth followed by severe elusion and an effective zero growth steady state at 400°C, for high chromium steel. Increasing the temperature, the oxide evolution behavior becomes more favorable until a stable oxide layer is able to persist at 600°C.

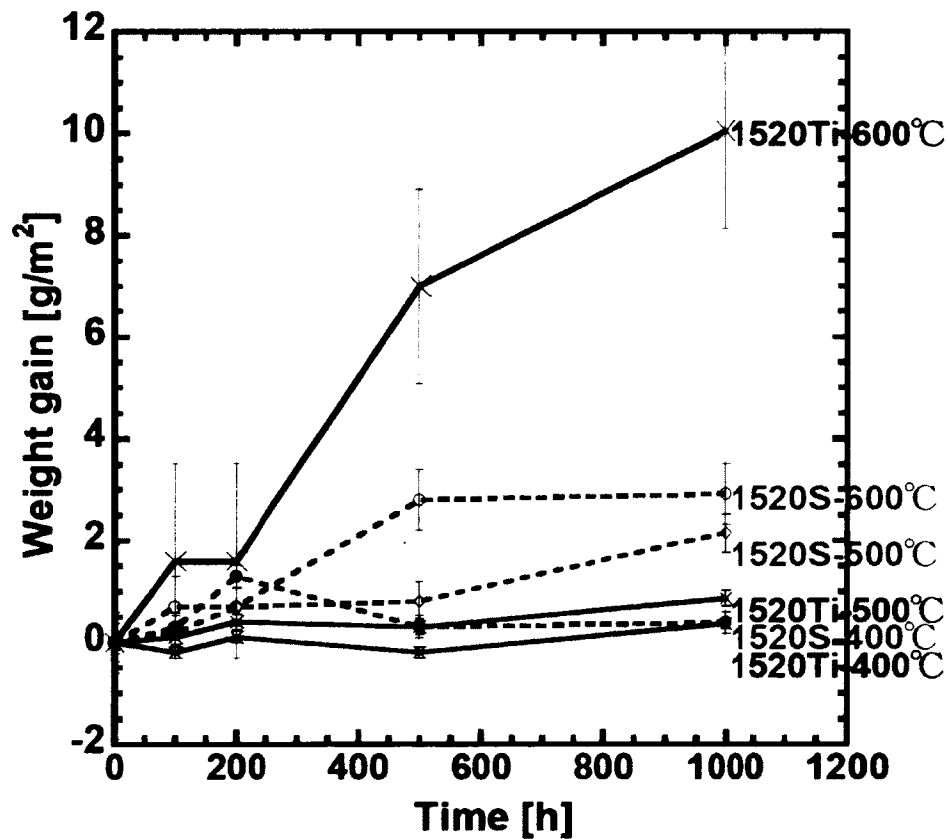


Figure 5-2: "Weight gain as a function of corrosion time for 1520S and 1520Ti exposed to supercritical water at 400, 500, 600oC, <1000h" [52]

Also of interest in the study is the potential for alloying elements, added for strengthening effects, which may lead to accelerated oxide growth. Studies focusing on nickel based

superalloys, including Inconel 625, show that while the slope of the oxide weight gain is positive across all temperatures for all time, oxide growth never levels off [53][54]. The growth rate for these materials increases with temperature, leading to an oxide spalling failure mechanism [53]. Comparing the different behavior of the austenitic steel to the nickel based superalloys, it appears that the lack of iron in the superalloys allows for the formation of a relatively stable NiO oxide layer as the Cr_2O_3 dissolves into the supercritical water, improving the material's oxidation resistance between 400 °C and 500 °C. While the oxidization behavior and oxide stability in supercritical water is an active field of research [55], the current data suggest that Inconel 625 has sufficient oxidization resistance to suit the test section requirements.

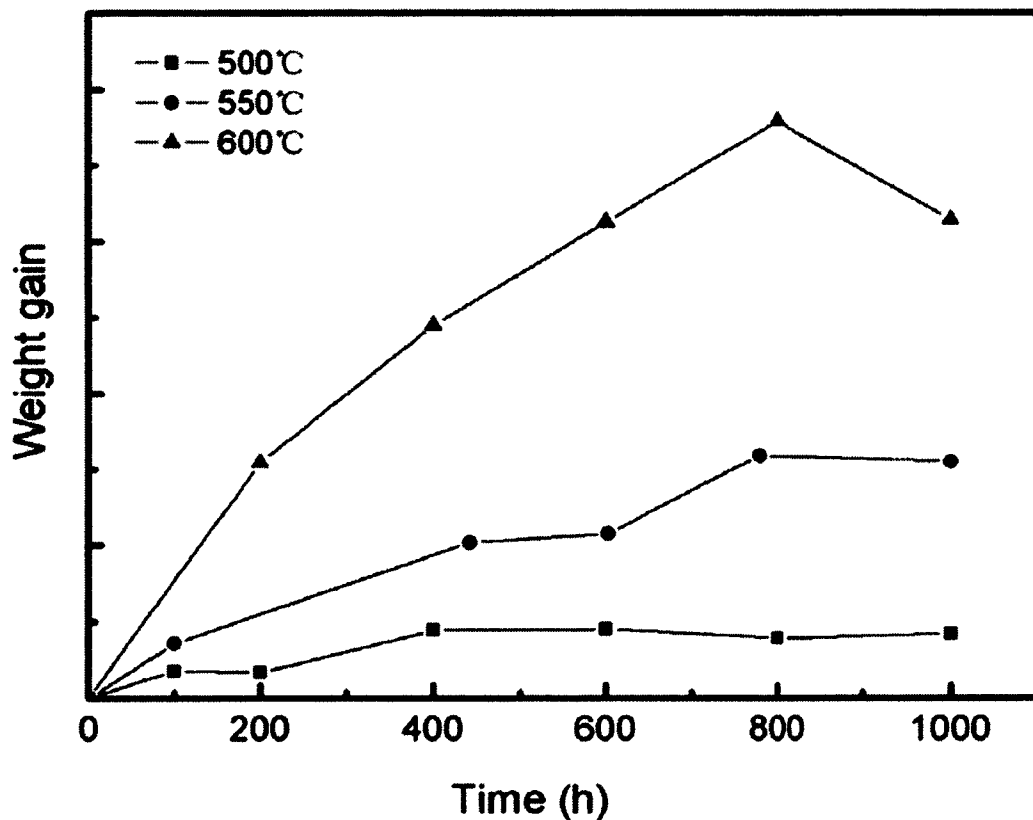


Figure 5-3: Typical Weight Gain of a High Chromium Nickel Superalloy [53]

5.3 Ceramic Coatings

Oxide stability is also of critical importance for any coatings to be exposed to the fluid. Coatings exposed to the fluid will be primarily used for electrical insulation and corrosion resistance; yet they need to be capable of conducting heat efficiently too. If the coating is also highly porous then the behavior of the underlying coatings or material must also be considered. A brief review of literature dealing with ceramic stability in supercritical water suggests that pure sintered alumina has superior corrosion resistance, while some types of stabilized Yttrium ceramics may also prove acceptable [56][57][58]. Silica-based ceramics do not perform well and others disintegrate entirely [56]. Zirconia ceramics are typically used as a thermal barrier coating due to their low thermal conductivity and high porosity, making them undesirable as an insulator between the electric heating element and the fluid. Alumina in contrast has an excellent thermal conductivity and sufficient dielectric strength, while also exhibiting good bonding to substrate alloys. With no drawbacks, alumina (A1) is the natural choice for dielectric coating applications in the test section, and has been used in other supercritical water thermal-hydraulic applications [59]. The properties of alumina are listed in Table 5-3 below.

Table 5-2: Comparison of Ceramic Coating Applicability as Electrical Insulators [44] [60][61]

Material	Thermal Conductivity [W/mK]	Dielectric Strength [kv/mm]
99.6% Aluminum Oxide	35	16.9
94% Aluminum Oxide	18	16.7
MgO Stabilized Zirconia	2	2-10
Y ₂ O ₃ Stabalized Zirconia	2	-
Fused Silica	1.38	30
Silicon Carbide	120	Semiconductor
Inconel 625	9.8-16.2	N/A
Inconel 600	14.9-27.5	N/A

Table 5-3: Mechanical Properties of Alumina at Room Temperature [61]

Grade	Purity [min%]	Thermal Expansion [10^{-6} K^{-1}]	Conductivity [W/mK]	Resistivity [Ωm]	Flexural Strength [MPa]	Flexural Strength @ 700 °C [MPa]
A1	99.6	5.4	30-40	10^{14} - 10^{16}	210-500	-
A2	99.8	5.4	30-40		150-450	-
A3	99.5	5.4	30-40		300-600	-
A4	99.6	5.4	25-23		150-450	-
A5	99.0	5.4	30-40	10^{14} - 10^{16}	150-500	-
A6	96.5-99.0	5.1-5.4	25-30		150-450	-
A7	94.5-96.5	5.1-5.4	20-30	10^{14} - 10^{16}	180-360	240-360
A8	86.0-94.5	4.9-5.5	15-20	10^{13} - 10^{16}	150-350	250-325
A9	80.0-86.0	4.5-5.5	15-20		200-300	-

A ceramic will also be required to act as the resistive heating element for the annular and 7-rod-bundle test sections as discussed in Section 5.4, and in detail in Chapter 6. As ceramic coatings are already being considered for dielectric insulation, an additional ceramic coating may be applied to act as the heating element, with its properties tailored to the power supply's constraints. The ceramic chosen to act as the heating element is Kanthal Super (MoSi_2), which is capable of being applied by plasma spray [62]. While an oxidizing environment is favorable for the operation of Kanthal Super, it will be utilized with a protective alumina coating, for corrosion and dielectric resistance, so only its electrical properties will be considered.

5.4 Electrical Resistivity and Conductor

For the test sections that are to have a pressure vessel double as the resistive heating element as well (see Chapter 6 for further details), stability of the materials electrical resistivity over the experiments temperature range is desirable to promote a uniform heat generation along the test section's length. Examining the resistivity behavior of three candidate alloys in Figure 5-4 reveals while Inconel 625 has superior strength characteristics, Inconel 600 has the most stable electrical resistivity over the applicable range of temperature, especially between 600 and 800 °C. For high powered tests the geometry of the test sections preclude the use of the base metal

of the pressure vessels as heating elements as their resistance is poorly matched to the power supply. These concerns will be investigated in detail later in Chapter 6; however, it is sufficient for the purpose of material selection that a different heating element is required.

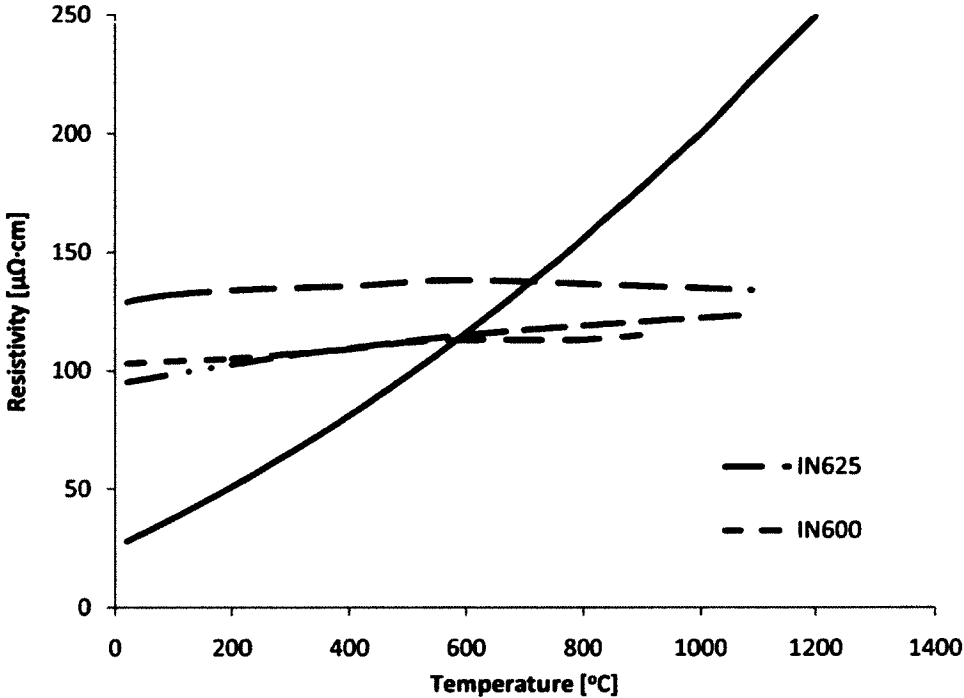


Figure 5-4: Temperature versus Electrical Resistivity for Selected Superalloys and Ceramics [44][51][59][61]

Comparing the resistivity versus temperature profile of the Kanthal 1700 material to the super alloys, the ceramic would appear to be undesirable as it experiences a large variation in resistivity over the temperature range shown. However, the geometry is independent and highly controllable, due to Kanthal being applied by plasma spray. Therefore the variability in electrical resistivity can be accounted for through design. Kanthal, as a product designed for heating elements, has the additional advantage of its high temperature behavior being well known, which allows for better predictability and control during the design process compared to a metallic alternative.

The electrical conductor of choice is copper for its dramatically lower cost compared to silver, which is only slightly superior as a conductor. Copper is also easily machinable and can be applied using a plasma spray process. While the melting point of copper is above 1000 °C, its strength at elevated temperatures is poor, as shown in Figure 5-5. Since the copper used in the test sections will have no structural role, the lack of mechanical strength across the thermal-hydraulic loop's operating temperature range will not impact the copper's performance. The reduction in yield strength will prove advantageous in instances where the copper is used as a gasket material as detailed in Chapter 6.

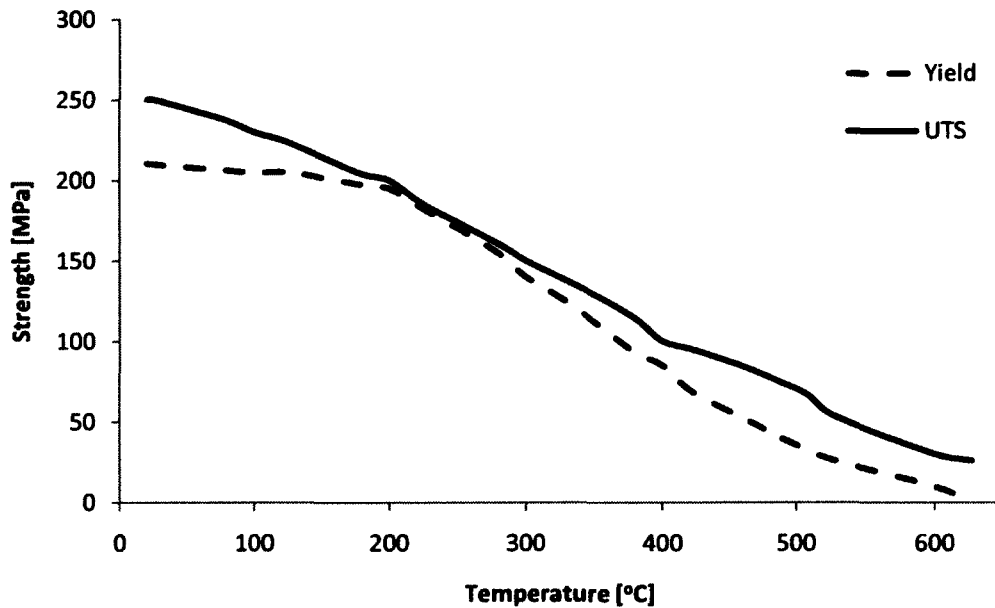


Figure 5-5: Copper Tensile Strength versus Temperature [63][64]

Based on the designs presented in Chapter 6, no copper will be exposed to the working fluid, therefore no consideration will be given to its susceptibility to corrosion in supercritical water. Given its desirable electrical properties and acceptable mechanical properties, copper is superior to silver given the cost difference compared to the potential performance difference.

Chapter 6 Preliminary Test section Design

6.1 Background

As described in Chapter 1, a number of thermal-hydraulic loops with capacity for studying heat transfer in supercritical fluid have been deployed around the world. The focus of these studies share similar goals to the work planned for the supercritical thermal-hydraulics facility at Carleton University: the investigation of heat transfer phenomena as applied to power generation. Topics of interest range from basic heat transfer studies in supercritical fluid to the impact of specific geometry on cycle efficiency. To carry these studies out, different test sections are to be employed in the Carleton thermal-hydraulics loop with the aim of isolating different phenomena or geometry effects.

Many basic heat transfer studies have been carried out with supercritical carbon dioxide, using simple tubular geometries for the test section [65]. Carbon dioxide is a popular fluid for supercritical studies as it has a lower critical temperature and pressure than water. While providing important information pertaining to general heat transfer in supercritical fluid, these apparatus are unable to utilize the working fluid of interest to the Carleton research group (water), nor operate to the desired temperature and pressure. With the recent interest in using supercritical water (SCW) for decomposing organic waste [66] and to improve efficiency in power generation[1], other facilities have been built to study supercritical water. Of particular interest are the facilities that operate a heated test section and how they handle the test section integration along with power delivery.

Carleton's primary industrial partner with the supercritical thermal-hydraulics group is Atomic Energy Canada Ltd. (AECL). Their principle thermal-hydraulic experimental apparatus centers around a 37-element bundle simulator consisting of 12 bundles [59]. The experiment is

concerned with determining critical heat flux and dryout effects for current sub-critical reactors, and as such is unable to be operated at supercritical temperatures and pressures. It is one of the goals of the Carleton group to be able to extend the work done by AECL to the supercritical region as applicable to the Generation IV Nuclear Program. It is therefore important to maintain similarity between test sections, such as unheated entry length and instrumentation capability, to facilitate comparison between data sets. These parameters will be further examined as applied to the Carleton design and other designs currently in operation, with particular interest being given to the ability to measure wall temperature along the entire length of the heated section as done by AECL with their sliding thermocouple design (Figure 6-1).

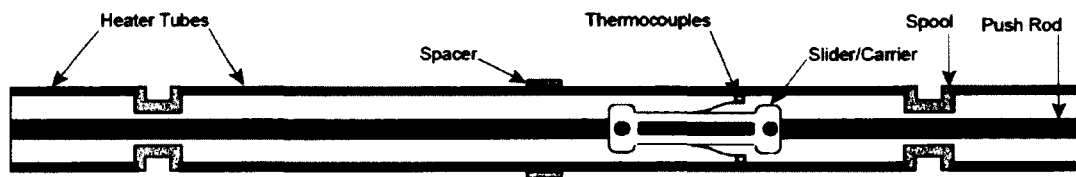


Figure 6-1: "Sliding Thermocouples Assembly and Carrier." [59]

At the University of Wisconsin (UW) a heat transfer facility was constructed to simulate and study heat transfer phenomena in supercritical water nuclear reactors [7][67]. The facility is designed to operate at 25 MPa with a maximum water temperature of 410 °C while studying flows in the vertical orientation, either up- or down-flow. The thermal-hydraulic loop is shown in Figure 6-2, with all major components labeled. The test section occupies a short length (1.01 m) of the internally-heated section and is mounted in line with the flow using Grayloc fittings.

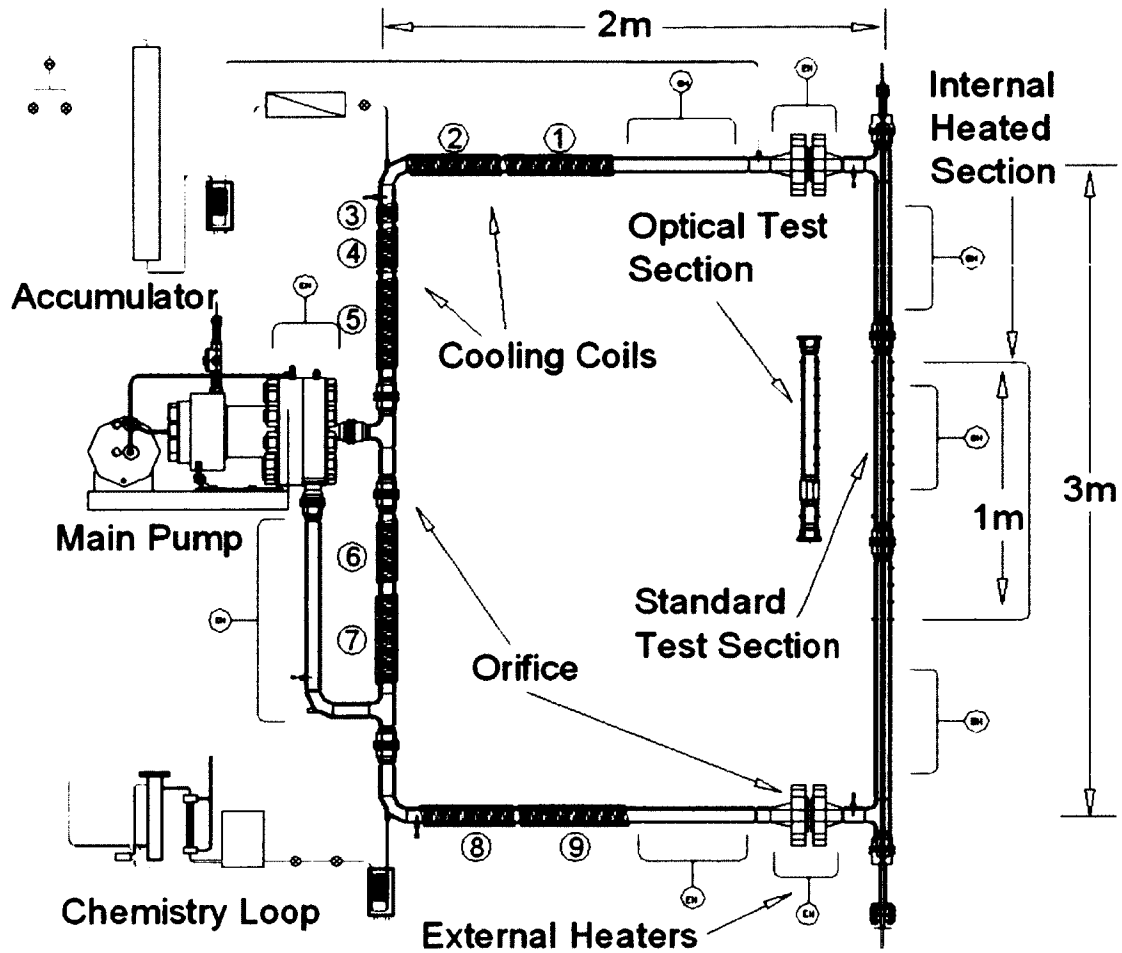


Figure 6-2: "Heat Transfer Loop" [7]

The test sections are of either a circular annular or square annular type with hydraulic diameters of 32.2 mm and 19.9 mm respectively. The inline mounting configuration creates a fixed entry length of 760 mm, which results in an unheated entry length significantly shorter for both test sections than the 50 diameters that is standardized at AECL [59]. The fluid is heated by direct current electric resistive heating with the heater rod projecting out both ends of the internal heated section. The heater rod is designed around a typical fuel pin of a nuclear reactor with the maximum heat flux (1500 kW/m^2) set to be just higher than the expected maximum for a power generation application. The electric power is dissipated by a heating element filament contained in an IN600 tube, which is electrically insulated from the rest of the loop across the entire power

length. Despite the heater rod being accessible at both ends, the heater rod design (Figure 6-3) uses an array of 16 stationary thermocouples, sandwiched between the sheath and cladding. This limits the temperature field to a resolution of 67.33 mm axial spacing with a single radial position at each node. Given the high degree of nonlinearity in fluid properties near the critical or pseudo-critical point, as well as the potential non uniformity of heat transfer effects in the radial direction (eg: buoyancy effects in the horizontal orientation), the fixed thermocouple design is less desirable than the AECL sliding thermocouple design.

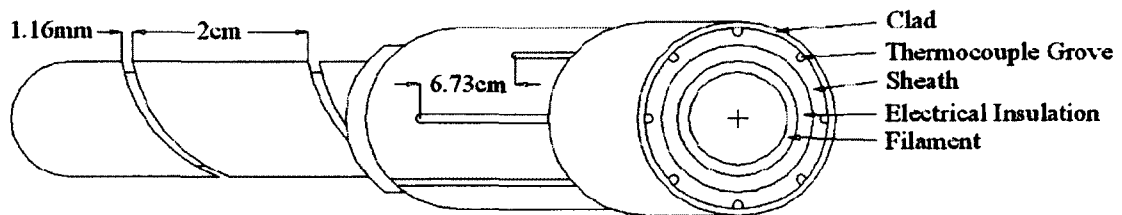


Figure 6-3: "Heater Schematic." [7]

Due to thermal expansion issues in the heated section one end of the heater rod was fixed while the other was left to slide freely. At the fixed end, after the piping was stepped down and actively cooled, a graphite compression fitting was employed (Figure 6-4). While capable of meeting the UW loop's operating temperature and pressure, graphite is not compatible with SCW, suffering the same rapid corrosion rate as silicas, discussed in Chapter 5, so the water needed to be cooled until no longer reactive with the graphite.

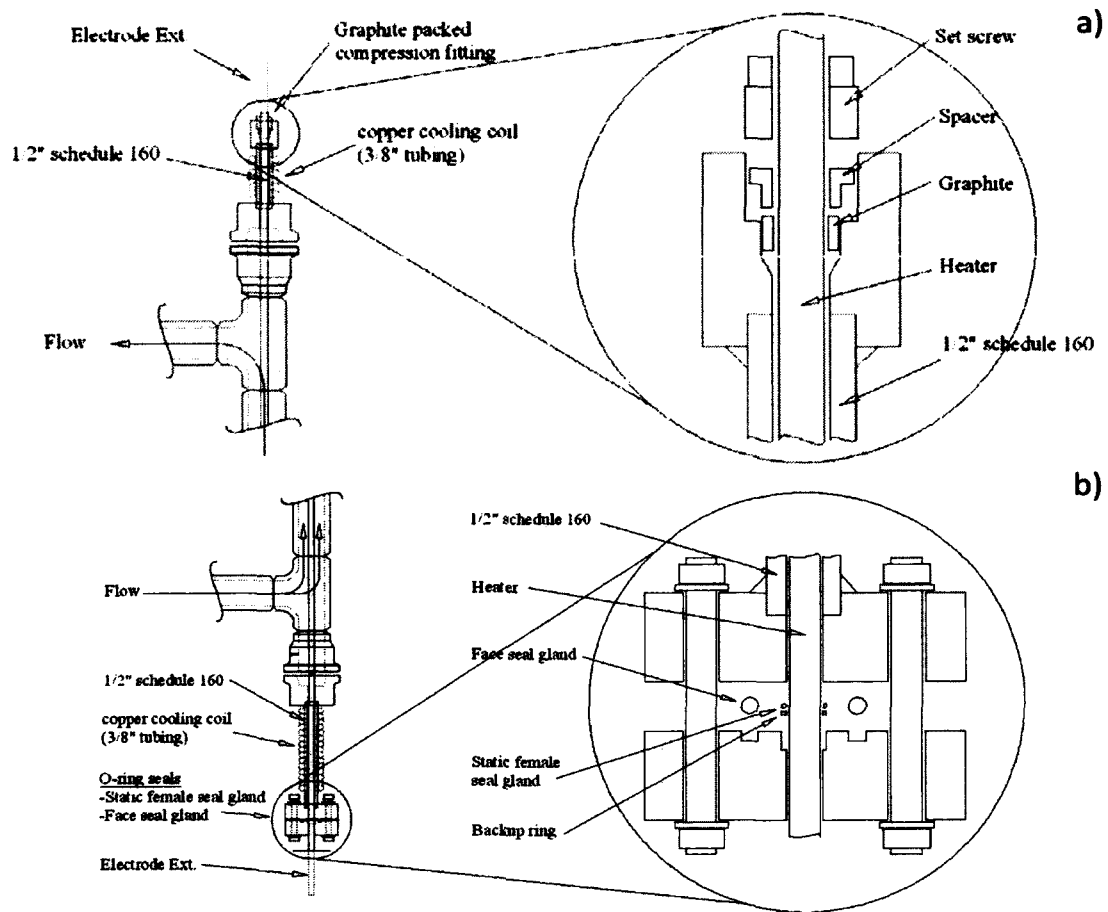


Figure 6-4: "Pressure Boundary." a) Fixed Position, b) Allowing Differential Expansion [7]

The opposite end is also actively cooled to allow the use a flanged terminator with typical elastomer seals. Shown in Figure 6-4 above, the flange face is sealed with an o-ring seal, while two additional rings with low coefficients of friction are used to form a seal between the heater rod and its mating flange while permitting sliding contact. The use of active cooling in the UW SCW loop allows for the use of common sealing methods while accounting for the thermal expansion mismatch between the heater rod and surrounding piping. Since the loop uses cooling coils fed with building water as the main form of heat rejection, adding active cooling to the pressure boundaries did not impose any additional requirements on the facility.

Another SCW thermal-hydraulics loop of pertinent interest was built at Xi'an Jiaotong University (XJU) to study heat transfer using a heated circular rod with a wire wrapped spacer in both circular and square annular channels [25]. The operating conditions of the loop are very similar to those of the UW SCW loop, with a maximum pressure of 25 MPa and fluid temperature not exceeding 415 °C. Of particular interest, the maximum component temperature of the loop never exceeds 550 °C (800 kW/m² maximum heat flux) which suggests that for other similar loops (such as the UW SCW loop) this maximum component temperature will be fairly consistent across current designs. Detailed below, the experiments to be carried out at the Carleton facility may require that the maximum component temperature reach 870 °C or even higher; a requirement that places an additional challenge on the test section designs for the Carleton SCW loop not present in previous work.

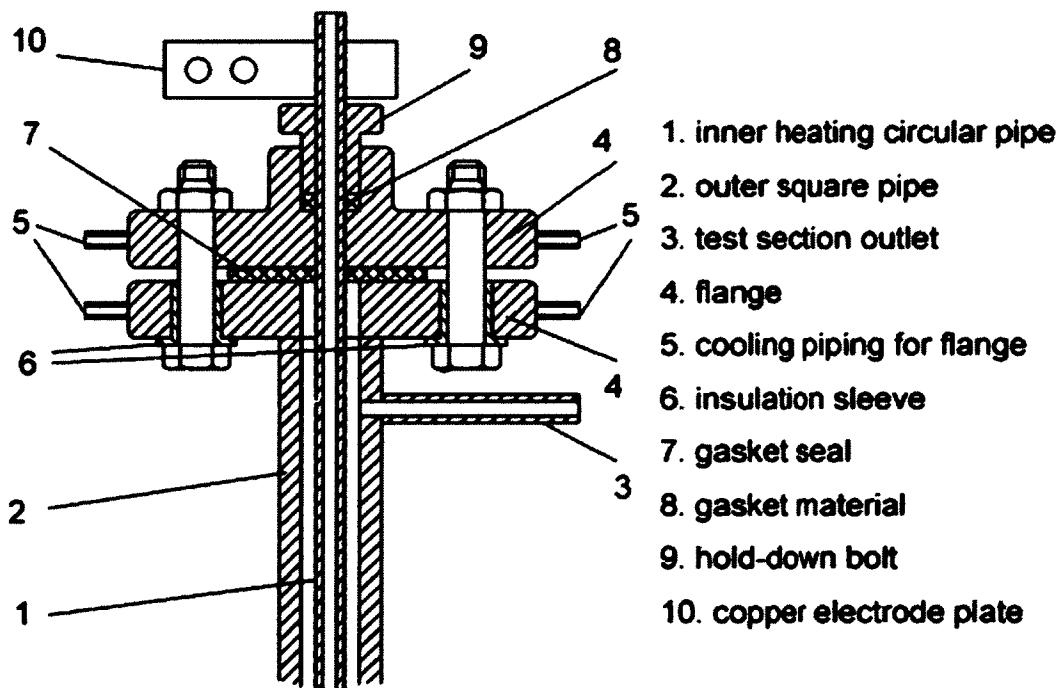


Figure 6-5: "Leak-proof seal and insulation structure of the [Xi'an Jiaotong] test section" [25]

A simplified approach to heating the fluid is used in the XJU SCW loop compared to the layered heating filament, insulation and sheath found in the UW SCW loop: alternating current is directly applied to the inner pipe, where the resistance of the metal is used to dissipate the electric power to heat. This has the effect of producing uniform heating along the entire length of the inner pipe. While a short length is provided from the inlet before measurements are taken, there is no unheated entry length in the XJU SCW loop test section design. The XJU SCW loop takes a similar approach to both instrumentation and sealing the heated rod pass through as the UW SCW loop. Eighteen thermocouples are evenly spaced (130 mm) along the internal wall of the heated rod yielding a further reduced spatial resolution; though due to the increased test section length (1.48 m) the relative spacing is similar, 8.8% versus 6.6% respectively. Active cooling is also used on the flange joints where the heated rod passes through the pressure boundary in the XJU SCW loop, however the flanges themselves are cooled, eliminating the need for a step down pipe. The specific gasket material is not given in the publication, however given the active cooling, any number of materials could be used as demonstrated in the UW SCW loop. The heating method chosen, using the inner pipe as the resistive element, presents the additional challenge of electrically isolating the remainder of the test section, as metallic contact between the heated rod and flange would otherwise result in undesirable stray current flow. This is examined in detail below as it also applies to the Carleton SCW loop test section designs.

Additional SCW facilities exist at: the University of British Columbia, Kyushu University, IPPE in Obninsk, Russia, and the Kiev Polytechnica Institute; however they are all similar in design to the UW and XJU SCW loops concerning their application to heat transfer studies[27] [66][68]. A common trend of the supercritical facilities (both water and carbon dioxide) reviewed is the focus on heat transfer near the critical or pseudo-critical point in annular or tubular test

sections. Total power delivered, and temperature rise, in the test section tends to be modest compared to the design specified for the Carleton facility, outside of the IPPE facility. There exists the opportunity to extend the available experimental data currently available by the Carleton group, by employing test sections capable of extending the current range of temperatures and pressures operated within by the above groups. The test sections detailed below for use by the Carleton supercritical fluids group are designed to take advantage of the full power available at the facility to heat the fluid in the test section, while being capable of operating up to 28.35 MPa and 625 °C. The designs will also offer provisions to meet AECL standards concerning instrumentation and fluid conditioning before heating.

6.2 Test section Geometry

Three test section designs are initially called for to satisfy the current experimental goals at the Carleton supercritical facility: tubular, annular and a 7-rod-bundle (Figure 6-6). This will allow a range of experiments to be carried out, from qualification and fundamental heat transfer to investigating spacer type and sub-channel design effects. A 7-rod-bundle design was chosen as it matches the core design of the Bruce 37-element fuel bundle, which is of interest to Carleton's industrial partner AECL [59]. The annular and tubular geometries provide a common geometry type to those currently employed by other groups around the world. This allows for initial, simplified experiments to be compared to the existing data for qualification and validation purposes while the Carleton group establishes itself.

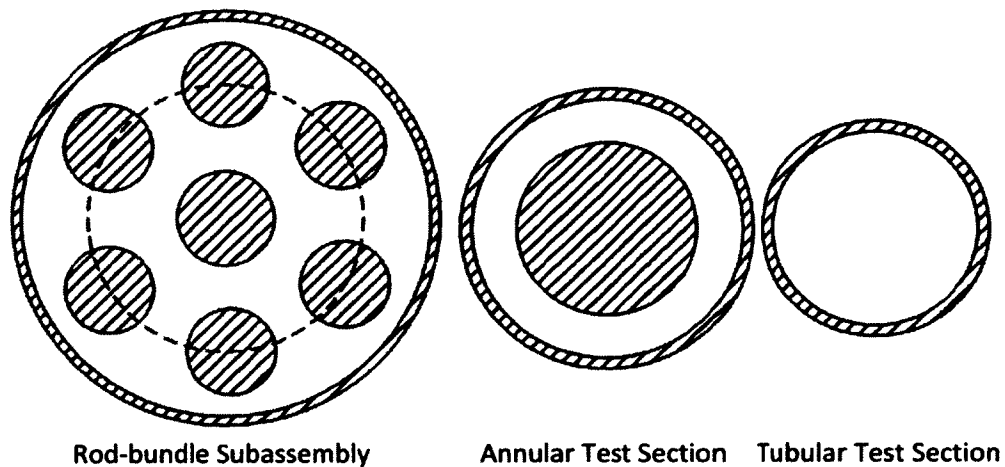


Figure 6-6: “Cross Section of Test section [Types]” [69]

To meet the experimental standards set forth by AECL, for the 7-rod-bundle and annular test sections a sliding type thermocouple is to be employed. This will allow for a complete temperature map of the heated rods to be made during an experiment and provide a superior resolution of heat transfer phenomena occurring in the test section. The detailed design of the instrumentation system for the Carleton SCW loop lies beyond the scope of this work.

Anticipating the needs of the instrumentation, provisions will be made for each test section design with internal heated elements to allow for the implementation of a sliding thermocouple. The detailed design of each test section is presented below.

6.2.1 Loop Interface

Two thermal-hydraulic loops were designed, as outlined in Chapter 1, to study supercritical fluid behaviour at Carleton University; one for water and the other for R134a. The test sections themselves, along with the other work presented in this thesis, are focused on the application of studying heat transfer effects in supercritical water. As the loops share many physical characteristics, and R134a requires a less severe environment, there is no reason the test sections could not be used across both loops. For this reason, and to simplify the

interchangeability within the supercritical water loop, all the test sections are designed to match a common connection arrangement.

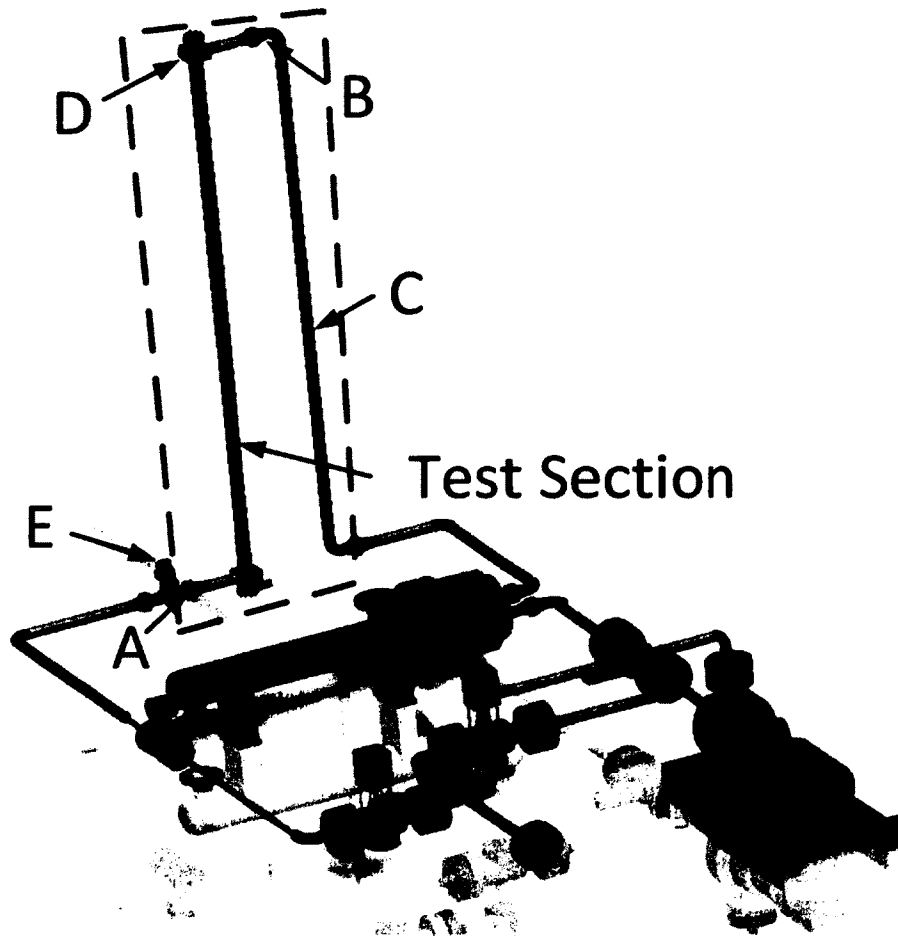


Figure 6-7: Test section Loop Interface [5]

Shown in Figure 6-7, the test section, highlighted in the dashed red box, connects to the thermal-hydraulic loop through a standard Grayloc hub, at points A and B. Test sections are designed to be symmetric with repeated parts to simplify both manufacturing and to make incorrect assembly impossible. An additional advantage of the symmetric design and Grayloc connections, is that the pipe segment C and the test section may be reversed in order to investigate the effects of flow both in the direction of gravity and against.

To achieve the desired interchangeability and flexibility, a number of parameters are fixed across the different test sections; these can be found in Figure 6-8 and Table 6-1. Due to a height restriction imposed by the lab space, the length of the test section assembly and the test section itself are limited to 2.54 m and 2.38 m respectively. This has a varying degree of impact on the different test section configurations as discussed below. The inlet and outlet blocks are also fixed in size to accommodate the piping and Grayloc hub, set by the loop, as universal connectors. One of the blocks, D in Figure 6-7, has a quarter inch port opposite the inlet/outlet bore, Figure 6-9, to allow for a pressure sense line to be installed and connected to the opposite end of the test section through a port at location E, Figure 6-7. The remaining components of each test section are allowed to vary according to their design.

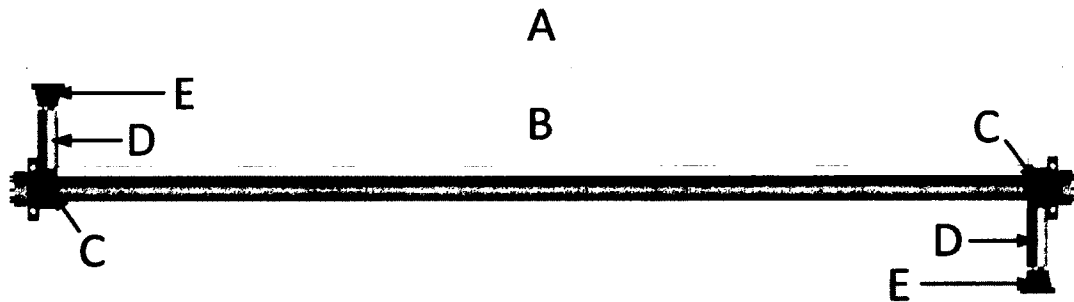


Figure 6-8: Common Test section Elements

Table 6-1: Common Test section Elements

Part Name	Figure Label	Dimensions		
Test section Assembly Length	A	-	-	Length: 2439 mm
Test section Length	B	-	-	Length: 2329 mm
Inlet/Outlet Block	C	Width: 100 mm	Height: 100 mm	Length: 55 mm
1.5" XXS Pipe	D	OD: 48.26 mm	ID: 27.94 mm	Length: 152.4 mm
Grayloc Hub	E	Grayloc Hub (1-1/2GR11)		

The inlet/outlet block is sized to accommodate all possible parts attached to it while retaining sufficient wall thickness to handle the peak fluid temperature and pressure of the loop. The minimum wall thickness was determined by the necessity to be able to penetrate the pressure vessel and attach a pressure sense line, detailed in Section 6.4 below. Each block is oriented locally with the front face set by the bore used to mate the block to the test section shroud (Figure 6-9). A centering ring is used to align the 1.5" XXS pipe which is to be permanently fixed to the block. Table 6-2 lists the unique features of the inlet/outlet blocks used for the different test sections. Both the Grayloc hub and 1.5" XXS pipe, as common loop components, are the same as discussed in Chapter 1.

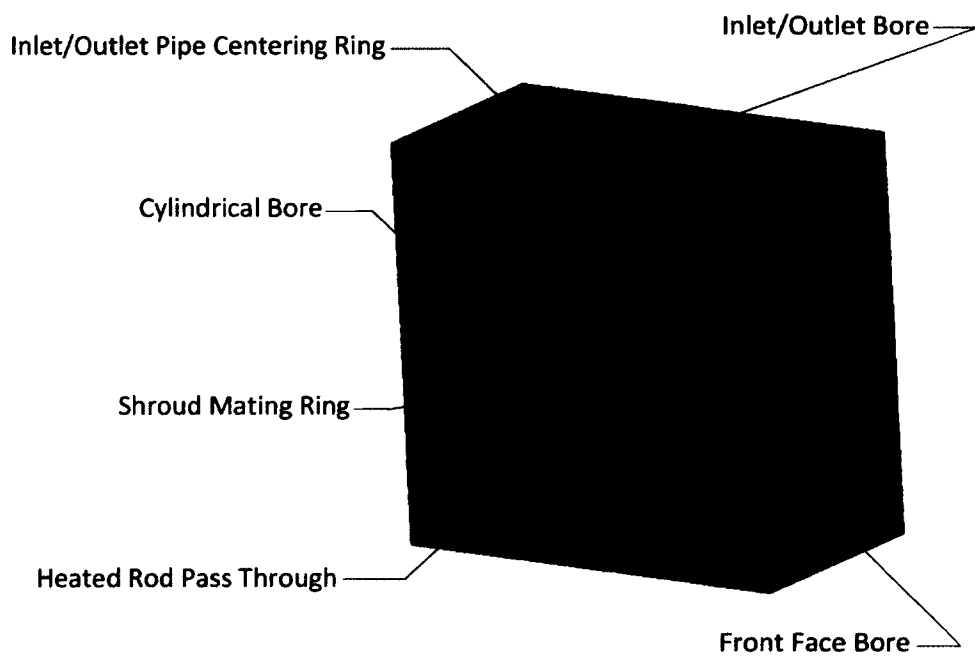


Figure 6-9: Inlet/Outlet Block, 7-Rod-Bundle Test section

Table 6-2: Inlet/Outlet Block Elements Across Each Test section

Test section		7-Rod Bundle	Annular	Tubular
Inlet/Outlet Bore	Diameter [mm]	27.94	27.94	27.94
	Depth [mm]	Through	Through	Through
Front Face Bore	Diameter [mm]	60.33	42.16	11.45
	Depth [mm]	11.03	9.00	Through
Cylindrical Bore	Diameter [mm]	58.19	58.19	N/A
	Depth [mm]	27.94	27.94	N/A
Heated Rod Pass Through	Diameter [mm]	11.45	11.45	-
	Number	7	1	0

6.2.2 7-Rod-Bundle Test section

The 7-rod-bundle test section is geometrically the most complex test section to be utilized; it most accurately simulates the flow arrangement found in a CANDU fuel bundle [59]. The 7-rod-bundle can be used to investigate heat transfer in sub-channel flow as well as being extended to study the effects of different spacer designs. Since spacer design has not been considered at the current stage of the supercritical water thermal-hydraulics experiment and represents a separate area of study to be pursued in future work, it will not be considered further. Future work may incorporate any spacer design without additional modification to the test section design, and no change in mechanical or electrical performance, so the spacers may be neglected with no loss of generality to the design of the test section.

Table 6-3: Internal Component Geometry Comparison, 7-Rod-Bundle Test section

	Shroud ID [mm]	Heated Rod OD [mm]	D_h [mm]	Flow Area [mm ²]
Initial Specifications	28	7	5.73	346
Modified For Instrumentation	40.07	11.45	5.73	580
Modified with 2" SCH 160 Shroud	42.91	11.45	7.50	725
Modified with 2" XXS Shroud	38.18	11.45	4.56	424

The initial experimental specifications called for a 7 rod assembly with a shroud inner diameter of 28 mm and a hydraulic diameter of 5.73 mm. This would have necessitated the heated rod's diameter to be too small to allow for internal instrumentation necessary for heat transfer study. To maintain dynamic similarity the hydraulic diameter was fixed while components were scaled up. To meet the requirement of passing instrumentation internally through the test section, heated rods with an internal diameter of 8.95 mm were chosen, with an outer diameter of 11.45 mm to provide the necessary wall thickness demanded by the maximum operating temperature and pressure. To match the specified hydraulic diameter the shroud's inner diameter would be 40.07 mm, as shown in Table 6-3 above. This internal diameter is not available based on the nominal pipe size (NPS) specifications; using a NPS pipe is desirable to avoid cost and certification requirements with using custom parts. A 2" NPS schedule (SCH) 160 or double extra-strong (XXS) provide a pipe with a very similar internal diameter, the SCH 160 being larger and the XXS smaller. Using 2" XXS piping provides the best compromise between using a standard pipe size and maintaining the desired hydraulic diameter. The reduced flow area, in conjunction with the reduced hydraulic diameter has additional advantages for the scope of the heat transfer experiments possible with the test section for the power available, described below in Section 6.3.1. In addition to the cost savings gained from using standardized parts, using the double extra-strong standard allows a greater number of materials to meet the ASME safety standards, including stainless steels which are significantly cheaper than super alloys that would be required by a thinner walled shroud.

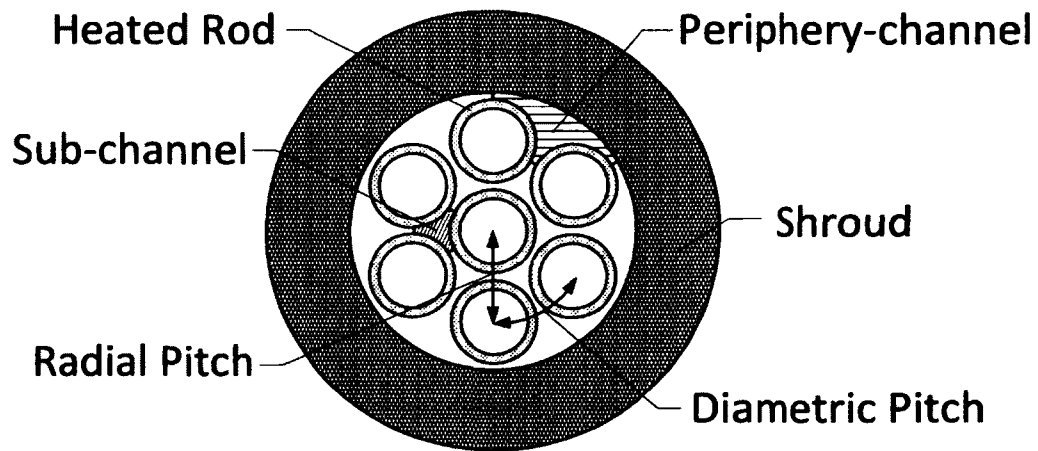


Figure 6-10: 7-Rod-Bundle Test section Cross Section

Table 6-4: 7-Rod-Bundle Test section Geometry

	Outer Diameter [mm]	Inner Diameter [mm]
Shroud	60.33	38.18
Heated Rod	11.45	8.95
Radial Pitch [mm]	12.41	
Diametric Pitch [mm]	6.50	
Heated Rod Spacing δ [mm]	0.9575	

Considering the compromises and advantages offered by using a NPS 2" XXS pipe for the 7-rod-bundle, the benefits justify the modification to the test section specifications, with the resulting internal geometry shown in Figure 6-10 above. The resultant rod spacing channel geometries are detailed in Figure 6-11. As consequence of the circular cross section of the shroud, the periphery-channel has a significantly larger flow area and hydraulic diameter (Table 6-5) which will result in flow rates being unevenly split between the core and periphery of the test section, favouring the periphery. The reduced flow rate in the core, coupled with the dominating heated surface area to volume ratio of the core versus the periphery will cause the core fluid to heat much faster than the periphery flow. The resultant temperature distribution of the fluid will result in the center heated rod being subjected to a higher temperature than its surrounding

neighbors. The effect of uneven temperature distribution on the test section performance will be detailed in Section 6.3.2.

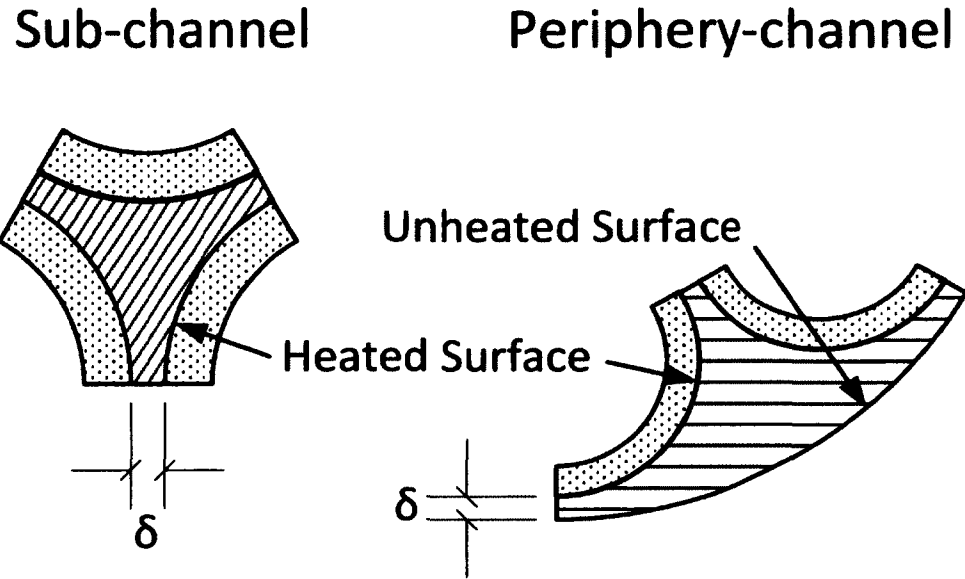


Figure 6-11: 7-Rod-Bundle Sub-channel and Periphery-channel Cross Section

Table 6-5: Sub-channel vs Periphery-channel Geometry

	Flow Area [mm ²]	Wetted Perimeter [mm]	D _h [mm]	Heated to Wetted Perimeter Ratio
Sub-channel	15.18	17.99	3.375	100%
Periphery-channel	55.51	43.97	5.050	54.5%

To interface the test section geometry with the rest of the thermal-hydraulic loop, fluid is delivered from the loop through the inlet block, one of the common test section elements. The block, shown below in Figure 6-12, is designed to both turn the flow, which is delivered radially to the test section geometry, and distribute the flow evenly around the periphery of the test section geometry to prevent any of the heated elements from being starved of flow. To accomplish these tasks, the inlet block functions as both a stagnation chamber and volute for the 7-rod-bundle test section.

Flow enters through the bore in the top of the block into a cylindrical bore which acts as a stagnation chamber. Due to the geometry of the inlet bore intersecting with the cylindrical bore, the flow experiences a sudden expansion; the increasing flow area is used to slow the incoming fluid. For the 7-rod-bundle test section the heated rods pass through the back of the inlet block (Figure 6-12), which creates a flow blockage in the center of the cylindrical bore. The orientation of the heated rods to the inlet bore, shown below in Figure 6-13, results in two stagnation lines where the inlet flow is oriented normal to the top two heated rods, while the space between the heated rods will act as converging ducts pointed at the central heated rod. As the flow spreads around the stagnation lines, the red dots in Figure 6-13, the flow directed to the periphery will be directed around the rod bundle.

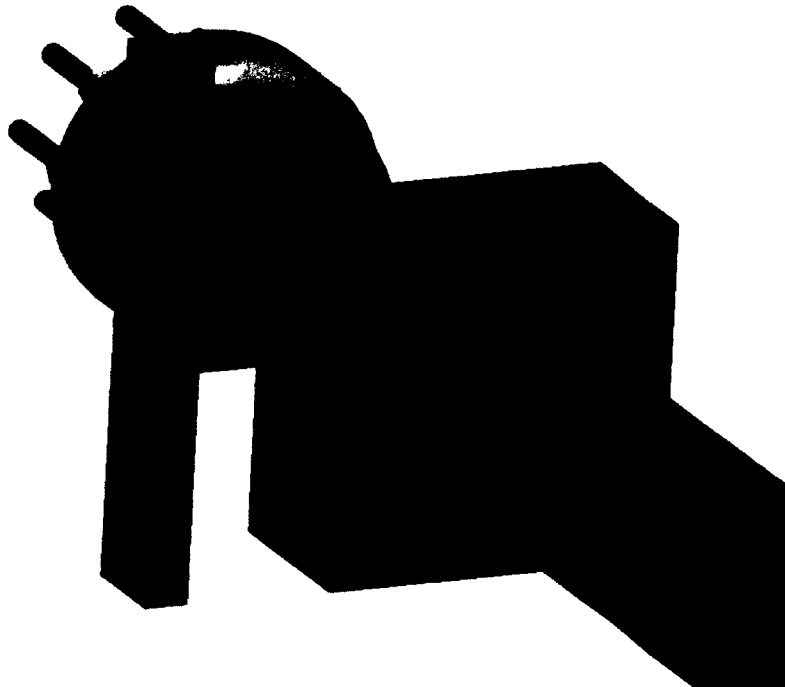


Figure 6-12: 7-Rod-Bundle Inlet/Outlet Assembly Exploded View

The flow area difference between the flow path around the rod bundle and the flow path between the heated rods will ensure that most of the fluid will be distributed around the

periphery as if a volute was present. The fluid that does not escape into the core will flow into the periphery-channels described above (Figure 6-11). The entrance to the shroud from the inlet block cylindrical bore is rounded to reduce entrance losses. The shroud face round has a 10 mm radius round which yields a loss coefficient of less than 0.05 for its diameter [22], and can therefore be considered lossless. The round does not extend completely to the periphery, leaving a thin, flat faced ring to mate with the shroud positioning face of the inlet block. This inlet configuration is expected to provide the necessary flow distribution without incurring excessive losses or requiring a complicated geometry.

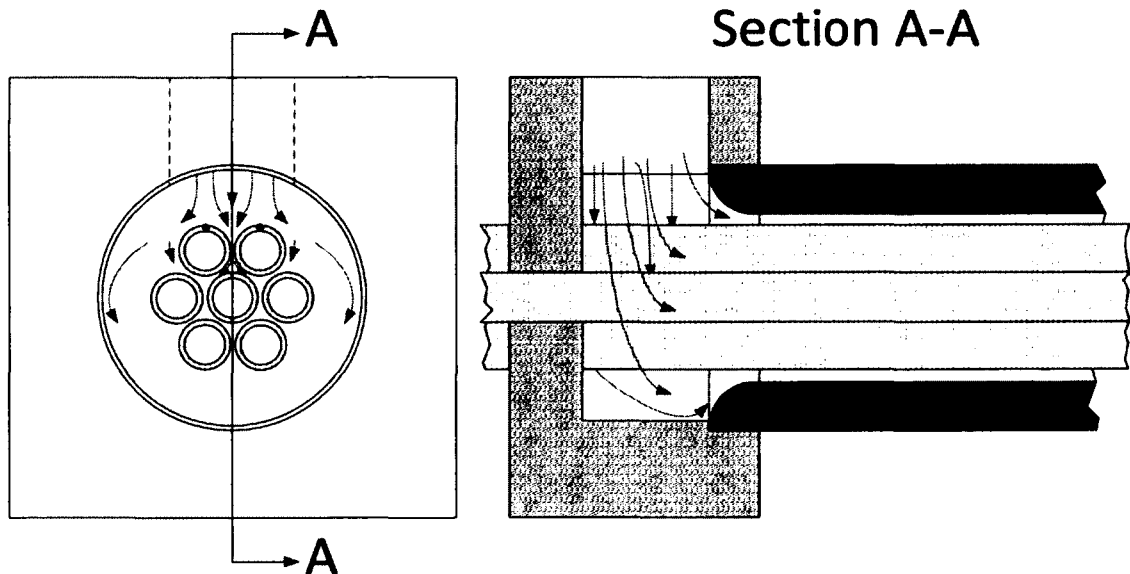


Figure 6-13: Inlet Cross Section and Flow Distribution Illustration, 7-Rod-Bundle Test section
 Per AECL's standard, each test section is expected to have an unheated entry length of 50 hydraulic diameters to allow the flow to come to a fully developed state [59]. While the true hydrodynamic entry length varies with geometry and geometry features as well as Reynolds number, the 50 length to diameter ratio was settled on to standardize tests and facilitate comparisons between different experimental setups. As the length of the test section is limited by the lab space, the unheated and heated length of the test section becomes a function of the

hydraulic diameter. For this reason, using 2" XXS piping for the shroud with its smaller hydraulic diameter (Table 6-4) has the additional benefit of maximizing the heated length in which experiments may be carried out. The resulting heated and unheated lengths for the chosen hydraulic diameters of the test sections are presented in Table 6-6.

Table 6-6: Test Section Heated and Unheated Lengths

Test section Length	2329 mm			
	D _h [mm]	Unheated Length [mm]	Heated Length [mm]	Heated Length Ratio
7-Rod-Bundle	4.56	228.0	2101.0	90%
Annular	3.76	188.0	2141.0	92%
Tubular	8.95	447.5	1881.5	81%

For the reasons listed above, an identical block is used to collect the flow from the exit of the shroud. The shroud exit face has the same round as the entry face; however this is for symmetry purposes only to ensure the test section is completely reversible. As described by White the exit shape has a negligible impact of the loss coefficient as the cylindrical bore is sufficiently large, so the loss coefficient becomes 1.0 [22]. After discharging into the outlet block's cylindrical bore, the fluid is collected and discharged through the outlet bore to the thermal-hydraulic loop.

6.2.3 Annular Test section

Maintaining the greatest possible number of common parts between test section designs, the same heated rod size used in the 7-rod-test section will be used as the inner tube of the annular test section. This will allow for the instrumentation developed for the 7-rod-bundle to be utilized with the annular test section as well. Comparing this to the initial specification and applying the same approach of selecting a NPS pipe to be the shroud yields the selection of a 1" XXS pipe, with the component geometry detailed in Table 6-7, Table 6-8, and Figure 6-14.

Table 6-7: Internal Component Geometry Comparison, Annular Test section

	Shroud ID [mm]	Heated Rod OD [mm]	D _h [mm]	Flow Area [mm ²]
Initial Specifications	16	10	6	123
Modified For Instrumentation	17.45	11.45	6	136
Modified with 1" XXS Shroud	15.21	11.45	3.76	78.8
Modified with 1½" XXS Shroud	22.75	11.45	11.3	304

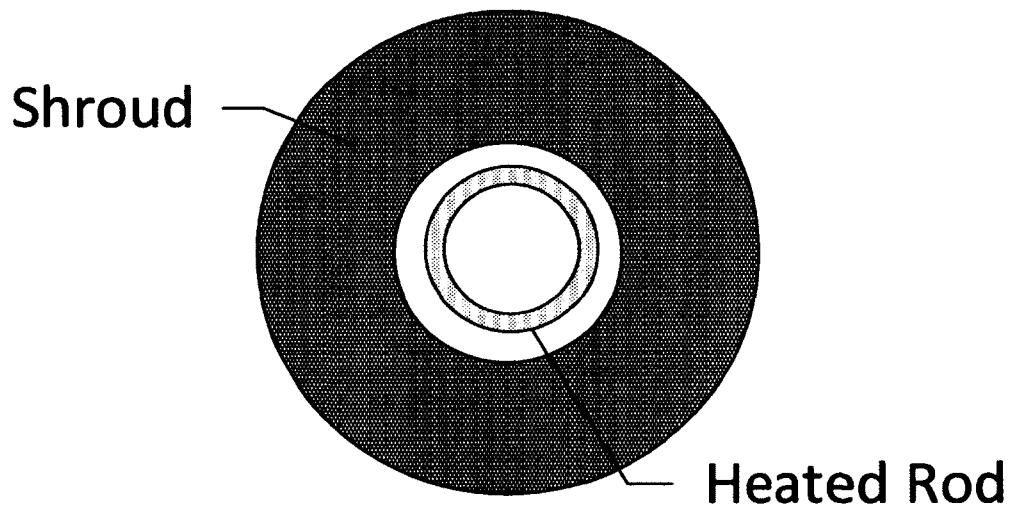


Figure 6-14: Annular Test section Cross Section

Table 6-8: Annular Test section Geometry

	Outer Diameter [mm]	Inner Diameter [mm]
Shroud	33.40	15.21
Heated Rod	11.45	8.95

To accept the annular test section, the inlet/outlet block design is modified from the 7-rod-bundle geometry as outlined in Table 6-3. Since the number of heated rods is reduced from seven to one from the bundle to the annular configuration, the heated-rod pass-through cut-out's pattern is modified to match; the center hole remaining while the six periphery holes are eliminated. The front face bore is scaled down to match the outer diameter of the 1" XXS piping.

The face bore being of lesser diameter than the cylindrical bore requires the face bore depth to be reduced to 9 mm to provide a mating ring to seat the shroud against. The geometry described in Table 6-3 is shown in Figure 6-15 with the resulting cross section.

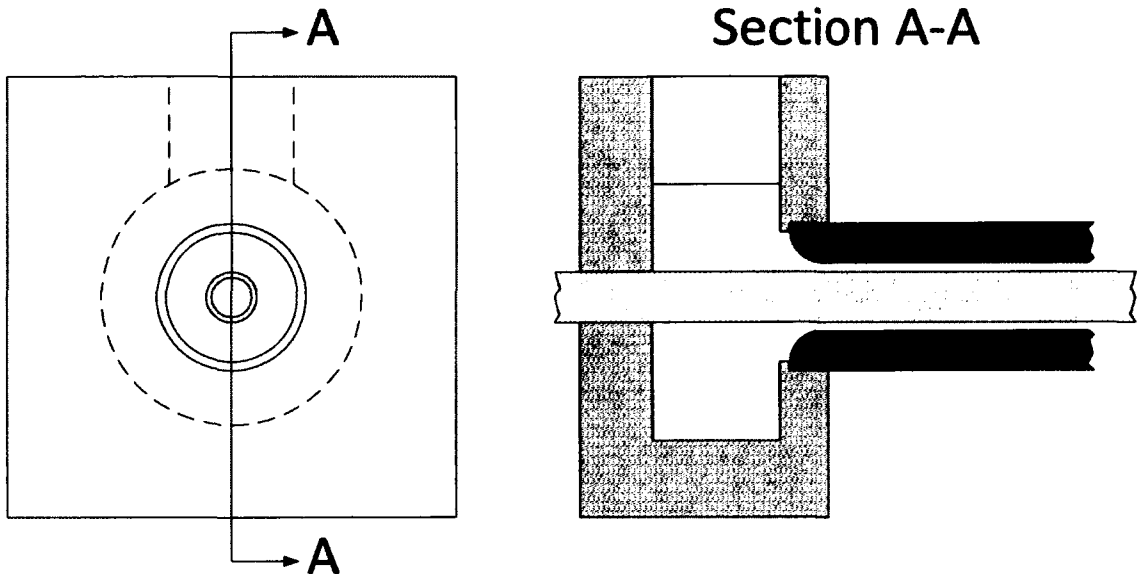


Figure 6-15: Inlet Cross Section, Annular Test section

No special consideration is required to turn and distribute the flow from the inlet to the shroud entrance with the annular test section. Between the sudden expansion loss effects and the flow area expansion, more than doubled from inlet to heated rod, the flow will slow down substantially before being drawn into the test section. The entrance to the shroud is rounded (7 mm round) as was done for the 7-rod-bundle shroud to reduce entrance losses, with the same effect. Shown above in Table 6-7, based on the test section's hydraulic diameter the unheated entry length takes up 8% of the total test section length. After the heated length the fluid is discharged into the outlet block, of the same design as the inlet block, where it is collected and discharged to the loop through the exit bore.

6.2.4 Tubular Test section

The tubular test section differs significantly from the 7-rod-bundle and annular test sections, as the power and flow delivery are greatly simplified in comparison. The tubular test section's shroud is derived from the heated rods used in the other test sections above, this reduces the number of unique parts to manufacture and certify. To preserve continuity between test sections interconnects, a similar inlet/outlet block is employed as in the annular and 7-rod-bundle test sections. However, without the need to pass a heated rod through the back of the block and the flow disruption it produces, the cylindrical bore is removed and a T-joint style connection is used between the test section and inlet bore. The inlet bore is also continued past the test section joint to the same depth as the diameter of the cylindrical bore would reach. This provides consistency for the through port to the pressure sense line as well as a zone away from the test section inlet for the recirculation effects due to dead-heading the inlet bore. The resultant cross section is shown below in Figure 6-16.

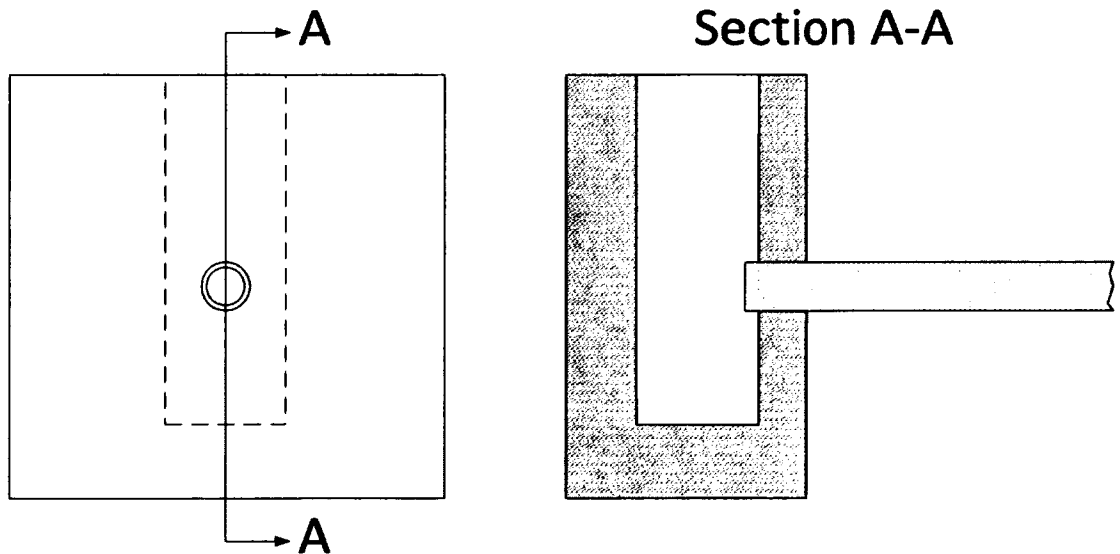


Figure 6-16: Inlet Cross Section, Tubular Test section

The small internal diameter of the tubular test section with the configuration resulting in branch flow between the inlet/outlet bore and test section would result in higher than necessary entry/exit losses; to reduce the losses, a reentrant inlet is used [22]. The reentrant inlet's specifications are provided in Table 6-9 below, and should reduce the inlet losses to an acceptable level. Shown above in Table 6-6, based on the test section's hydraulic diameter the unheated entry length takes up 19% of the total test section length. The exit of the test section has the same reentrant design to discharge the flow to the outlet bore, which as discussed previously will not reduce exit losses, however is implemented to preserve reversibility of the test section.

Table 6-9: Tubular Test section Reentrant Inlet/Outlet Geometry [22]

Shroud	D	t	$l_{\text{projection}}$	t/D	l/D	K_{loss} Estimate
[mm]	8.95	1.25	3.00	0.14	0.33	0.65

6.3 Electric Resistive Heating

To simulate the thermal release of a nuclear decay process, the test sections use electric resistive heating (Joule heating). This method is standard across similar experimental setups, as discussed in Chapter 1 and other thermal-hydraulic loops, and provides a well-defined and easily measurable source of heat for the experiments. The electric heating chosen is direct current, which provides a low noise constant power source that produces superior uniform heat flux across the conductor compared to alternating current. Since direct current is being used, the power delivered to the test section can be taken directly from Ohm's law and the definition of electric power dissipation (Eqn. 6.1, 6.2).

$$V = IR \tag{6.1}$$

$$P = VI \tag{6.2}$$

where: V : voltage; I : current; R : resistance; P : power.

The test sections will be supplied power from a 300 kW DC power supply (DTLG 600-150/2000) from Magnavolt. The power supply is rated for operation of 0-150 Vdc and 0-2000Adc, which requires that the test section's resistance to be exactly matched to the power supply's specifications (0.075 Ω) to utilize all the power available for heating.

6.3.1 Power Dissipation

Electric power is dissipated to heat through the process of Joule heating, where a materials resistance to the passage of an electric current converts some of the electric potential to heat which is released inside the material; if the material is homogenous, this process is evenly distributed throughout the volume. The materials resistance to the flow of electric current is known as its electrical resistivity, which in conjunction with the materials geometry yields the total resistance (Eqn. 6.3).

$$R = \frac{\rho l}{A} \quad (6.3)$$

where: R : resistance; ρ : resistivity; l : conduction path length; A : conduction path cross section area.

The total resistance of a system is determined by the sum of the contributions of individual resistances. Resistive elements in parallel offer a larger total flow path, and so contribute as their reciprocals, while elements in series are cumulative and summed as such. The total effective resistance for elements in series or parallel is shown in Equations 6.4.a and 6.4.b. Using Equations 6.3 and 6.4 along with the geometry of the test sections, the effective resistance of each test section may be calculated.

$$R_{tot} = \sum R_i \quad \text{Resistance in Series} \quad (6.4.a)$$

$$R_{tot} = \left(\sum \frac{1}{R_i} \right)^{-1} \quad \text{Resistance in Parallel} \quad (6.4.b)$$

Using the heated rods, as the heating element for either the 7-rod-bundle or the annular test section, results in a poorly matched resistance for the power supply and limits the potential power delivered to the test sections. Due to the 7 heated rods arranged in parallel the resistance of the 7-rod-bundle is much lower than the desired 0.075 Ω , so the test section would be current limited by the power supply. The annular test section is nearly perfectly matched to the power supply, so is sufficient without modification to deliver nearly 300 kW to the test section. While the tubular test section's shroud has the same geometry as the other test section's heated rods, and therefore resistance characteristics similar to the annular test section, the total heated length is significantly less, reducing the total resistance. This results in a reduction in the total power that can be delivered. With the goal of studying fundamental heat transfer characteristics in supercritical fluid, the tubular test section will be able to perform adequately with the power delivered and so requires no modification. The basic resistance and power delivery characteristics of the test sections are shown in Table 6-10.

Table 6-10: Basic Test section Power Characteristics IN625

	7-Rod-Bundle	Annular	Tubular
A_c [mm²]	280.4	40.05	40.05
Heated Length [mm]	2101.0	2141.0	1881.5
Average Resistivity [$\mu\Omega$-m]	1.36	1.36	1.36
Element Resistance [Ω]	0.071	0.073	0.064
Total Resistance [Ω]	0.010	0.073	0.064
Max Voltage Drop [V]	20	146	128
Max Current [A]	2000	2000	2000
Max Power Delivered [kW]	40	292	256

To deliver an appropriate amount of power to the 7-rod-bundle test section, the power must be dissipated through a heating element different than the heated rods themselves. To achieve this, the rods are to be coated with ceramic material to act as the heating element. As the

coatings thickness may be specified independently, the new heating element's resistance may be specified without modifying the heated rods which are required to act as pressure vessels.

Geometries of all electric power components will be detailed below in Section 6.3.4, including the unheated length and electrical bussing. The final power dissipation characteristics of each test section will be presented there for convenience.

6.3.2 Convective Heat Transfer Coefficient and Heating Element Temperature

While the purpose of the test sections is to study the heat transfer between the heated rods and the fluid, a preliminary estimate of the heat transfer effect is necessary for establishing the maximum expected temperature of the heated rods to ensure they meet the ASME standards and will not fail in operation. From the theory discussed in Appendix A, the volumetric Joule heating and subsequent heat dispersion can be used to derive a temperature field across the heated rod. The transient thermal simulations performed on the thermal-hydraulic loop (see Chapter 4) made the assumption that all the heat generated by the resistive heating is transferred to the fluid. This is the worst case scenario for the heated rods as it assumes that their internal surface is adiabatic and therefore, at steady state conditions, the heated rods will reach the same temperature as the heating element. This approximation is useful as it sets the upper temperature limit the heated rods may experience in service, and can therefore be used for the design requirements. In the case of the tubular test section which uses the shroud as the resistive heating element, the outer surface is insulated, which also satisfies the adiabatic assumption, and so the analysis used for the 7-rod-bundle and annular test sections can be extended to the tubular test section.

The validity of this approach is limited to the accuracy of the empirical correlation between known quantities, such as the fluid's Reynolds number and Prandlt number, and the heat

transfer coefficient, expressed through the Nusselt number. Previous experimental work suggests that while the correlations, which are well developed for subcritical flow, follow the correct trend, they are only accurate to within 25% [25][70][71]. Different correlations for the Nusselt number have been proposed, but remain limited to the experimental setup from which they were determined, as they have not been tested extensively across different flow configurations[70][71]. Further complication exists for the 7-rod-bundle test section which will see a non-uniform heating of the flow, as the reduced core flow will result in stronger heating of the core fluid compared to the periphery fluid. This behaviour is seen in the experimental work and numerical simulations carried out on rod bundle configurations [71][72][73]. With these limitations in mind, the analysis can be used to provide a first order estimate of the temperature distribution.

Since the heating elements are considered to be homogenous and the resistivity either constant, or the heating element designed to deliver uniform heating along the length of the test section, constant heat flux will be assumed over the heated length of the test section. Using the temperature and convective heat transfer coefficient profile along the length of the test section from the simulation, a surface temperature profile may be developed using Equation 6.5.

$$\dot{q}''_{conv} = h_{conv}(T_s - T_{\infty}) \quad (6.5)$$

where: \dot{q}'' : heat flux; h_{conv} : convective heat transfer coefficient; T : temperature.

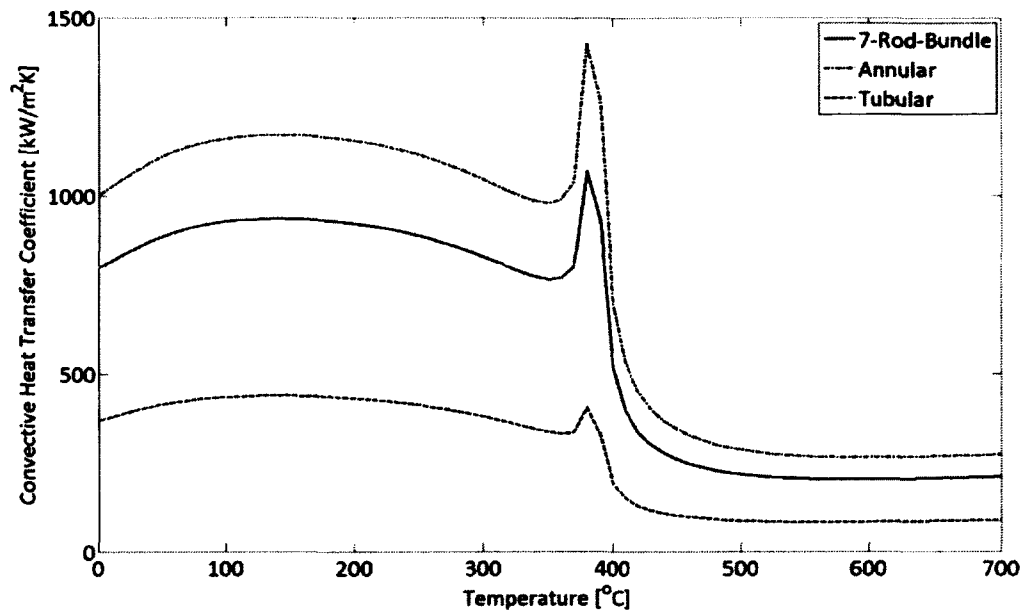


Figure 6-17: Convective Heat Transfer Coefficient versus Temperature for the Test sections with a Mass Flow Rate of 0.125 kg/s

Table 6-11: Test section Heat Flux and Peak Heating Element Surface Temperature

Test section	7-Rod-Bundle	Annular	Tubular
Maximum Power Delivered	300	300	256
Heat Transfer Area [m ²]	0.529	0.077	0.053
Heat Flux [kW/m ²]	567	3900	3970
Mass Flow Rate [kg/s]	0.127	0.127	0.108
Peak Surface Temperature [°C]	616	680	1137

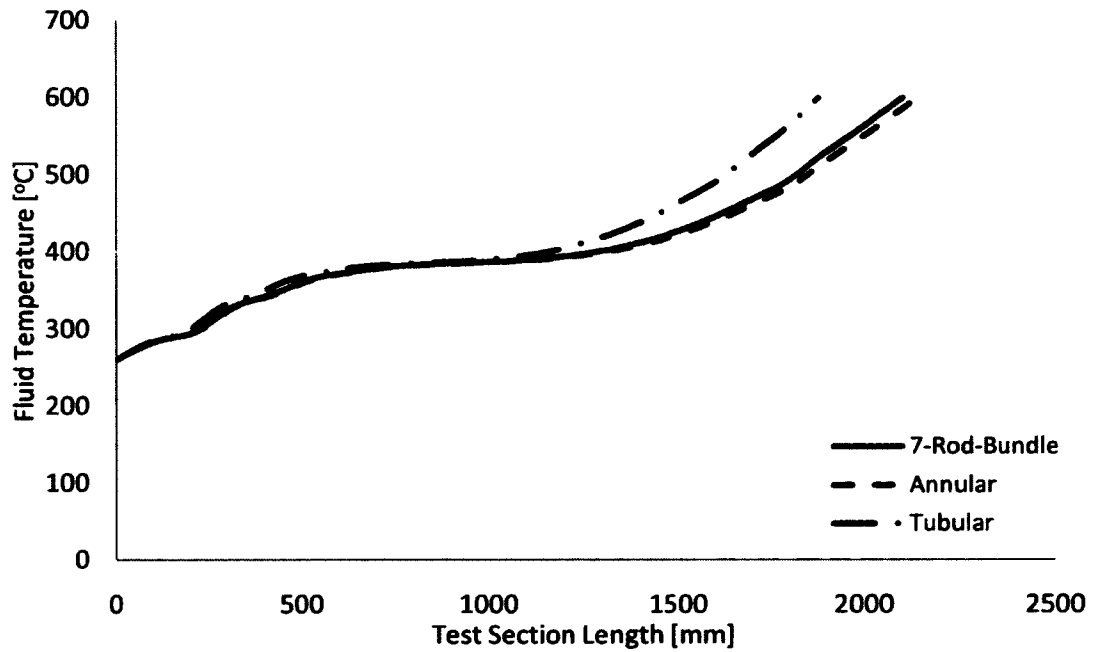


Figure 6-18: Steady State Fluid Temperature Profile in the Test section

The predicted fluid temperature profiles used for each test section are shown in Figure 6-18, while a representative convective heat transfer coefficient versus temperature profile is shown in Figure 6-17 above. Given the power delivered to each test section, to reach a bulk fluid temperature of 600 °C at the end of the heated test section, the mass flow rate of each test section must be matched to the available heat input, with the corresponding values given in Table 6-11.

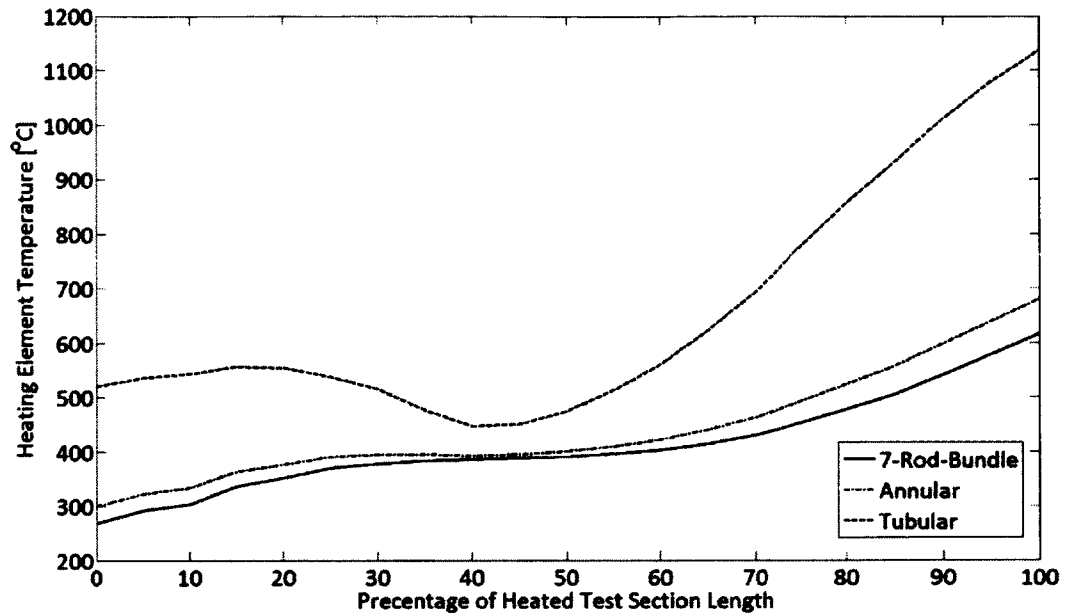


Figure 6-19: Heating Element Temperature versus Test section Length at Maximum Heat Flux

Using the constant heat flux assumption and the fluid temperature profiles from Figure 6-18 Fourier's law of heat transfer (Eqn. 2.2) may be solved to yield the heating surface interface temperature between the heating element and the fluid. Since the heating element is thin (micron scale) the temperature across it may be assumed to be constant, so the surface temperature may be taken as the bulk temperature. The resultant heating element temperature profiles for each test section are shown in Figure 6-19. Both the 7-rod-bundle and annular test sections have sufficient heat transfer surface areas coupled with a low hydraulic diameter (increasing the Reynolds Number and therefore heat transfer coefficient) that the heating element temperature tracks the fluid temperature at a slightly higher temperature. The tubular test section has the greatest specific heat flux and the largest hydraulic diameter which requires greater heat transfer in a less efficient system. To drive this heat transfer, the temperature of the heating element must be much higher than the fluid. This temperature difference ranges from 250 °C up to nearly 600 °C at the test section outlet, except where the fluid passes through the pseudo-critical point. Around the critical point, the fluid's specific heat capacity

asymptotically approaches positive infinity, similar to the thermal conductivity shown in Appendix A. With both the fluid's specific heat capacity and thermal conductivity tending to infinity at the pseudo-critical point the fluid effectively loses all thermal resistance and heat transfer becomes nearly unlimited. This is expressed in Figure 6-20 where the heating element temperature of the tubular test section drops to be nearly equal to the fluid temperature before sharply rising as the fluid continues to heat and moves away from the pseudo-critical point and the heat transfer capacity of the fluid deteriorates. The impact of the very high peak temperature of the tubular test section heating element will be discussed in detail further in Section 6.4.

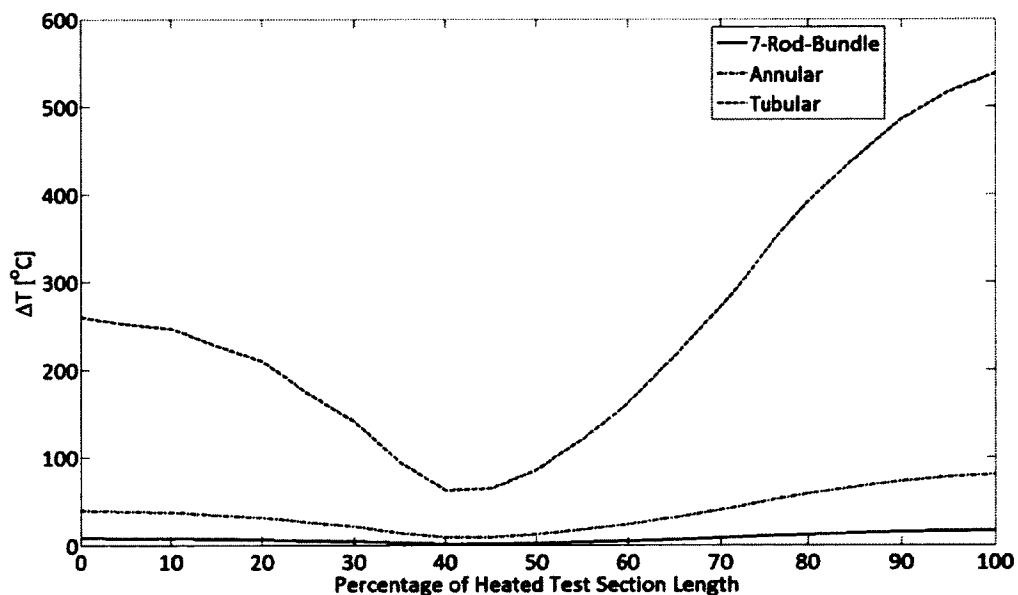


Figure 6-20: Heating Element to Fluid Temperature Difference versus Test section Length at Maximum Heat Flux

Figure 6-21 and Figure 6-22 below show the convective heat transfer coefficient as a function of test section length and heating element temperature. The effects of the fluid near the pseudo-critical point are highlighted by Figure 6-22 for tubular test section. As the fluid approaches the pseudo-critical point, the improved heat transfer reduces the heating element temperature

significantly, as shown by the plot folding back on itself. Once the fluid has passed the pseudo-critical point the heat transfer coefficient drops and the heating element temperature climbs rapidly. Since increasing the fluid's pressure increases the temperature at which the pseudo-critical point occurs, this has a significant implication for the effect of pressure drop through a test section, or operating fuel bundle, on safety; controlling what temperature the pseudo-critical point will occur at can determine the peak temperature during a heat transfer process. This will be studied in detail during the experiments carried out by the supercritical thermo hydraulics group at Carleton University.

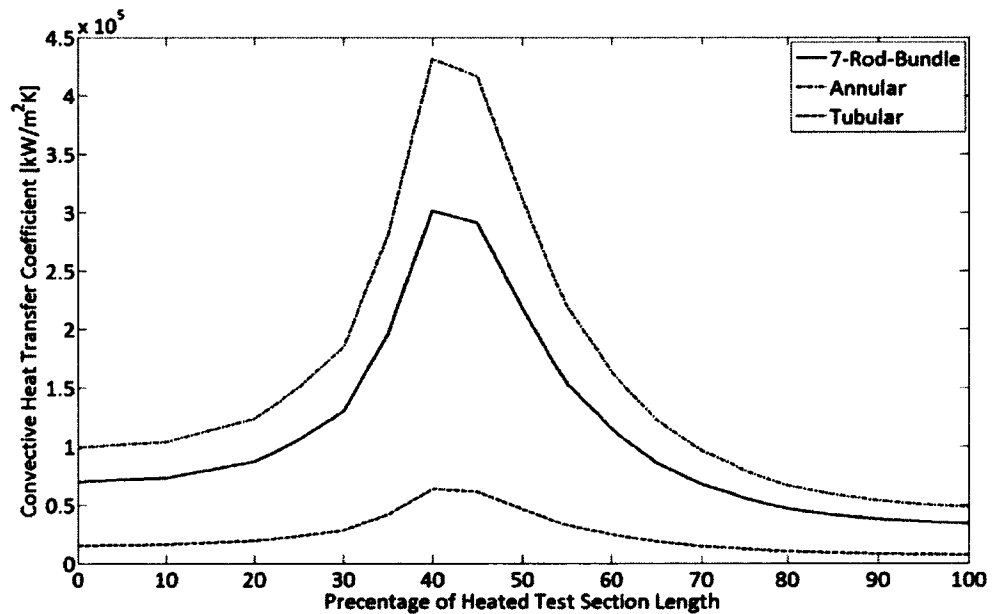


Figure 6-21: Heat Transfer Coefficient versus Test section Length at Maximum Heat Flux

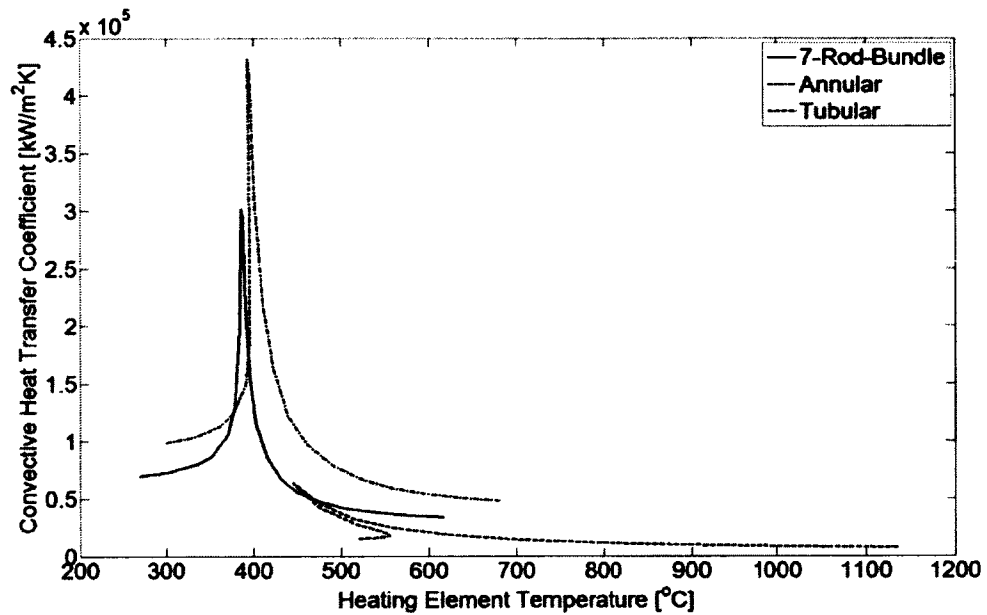


Figure 6-22: Heat Transfer Coefficient versus Heating Element Temperature at Maximum Heat Flux

The relatively low-gradient heating element temperature profiles of the 7-rod-bundle and annular test sections coupled with their thin cross sections will result in negligible heat flow axially along the heating element. The absence of axial conduction through the heating element(s) of these test sections will allow for the uniform heat flux assumption to hold true, and lends a high degree of confidence to the estimated temperature profiles. For the tubular test section, the local minimum in the temperature profile, coupled to the larger temperature gradients along the heating element will result in a sink effect where the fluid reaches the pseudo-critical point. This sink effect not only removes the uniform heat flux assumption from the tubular test section, but will likely result in an instability in the fluid heating as the minimum heating-element-temperature location fluctuates in the axial direction. A more refined analysis detailing this unsteady behaviour will have to be carried out on the tubular test section, or a greater safety margin will have to be built into its design.

6.3.4 Power Delivery and Electric Insulation

Power will be delivered to the test sections through a copper bus connected to the power supply by an appropriate cabling run. The design of the cabling run from the power supply lies outside of the scope of this work, as it is part of the thermal-hydraulic loop and lab design; however it is assumed to be well designed with negligible power losses and interface to the test section through a Cam-Lok type connector [74][63]. This will allow for a simple and safe connection point that uses standard AWG cables and is CSA certified. The female connector is pictured below (Figure 6-23) which bolts onto the test sections electric bus. Each connector is rated for 600 V and up to 690 A continuous (1150 intermittent); each bus accepting a minimum of three connectors for a total delivery rating of 2070 A.



Figure 6-23: Cam-Lok E1017 Series Female Receptacles [74]

The 7-rod-bundle and annular test sections use a common copper bus design to deliver power to the heated rods (Figure 6-24 and Figure 6-25). As the pressure vessel must be penetrated to deliver the power to the heating elements a flange arrangement is used to seal the heated rod

pass through, with the electric bus doubling as the gasket material. This will be detailed below in Section 6.4.3. The main bus bar holding the three Cam-Lok female connectors will be considered to exist at a constant and uniform potential with voltage drop first occurring along the two delivery rails which penetrate the flange cap (described later). Due to the greatly increased cross sectional area and very short conduction path to the heated rods, the copper gasket plate interfacing the heated rods to the delivery rails will also be considered at uniform potential without voltage drop. The current is then transferred to the heated rods and through the unheated section of the test section to the heated section. After the heated section the current leaves the test section through an identical copper bus as found at the delivery end. This ensures reversibility for the test section.

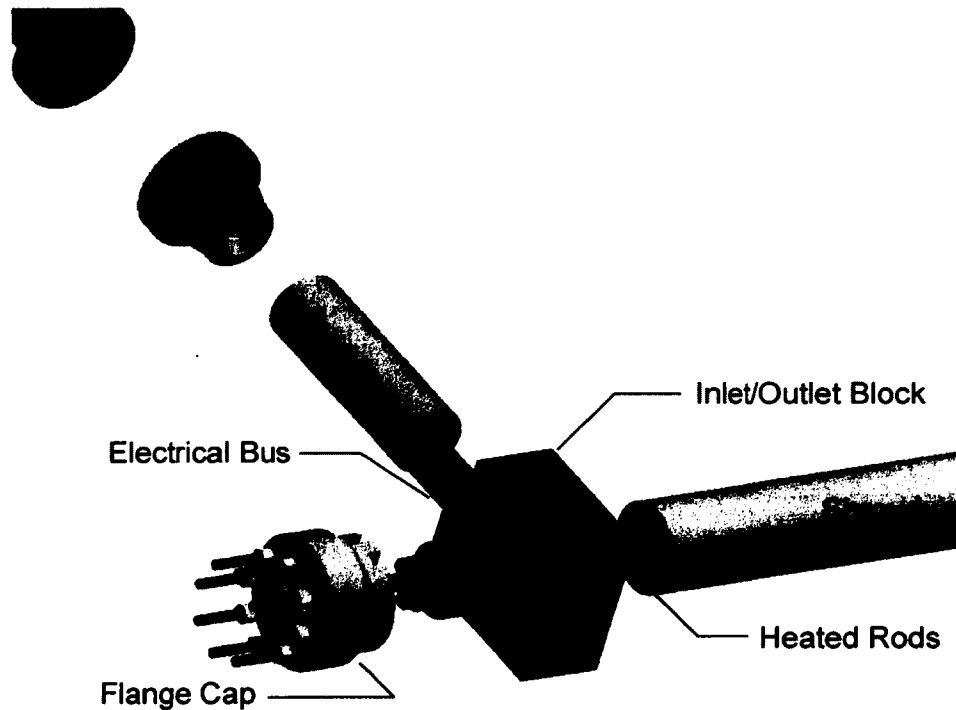


Figure 6-24: Electrical Bus and Test section Assembly

Previously discussed in Section 6.3.1 the 7-rod-bundle test section requires modification to the heated rods in the form of a separate heating element designed to match the desired resistance

based on the power supply unit. This heating element must be electrically insulated from the heated rods to ensure proper operation; this requires the heated rods to be fully electrically insulated from power delivery to removal. Based on the material selection investigation in Chapter 5, alumina is an excellent choice as it has good adhesion to super alloys with their base aluminum content and excellent mechanical and corrosion properties. As a dielectric it is more than adequate given the low voltage delivered by the power supply, requiring a coating of less than 20 μm to provide electric insulation. A 20 μm coating is also applied to any metallic face that will make contact with a conducting element, including the inner face of the flange cap and the rear face of the inlet/outlet block. With the base coating applied to provide electric insulation of the heated rods, two additional layers are required to provide the desired electrical behaviour as well as an additional electrical insulation and corrosion resistance layer. A schematic of the coating sandwich for the heated rods in the 7-rod-bundle test section is shown below in Figure 6-25.

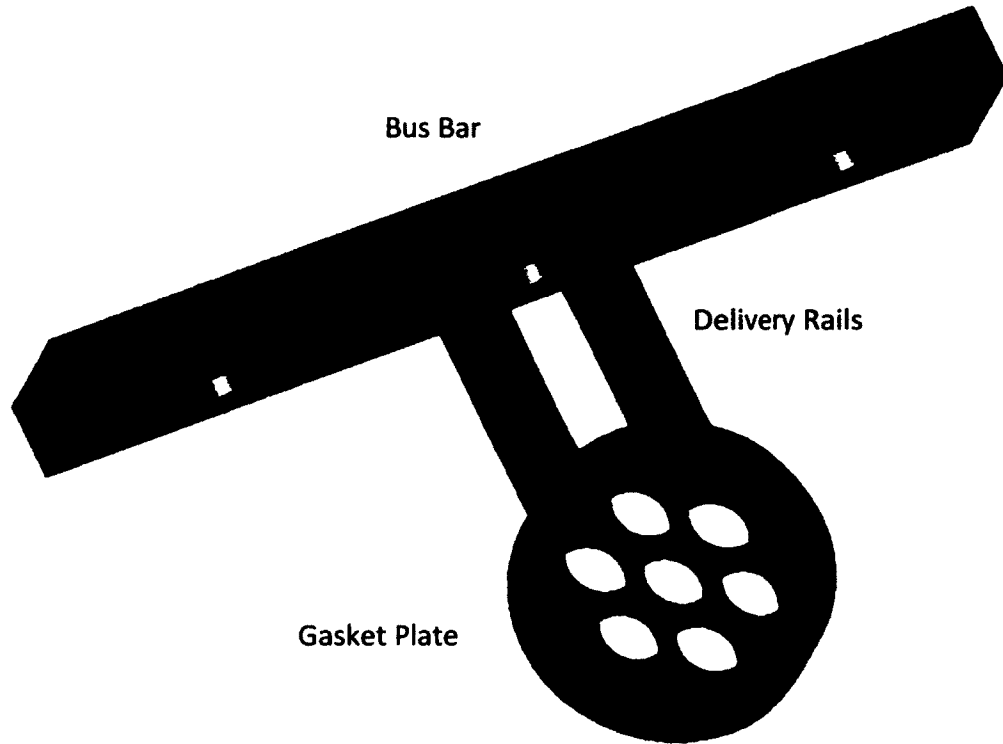


Figure 6-25: 7-Rod-Bundle Copper Bus and Gasket

To contain the power dissipation to the heated portion of the test section as much as is possible, the coating sandwich consists of two distinct types, one using a conductor and the other the Kanthal heating element, titled unheated length and heated length respectively. Matching the Kanthal's resistivity as a function of temperature to the heating element temperature from Figure 6-19 allows the desired thickness of the heating element along the length of the heated section to be determined through Equation 6.1.

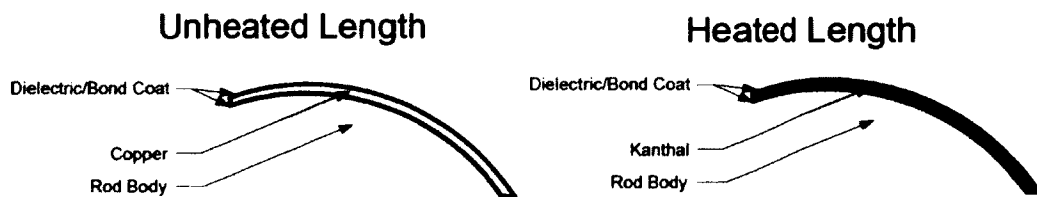


Figure 6-26: 7-Rod-Bundle Coating Schematic

To provide uniform heat flux along the length of the heated section of the 7-rod-bundle test section, the resistor's cross sectional area is varied along the heated rod's length (Eqn. 6.1). The necessary coating thicknesses are summarized in Table 6-12 and Figure 6-27. Using the area profile from Equation 6.1 the required Kanthal thickness may be computed since the inner diameter is fixed at 11.49 mm. The area and thickness profiles are plotted below in Figure 6-27.

$$\frac{R_l}{l} = \frac{\rho}{A} \quad (6.1)$$

Table 6-12: 7-Rod-Bundle Coatings

Coating	Start [mm]	End [mm]	Thickness [μm]
Dielectric Rod Insulation	0	2539	20
Inlet to Heated Section Copper	40	333	130
Kanthal Heating Element	333	2434	Variable
Heated Section to Outlet Copper	2434	2499	130
Dielectric and Corrosion Coating	50	2489	20

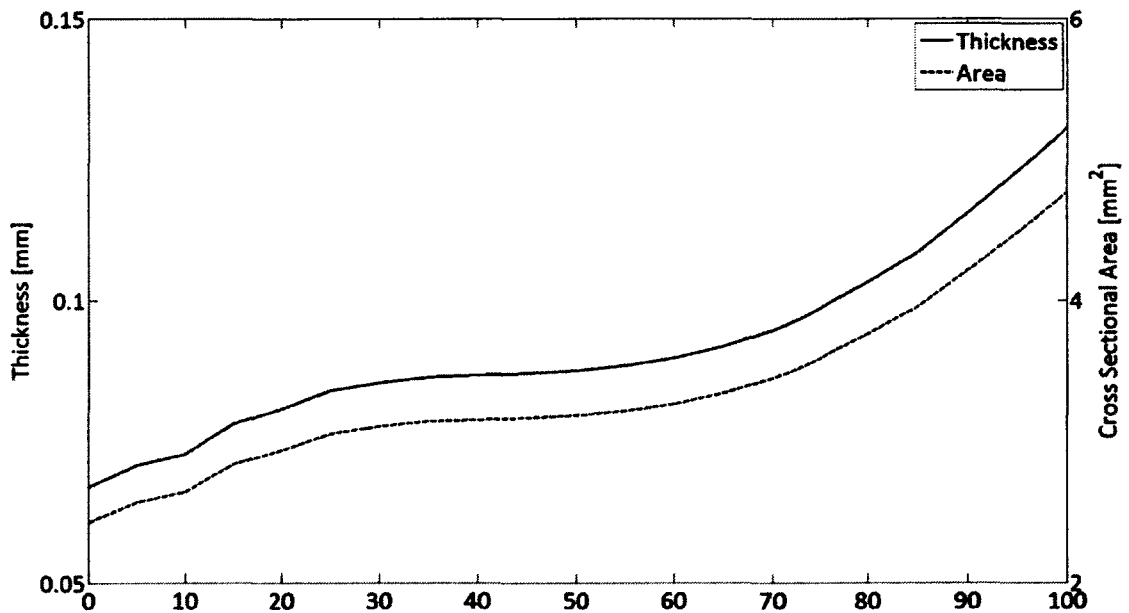


Figure 6-27: Kanthal Thickness and Area Profile versus Heated Test section Length

For the unheated lengths, the resistance is to be minimized to reduce power dissipation and minimize losses through the inlet and outlet electrical buses. The largest Kanthal thickness is

used for the copper conductor coating to minimize the resistance without further reducing the spacing between heated rods. As shown below, the total power dissipated in the unheated sections is negligible compared to that dissipated in the heated section; therefore, the temperature of the copper conductor may be considered constant at 260 °C at the inlet, matching the fluid temperature, and 600 °C at the outlet also matching the fluid temperature. The electrical properties of the unheated sections and the resultant total resistances are given in Table 6-13.

Table 6-13: Copper Components Electrical Properties, 7-Rod-Bundle Test section [64]

		T [°C]	A_c [m ²]	L [mm]	Resistivity [nΩ·m]	R_{total} [μΩ]
Inlet Delivery Rail		260	87.0×10^{-6}	55	31.32	19.80
Unheated Section	Inlet	260	4.7674×10^{-6}	288	31.32	1892
	Outlet	600	4.7674×10^{-6}	60	51.70	650.7
Outlet Delivery Rail		600	87.0×10^{-6}	55	51.70	32.68

Summing the individual contributions of all the resistive elements yields the total effective resistance of the 7-rod-bundle test section, matched to the power supply unit to draw the full 300 kW of power (Table 6-14). By using a custom coating for the heated and unheated sections, not only is the power delivered to the heated test section maximized, but the power system is made very efficient with 99.46% of the power being delivered to the heated portion of the test section. The copper and Kanthal coatings are insulated with an additional alumina coating to prevent arcing or conduction to the surrounding metallic components. The alumina also provides corrosion resistance necessary to prevent attack from the supercritical water.

Table 6-14: Test section Electrical Resistance, 7-Rod-Bundle Test section

		$R_{\text{component}} [\Omega]$	$R_{\text{reflective}} [\Omega]$	Power Dissipated [kW]
Delivery Rails @ 260 °C			9.900×10^{-6}	3.96×10^{-2}
	Individual Rail	19.80×10^{-6}		
Heated Rod Bundle			0.07497	299.88
	Unheated @ 260 °C	1892×10^{-6}		
	Heated	0.5222	0.5222	298.4
	Unheated @ 600 °C	650.7×10^{-6}		
	Heated Rod		0.5248	
Delivery Rails @ 600 °C			16.34×10^{-6}	6.54×10^{-2}
	Individual Rail	32.68×10^{-6}		
7-Rod-Bundle Test section				300

The total added thickness increases the outer diameter of the heated rods to a maximum of 11.79 mm. To accommodate the increased diameter the rod spacing from the wall is reduced to maintain the sub channel spacing (Figure 6-11). The resultant geometry is presented below in Table 6-15.

Table 6-15: Test section Geometry Modified for Coatings, 7-Rod-Bundle Test section

	Outer Diameter [mm]		Inner Diameter [mm]	
Shroud	60.33		38.18	
Heated Rod	11.79		8.95	
D_h [mm]	4.02			
Radial Pitch	12.75			
Diametric Pitch	6.68			
	Flow Area [mm ²]	Wetted Perimeter [mm]	D_h [mm]	Spacing δ
Sub-channel	15.78	18.52	3.41	0.9575
Periphery-channel	47.67	44.68	4.27	0.4475

Since the resistance of the heated rod along the heated section of the annular test section is well matched to the power supply already, no additional modification is required for power delivery in the heated section. To reduce losses in the unheated sections, the resistance of the conduction path should be reduced. As the heated rod will be electrically charged, there is no

need to isolate it from the applied coating using an alumina substrate. The heated rod should not be made of any type of steel as in the event of the copper liquefying, it would embrittle the steel and potentially lead to catastrophic failure of the heated rod. This allows the copper to be applied to the inside of the heated rod, as it does not need to be directly exposed to the copper bus. The total thickness of the copper coating will not adversely affect the operation of the internal instrumentation (thermocouple probe) since the coating will not close the unheated inlet end and adequate space will remain to pass the instrumentation control mechanism though. The copper coating (0.5 mm thickness) details and the resultant electrical properties of the annular test section are presented in Table 6-16 and Table 6-17 below. A reduced thickness coating (0.1 mm) will be used at the outlet unheated section to allow the insertion of the instrumentation. The power loss penalty is acceptable since the outlet unheated length is sufficiently short. The exterior of the heated rod will be coated with 20 μm of alumina to prevent any electrical arcing as well as provide corrosion resistance for the heated rod.

Table 6-16: Copper Components Electrical Properties, Annular Test section [64]

		T [°C]	A_c [m ²]	L [mm]	Resistivity [n Ω ·m]	R_{total} [$\mu\Omega$]
Inlet Delivery Rail		260	87.0×10^{-6}	55	31.32	19.80
Unheated Section	Inlet Cu	260	13.27×10^{-6}	288	31.32	679.7
	Inlet Rod	260	40.05×10^{-6}	288	1345	9672
	Outlet Cu	600	4.7674×10^{-6}	60	51.70	650.7
	Outlet Rod	600	40.05×10^{-6}	60	1380	2067
Outlet Delivery Rail		600	87.0×10^{-6}	55	51.70	32.68

Table 6-17: Test section Electrical Resistance, 7-Rod-Bundle Test section

		$R_{\text{component}} [\Omega]$	$R_{\text{effective}} [\Omega]$	Power Dissipated [kW]
Delivery Rails @ 260 °C			9.900×10^{-6}	3.96×10^{-2}
	Individual Rail	19.80×10^{-6}		
Heated Rod			0.0741	296.52
	Unheated Cu @ 260 °C	679.7×10^{-6}	635.1×10^{-6}	2.54
	Unheated Rod @ 260 °C	9672×10^{-6}		
	Heated	0.073	0.073	292.00
	Unheated Cu @ 600 °C	650.7×10^{-6}	494.9×10^{-6}	1.98
	Unheated Rod @ 600 °C	2067×10^{-6}		
Delivery Rails @ 600 °C			16.34×10^{-6}	6.54×10^{-2}
	Individual Rail	32.68×10^{-6}		
7-Rod-Bundle Test section				296.63

As the copper coatings only modify the internal diameter the only change to the geometry of the annular test section due to the electrical coatings will be a slight increase in the outer diameter of the heated rod to 11.49 mm and a slight reduction of the hydraulic diameter by one percent to 3.72 mm.



Figure 6-28: Tubular Test section with Electric Buses

The tubular test section, with its simplified geometry uses a different power delivery bus than the 7-rod-bundle and annular test sections. Since the shroud is to act as the heating element as well, there is no need to penetrate the pressure vessel to transmit power to the heating element. The power is instead delivered by copper bus blocks that are bolted directly to the

shroud, with the positive and negative terminal locations defining the heated length. The buses for the tubular test section consist of two matched halves, shown below in Figure 6-29, that are bolted to heated shroud using the same bolts used to mount the Cam-Lok connectors. This provides a potential for Cam-Lok connectors to deliver power, though only three will be needed to deliver the maximum possible current. The tubular test section will have the lowest power dissipation in its heated section, while the resistance per unit length for the tubular test section is the same as for the annular test section, as shown above in Table 6-6 and Table 6-9 the reduced heated length of the heated length of the tubular test section results in a lower total resistance. Without the need to apply any coatings, and given that the electrical buses are at uniform potential, the power dissipated by the tubular test section and its geometry remains the same as given in the previous sections. If desired, since the electrical buses are not fixed, the heated length may be increased by moving the buses to increase the power dissipated at the cost of the unheated inlet section.

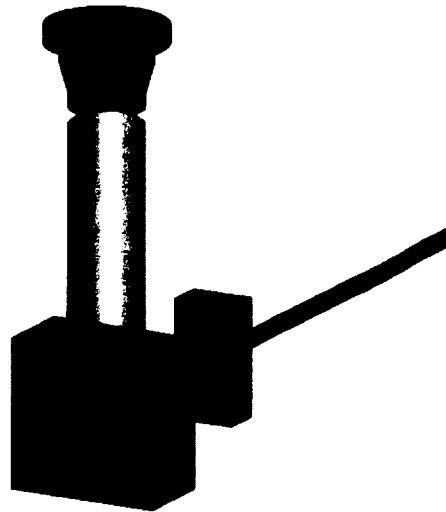


Figure 6-29: Tubular Test section Electrical Bus Assembly

6.4 Safety Analysis and Certification

To ensure safe operation of the test section and meet certification requirements, the test section was designed to conform to ASME code (B31.1) for high pressure apparatus. Each component, beside the heated rods, are designed to withstand the same design pressure and temperature , 28.35 MPa and 625 °C respectively, as the other components in the thermal-hydraulic loop for supercritical water [5]. The heated rods will be required to operate at an elevated temperature compared to the other components, as they must withstand the maximum heating element temperature (Figure 6-19) imposed by the heat transfer requirements. Their design operating pressure will be the same as the other components.

For the 7-rod-bundle and annular test section the heated rods must penetrate the surrounding pressure vessel to accommodate the electric power delivery. To prevent unwanted leakage of the working fluid from the thermal-hydraulic loop a sealing method has to be implemented at the locations where the pressure vessel is penetrated. This seal must be able to perform at the maximum expected component temperature and pressure while meeting ASME code; for these reasons the seal will use the same design pressure and temperature as the thermal-hydraulic loops components.

6.4.1 ASME Boiler, Pressure Vessel, and Pressure Piping Code Standards

The inlet and outlet Grayloc hubs and 1.5" NPS XXS piping are common to the thermal-hydraulic loop and satisfy the ASME piping code as detailed in the work by Masih et al [5]. The calculations will not be repeated in this report. The inlet/outlet blocks of the 7-rod-bundle and annular test sections may be treated as a straight pipe, due to the nature of the cylindrical bore, with multiple branch connections. Per section 104 of ASME B31.1 the basic minimum wall thickness of a straight pipe under internal pressure may be applied to determine the minimum wall

thickness before penetrations are made [49]. Knowing the internal diameter of the bore, Equation 6.6 may be used with the appropriate allowable stress value (S) for a material.

$$t_m = \frac{pD_i}{2(SE+py-p)} \quad (6.6)$$

where: t_m : minimum thickness; p : pressure; D_i : internal diameter; S : allowable stress; E : efficiency factor; y : empirical factor.

The weld joints of the various test section components are to be fully radiographed, so the type of butt weld used does not impact the joint efficiency factor (E), which will always be 1.0 due to the inspection. A dimensionless factor y that is temperature dependant is used to differentiate between material classes and is repeated from the ASME code in Table 6-18 below for convenience. The minimum wall thickness values for stainless steel type 316 (SS316), Inconel 600 (IN600) and Inconel 625 (IN625) are given below in Table 6-19 for the thermal-hydraulic loop design pressure and temperature.

Table 6-18: "Values of y " [49]

Temperature [°C]	482 and Below	520	538	566	593	621	649	677 and Above
Ferritic Steels	0.4	0.5	0.7	0.7	0.7	0.7	0.7	0.7
Austenitic Steels	0.4	0.4	0.4	0.4	0.5	0.7	0.7	0.7
Nickel Alloys	0.4	0.4	0.4	0.4	0.4	0.4	0.5	0.7

Table 6-19: Minimum Wall Thickness of Inlet/Outlet Blocks, 7-Rod-Bundle and Annular Test section

Material	T_{design} [°C]	P_{design} [MPa]	y	S [MPa]	D_i [mm]	t_m [mm]
SS316	625	28.35	0.7	65.5	58.19	14.47
IN600	625	28.35	0.4	15.2	58.19	-
IN625	625	28.35	0.4	145	58.19	6.043

The minimum wall thickness of the cylindrical bore is 20.91 mm, which is sufficient to allow for the block to be made of either SS316 or IN625. The design must also conform to section 104.3.1 Branch Connections, due to the penetrations to allow for the inlet/outlet piping and shroud to

be mounted to the block, along with the heated rod pass through(s) and pressure port in the outlet block. Per section 104.4 the requirements pertaining to straight pipes and branch connections also satisfy any closures or openings in a closure. Therefore the inlet bore, the face bore and a heated rod pass-through may be analyzed in the same manner. To satisfy the code's specifications, the loss in strength due to an opening in the pipe wall must be accounted for by a thickening of the surrounding joint equal in cross sectional area to the material removed, as defined in Equation 6.7 for a 90° branch.

$$A_{add} = t_m D_{opening} \quad (6.7)$$

where: A_{add} : cross sectional area of reinforcement required; t_m : minimum wall thickness; $D_{opening}$: diameter of opening through the pressure vessel.

The area available for reinforcement extends uniformly around the opening to a diameter of the greater of Equation 6.8, but not exceeding the external diameter of the header pipe, the cylindrical bore. Any additional thickness in the pipe wall that exceeds t_m for the pipe may be used to satisfy the additional area required along with any material added at the joint, in the form of weld material or strapping.

$$D_r = D_{opening} \quad (6.8.a)$$

$$D_r = t_{header} + t_{branch} + \frac{D_{opening}}{2} \quad (6.8.b)$$

The additional wall thickness of the inlet/outlet block design, compared to the minimum calculated thickness using IN625, satisfies the requirements for branch connections under ASME B31.1, without additional consideration of the welds or the mating components. To use SS316 for the inlet block would require additional thickening of the walls or the specification of sufficiently thick welds. The results for the 7-rod-bundle and annular test sections are summarized in Table 6-20 below.

Table 6-20: Branch Connections of Inlet/Outlet Blocks, 7-Rod-Bundle and Annular Test sections

Test section	Penetration	D _{opening} [mm]	D _r [mm]	SS316			IN625		
				A _{add} [mm ²]	t _{excess} [mm]	A _r [mm ²]	A _{add} [mm ²]	t _{excess} [mm]	A _r [mm ²]
7-Rod-Bundle	Inlet/Outlet Bore	27.94	27.94	404	6.44	180	169	14.87	415
	Face Bore	60.33	100	873	-0.73	-	364	7.93	793
	Heated Rod Pass Through	37.3	100	546	4.27	427	225	12.93	1293
Annular	Inlet/Outlet Bore	27.94	27.94	404	6.44	180	169	14.87	415
	Face Bore	42.16	100	610	-0.73	-	255	7.93	793
	Heated Rod Pass Through	11.45	100	166	4.27	427	69	12.93	1293

For the 7-rod-bundle heated-rod pass-through it is assumed that the material between each bore does not contribute to any load carrying capacity, so the opening is considered to be a circle lying tangent to the exterior surface of the six exterior heated rods. This is conservative but will ensure integrity during operation.

The tubular test section uses a greatly simplified geometry (Figure 6-16) with the inlet/outlet pipe effectively extending into the block, while the shroud forms a branch connection. The available material for reinforcement around the openings is more than sufficient for the tubular test section inlet/outlet block to be made of either SS316 or IN625. The inlet pipe is effectively extended so no branch connection occurs that requires reinforcement, while the shroud connection mimics the annular test section heated-rod pass-through, which is shown to be satisfactory in Table 6-16.

Table 6-21: Minimum Wall Thickness for each of the Test section Shrouds

Test section	t_{shroud} [mm]	SS316	IN600	IN625
		t_m [mm]	t_m [mm]	t_m [mm]
7-Rod-Bundle	11.08	9.50	-	4.23
Annular	9.10	7.57	-	3.37
Tubular	1.25	2.23	-	0.99

The shrouds are simple pipes supporting internal pressure without modification, and are treated using Equation 6.6 to determine their minimum wall thickness, with the results given in Table 6-21. Both the 7-rod-bundle and annular test section use NPS XXS piping for their shrouds which is sufficiently thick to use either SS316 or IN625 piping. The tubular test section, which uses the same specifications as the heated rods from the other two test sections for the shroud, requires the shroud to be made of IN625 to meet ASME code for the thermal-hydraulic loop design pressure and temperature. However, as the tubular test section shroud is also to act as the heating element, the necessary operating temperature will be much higher than the thermal-hydraulic loop design temperature. The ASME code only rates material to a maximum temperature of 650 °C which is much less than the maximum expected heating element temperature of 1130 °C necessary to raise the fluid temperature to 600 °C in the tubular test section. The ability of the shroud to perform at this temperature will be investigated along with the heated rods below.

The heated rods are thick-walled cylinders under uniform compression. Unlike a pipe under a simple internal pressure load, no simple formula (Equation 6.6) exists which allows for the calculation of a minimum wall thickness. In the case of both the heated rods and tubular test section shroud which fall outside of the rules governing ASME B31.1, the von Mises criterion will be employed to determine the minimum wall thickness. The von Mises equivalent stress is used to equate the stored strain energy to the yield stress in simple tension of a material to provide a

failure criterion; it has been used successfully to predict complex stress systems such as found in the test sections presented above [75].

To allow for the weld joints and possible constraints imposed on the test section due to the mounting configuration, the heated rods and tubular test section shroud will be considered to have rigid end supports. This provides for the worst case scenario where the imposed stress is maximized and the yield pressure minimized. As the failure criterion relates to the yield stress in simple tension and the ASME code only extends to 650 °C, the material data sheets provided by manufactures will be used to determine the yield stress at various temperatures (see Chapter 5). For a thick walled cylinder the von Mises criterion is represented by Equation 6.9. The principle stresses are determined by the boundary conditions imposed on the cylinders, given by Equation 6.10, where k is the radius ratio $\frac{r_o}{r_i}$. Atmospheric pressure is assumed to be constant at 0.1 MPa, while the pressurized face sees a constant 28.35 MPa as the design pressure. As the heated rods and tubular shroud have the same geometry, they only vary as being either externally or internally pressurized respectively.

$$(\sigma_\theta - \sigma_r)^2 + (\sigma_r - \sigma_z)^2 + (\sigma_z - \sigma_\theta)^2 = 2\sigma_Y^2 \quad (6.9)$$

$$\sigma_r = \frac{1}{k^2-1} \left[p_i \left(1 - \frac{r_o^2}{r^2} \right) - p_o k^2 \left(1 - \frac{r_i^2}{r^2} \right) \right] \quad (6.10.a)$$

$$\sigma_\theta = \frac{1}{k^2-1} \left[p_i \left(1 + \frac{r_o^2}{r^2} \right) - p_o k^2 \left(1 + \frac{r_i^2}{r^2} \right) \right] \quad (6.10.b)$$

$$\sigma_z = \nu(\sigma_r + \sigma_\theta) \quad (6.10.c)$$

where: σ : stress; p : pressure; k : radius ratio; ν : Poisson's ratio.

The inner surface of the cylinders will yield first, demonstrated in Figure 6-30, showing the variation of the principle stresses through a heated rod subjected to the design pressure, with the maximum von Mises equivalent stress occurring at the inner bore. Applying the principle stresses at the yielding surface for the components to the von Mises criterion provides the von

Mises equivalent stress for the cylinders at the design pressure. This is matched to the material's tensile strength-to-temperature ratio to provide the maximum permissible operating temperature of the component.

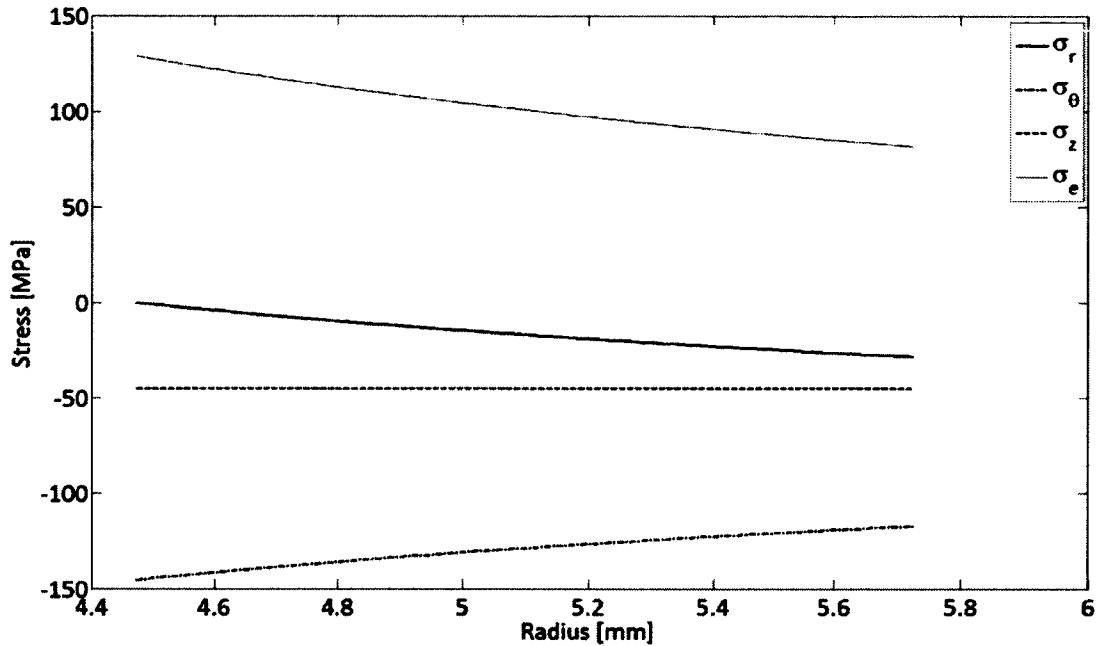


Figure 6-30: Principle and von Mises Stress Variation with Radius of a Heated Rod at 28.35 MPa

Table 6-22: Maximum Operating Temperature of Heated Test section Components IN625 [44]

Component	K	p_i [MPa]	p_o [MPa]	σ_r [MPa]	σ_θ [MPa]	σ_z [MPa]	σ_y [MPa]	T_{max} [°C]	T_{max} SF=2 [°C]
Heated Rod	1.279	0.1	28.35	-0.100	-145.34	-45.09	128.78	980	870
Tubular Shroud	1.279	28.35	0.1	-28.35	116.9	27.63	126.89	980	870

Based on the von Mises equivalent stress yield criterion the, heated rods are capable of operating up to 870 °C using a safety factor of two without yielding at the design pressure. This is greatly in excess of the maximum expected heated rod heating element temperature of 680 °C found in the annular test section, at which the heated rod would have a safety factor of 3.2. The tubular test section shroud is also able to operate up to 870 °C while retaining a safety

factor of two; however this is insufficient to heat the fluid to the desired 600 °C given the expected heat transfer coefficient. As designed, the tubular test section will be capable of heating the fluid to approximately 400 °C before reaching the materials limit. Thickening the tubular test sections shroud would allow it to operate at higher temperatures; however, it would further reduce the test sections electrical resistance reducing the power available for heat transfer systems. If the tubular test section is to heat the water past 400 °C at the design pressure, the shroud would need to be thickened, and a heating element design using layered coatings as found in the 7-rod-bundle need to be applied.

6.4.2 Sealing

Where test section is penetrated to allow the direct current to be delivered to the heating elements, the heated-rod pass-through, a seal is necessary to prevent the high pressure fluid from escaping between the components. The current must be contained to the heating element subsystem (delivery, element and ground) for experimental control and safety reasons; this requirement for electrical isolation prevents the components from being welded together to form a seal. Several different approaches to seal the opening and provide electric isolation are available, with some being successfully implemented in previous test section designs. Used by AECL on their rod bundle test section, is a graphite stuffing box [59]. This is a common method used to seal through hull shafts in nautical applications, and provides a low cost method of providing sealing for any geometry. Loose material is packed around the components to form a plug and is compressed to fill any gaps and prevent leakage. The seal formed by this method is never perfect and so a certain leakage rate must be accepted. For the test sections to be deployed at Carleton, zero leakage past the seals is mandated by the facility and design criterion, so the use of a stuffing box as implemented at AECL would be unacceptable.

Another common method of sealing co-axial shafts or piping, such as fittings between piping segments, is through the use of a compression ring between two mating faces that swages the inner tube to create a leak free seal. This design was popularized by Swagelok and is frequently used for high pressure pipe fittings. Demonstrated below in Figure 6-31, the sealing method requires two ferrules which are compressed against a non deformable body. As long as the ferrules are significantly harder than the tubing they are able to deform the tubing surface to form a gapless contact with the tubing while the matched mating faces of the ferrules complete the seal with the body.

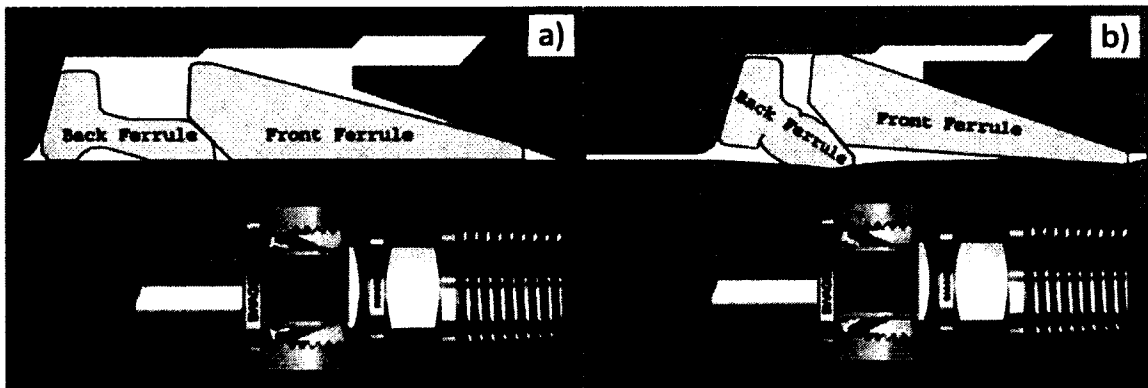


Figure 6-31: "316 SS Swagelok Tube Fitting with Advanced Geometry Back Ferrules."

a) Prior to Make-up, b) After Make-up [76]

Due to the requirement of the ferrules being significantly harder than the tubing and the stress concentrations introduced by the swaging the commercial designs from Swagelok using 316 SS are limited to a lower operating temperature at the design pressure than is necessary for use with the test section. The temperature limitation may be overcome by implementing a custom ceramic design, where such fittings have been used in gas turbine combustion chambers.

However, the design remains bulky with the ferrules and locking mechanism requiring significant space around the tube to form the seal. The high hardness of the heated rods and the

very limited spacing between them in the 7-rod-bundle arrangement makes the use of a Swagelok type seal unsuitable. The use of a ceramic ferrule would also present a problem at low temperatures where the material would be brittle and prone to failure where the back ferrule is subjected to bending during the make-up process. Due to the geometric limitations and the necessity to pressurize the system before heating requiring a low temperature high pressure sealing eliminates the possibility of using a swaging seal between the heated rods and the inlet/outlet block.

The test section designed for supercritical water at Xi'an Jiaotong University uses a cooled flange design as shown in Figure 6-5 (repeated below for convenience); the test section is designed to operate up to 25 MPa with component temperatures never exceeding 550 °C [25]. The flanges are actively cooled which allows for improved performance of the material in handling the pressure loads, while permitting an insulating gasket material to be used as covered in the report by Masih et al [5]. The power delivery and arrangement requires that the section of the flange that is attached to the test section (outer flange half) be energized, with the test section being isolated by the gasket material and an electrically insulated sleeve covering the bolts. The integral flange section bonded to the test section (inner flange half) has a larger bore to allow the heated rod to pass through without risk of contact. The heated rod is bonded and sealed to the outer flange half with a retention nut and gasket material. The sealing method employed to seal the test section at Xi'an Jiaotong University uses active cooling to allow the use of a common ASME flange system. This is attractive from a safety and certification perspective. The flange design may also be extended so the seal is formed around any internal feature, such as the increased bore size Xi'an Jiatong test section, or the 7-rod-bundle designed for the Carleton test section. The thermal-hydraulic loop design at Carleton does not provide for active cooling of components, so a modified sealing method will have to be utilized.

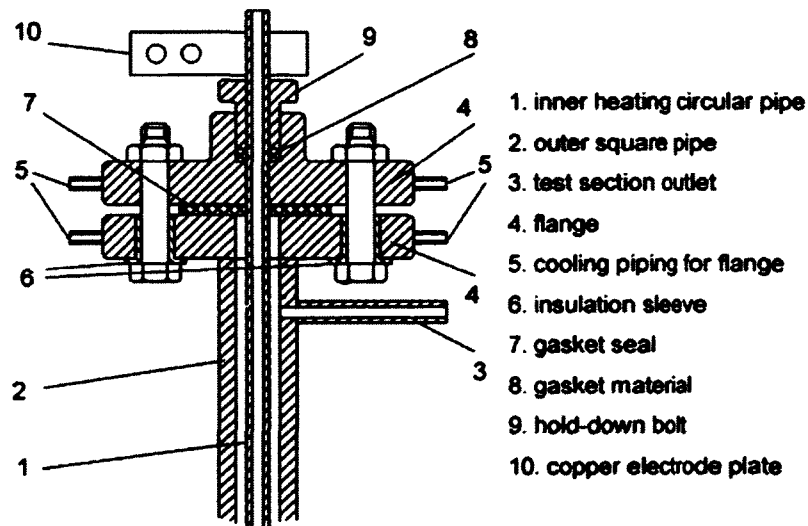


Figure 6-5: “Leak-proof seal and insulation structure of the [Xi’an Jiaotong] test section” [25]

To avoid actively cooling the flanges the gasket material must be capable of withstanding the maximum operating temperature. Using the design temperature of the thermal-hydraulic loop (625 °C) to ensure a safe operating margin, traditional elastomeric gasket materials are incapable of operating at desired temperatures. The gasket must therefore be a metallic type; the various options being covered in detail by Mashri et al [5]. Based on their extensive analysis, a flange with a ring-type joint and metal ring is the most suitable for the test section design temperature and pressure; the analysis and alternate flange types will not be repeated.

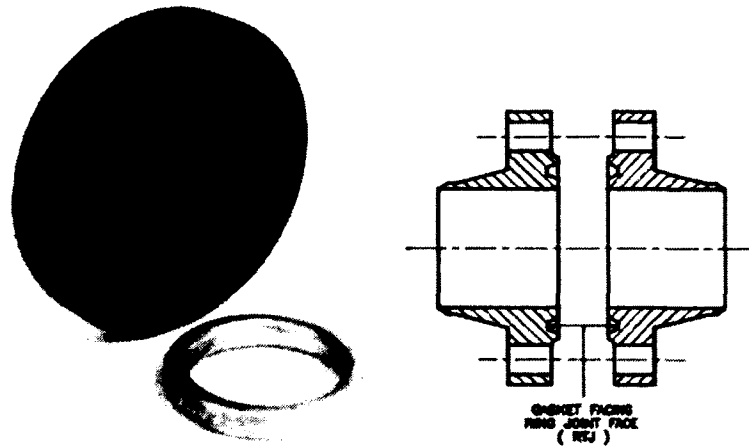


Figure 6-32: "Flange with Ring-type Joint Face" [5]

The purpose of the gasket material is to provide a soft, deformable material between the hard flange faces to ensure complete contact and ensure sealing capacity between mating parts.

Copper is a typical metallic gasket material as it is both soft, compared to either 316 SS or IN625, and ductile; its melting point is greater than 1000 °C allowing it to be used even at the hot end of the test section [5] [64]. Since the electrical bus is already made of copper and located on the outer face of the inlet/outlet blocks for the 7-rod-bundle and annular test section, the bus is extended to provide the metal ring for the flange (shown below). The electrical bus used as the gasket then forms a hybrid flange type combining the effects of a ring-type joint and flat face joint.

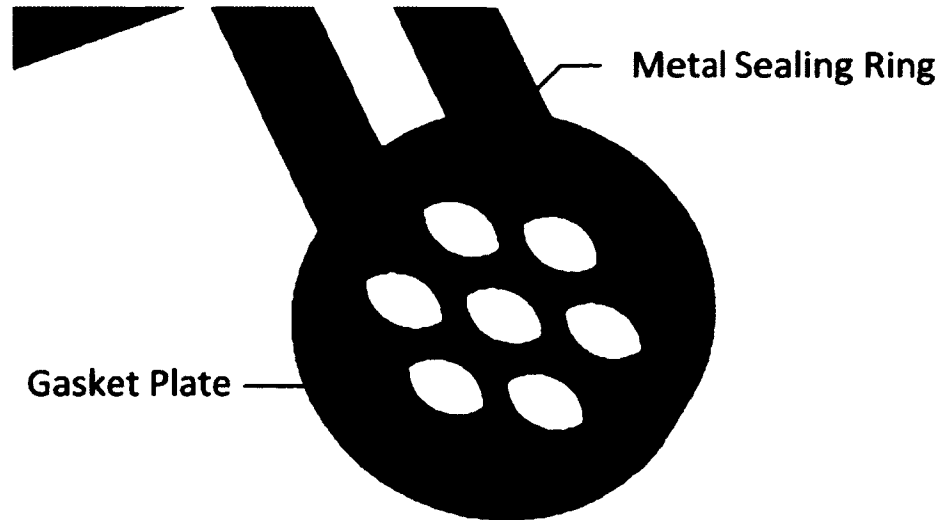


Figure 6-33: Copper Electrical Bus as Flange Ring and Gasket

The inlet/outlet block rear face is used as one half of the flange, with a mating groove cut into it to accept the metal sealing ring on the electric bus. A flange cap (Figure 6-34) makes up the other half of the flange. The cap is designed to fit over the copper bus and mate with the rear face of the inlet/outlet block. A mating groove, highlighted in blue in Figure 6-34 below, is cut around the inner electrical bus mating face. The gasket plate portion of the electrical bus thus acts as a typical gasket pad between the inlet/outlet block and flange cap, while the metal sealing ring ensures sealing contact where the flange cap mates with the inlet/outlet block. The flange cap has two slots cut into it to allow the delivery rails to connect the bus bar to the gasket plate, as discussed above. A set of eight $\frac{1}{4}$ " threaded studs hold the assembly together and provide the clamping force to seal the flange. The studs are welded to the inlet/outlet block as though fittings would be inappropriate. The entire assembly is shown for the 7-rod-bundle test section in Figure 6-24 in Section 6.3.4 and the geometry of the flange cap is given in Table 6-23.

Table 6-23: Flange Cap Geometry, 7-Rod-Bundle and Annular Test sections

Test section	7-Rod-Bundle	Annular
Total Length [mm]	50.0	
Superior OD [mm]	87.7	
Superior OD Length [mm]	25.4	
Inferior OD [mm]	75.0	
Electric Bus Bore Depth [mm]	10.0	
Electric Bus Bore OD [mm]	47.0	
Sealing Ring Depth [mm]	2.00	
Sealing Ring OD [mm]	49.0	
Bolt Radial Pitch [mm]	31.0	
Bolt Hole Diameter [in]	¼	
Heated Rod Pass Through Bores	7	1

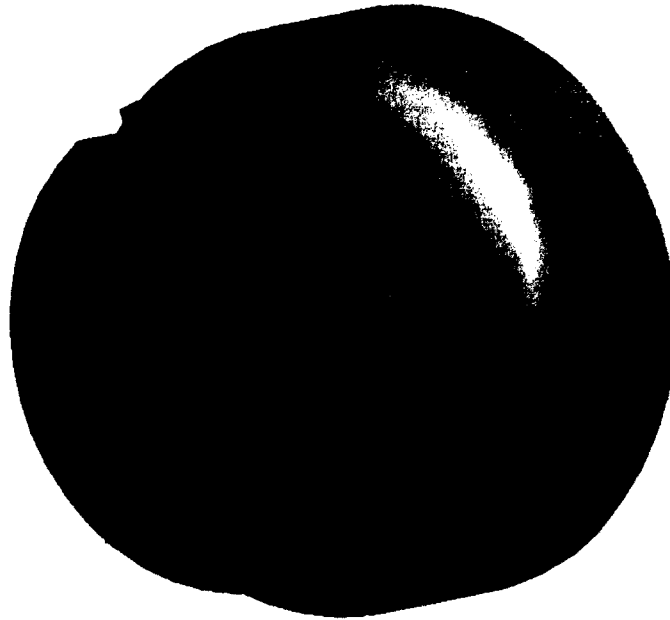


Figure 6-34: Flange Cap, 7-Rod-Bundle Test section

The use of a metal ring to provide the sealing capacity complicates isolating the electrical power delivery and removal as all the flange components are conducting. A dielectric must be inserted between the electric bus and heated rods and the remaining test section components. While the operating temperature is too high for traditional elastomere dielectrics, such as a silicone or rubber, many components are already being coated with alumina for electric insulation. Extending this coating to the inlet/outlet block rear face and heated rod pass through, along with

the flange cap will provide the necessary dielectric insulation. A 20 μm coating on these parts will be sufficient for the maximum voltage as was previously discussed in Section 6.3.4. Ceramics make poor gasket material due to their high hardness and brittleness. However, as a facing material their increased hardness compared to the flange parent material will improve the copper's response as a gasket material. As alumina's hardness is orders of magnitude higher than copper, alumina's suitability as a face coating for the insulated components will only depend on its ability to sustain the loading required to yield the copper without exceeding its own flexural strength. While the loading of the alumina coatings will be exclusively compressive, the tensile performance will be used as internal defects and local geometry can lead to tensile or bending loads which will lead to a tensile failure mode. The flexural strength of the alumina used is the lowest value reported, and will provide a conservative estimate of the coatings performance [61]. Comparing the performance of the alumina's and copper's strength with temperatures from Chapter 5, grade A3 alumina's flexural strength exceeds copper's yield strengths the entire temperature range. This ensures the flange may be sufficiently loaded to deform the copper gasket material to create the desired seal without failing the alumina coating and potentially compromising the electrical insulation.

The ends of the heated rods may be welded directly to the flange cap to create the necessary seal as the flange caps do not provide a grounding path for the direct current to flow through. The additional load due to the constrained ends and thermal expansion mismatch between the heated rods and test section was previously accounted for in Section 6.4.1, so using a weld joint will not affect the structural performance of the heated rods. The flange cap design, if constructed of IN625, provides sufficient thickness to meet ASME code for a closure at the thermal-hydraulic loop design temperature and pressure, so will not need active cooling.

Chapter 7 Conclusions and Future Work

The work presented above satisfies the twin goals of the author: the development of a numerical tool capable of predicting the loop's transient thermal response, and the preliminary design of the initial set of test sections. The details of the work are summarized below, and a discussion of the recommended future work is presented.

7.1 Transient Thermal Numerical Solver

7.1.1 – Numerical Solver and Simulation Results

An explicit numerical solver was developed to investigate transient thermal behaviour of a supercritical thermal-hydraulic loop. The numerical solver uses the lumped heat capacity model for heat transfer effects, and friction losses in piping flows from the Moody chart to determine the pressure field. The solver is capable of handling two dimensional heat transfer and one dimensional fluid flow with a variety of boundary and source conditions. Mesh generation is handled by the code, and is capable of dealing with non-uniform mass distributions while maintaining accuracy of the lumped heat capacity model. A von Neuman stability analysis is performed on the discretization scheme, and a Courant number enforced to determine the optimal time step that remains stable throughout the simulation.

The code was used to predict the proposed Carleton SCW thermal hydraulic loop's transient thermal behaviour for the proposed start-up procedure. This data is can be used to refine the start up procedure to reduce the energy cost of bringing the loop to conditions necessary for experimentation. The predicted pressure profile and heat exchanger performance provides important feedback on the listed performance of manufactures components, and necessary pumping power and schedule.

7.1.2 Suggested Future Simulation Work

As discussed in Chapter 3, additional experimental data is necessary to improve the Nusselt number correlation in the near critical region. The disparity between the available correlations and the experimental data represents the greatest source of error in the numerical simulation. Improving the correlation for convective heat transfer in supercritical fluid will greatly improve the utility of the numerical solver.

Additional simulations should be run to provide additional feed back to the Carleton supercritical fluids group. Running different start up scenarios will allow the initialization procedure to be optimized in total time and energy costs, while avoiding any compromise in safety. Shut down modeling should also be performed for the sake of completeness and additional validation data, though it would not impact the shut down procedure.

The numerical solver also provides a useful tool for accident and emergency situation investigation. For certain situations, such as the loss of cooling in the heat exchanger while power is being applied to the test section, the code may be used to examine if additional damage or failures will arise due to the initial failure. Minor modifications to the code would extend this capability to include loss of containment of the fluid, and the subsequent depressurization of the loop during operation.

7.2 Thermal-hydraulic Loop Test sections

7.1.1 Test section Designs

Three test sections were designed to satisfy the experimental requirements laid forth to the Carleton supercritical fluids group; these include a tubular, annular and rod-bundle geometry. The test sections are all designed to have a common interface with the thermal-hydraulics loop to facilitate easy replacement and are fully reversible to allow for experiments with up-flow or

down-flow conditions. Each design is matched to the available power to provide the widest experimental range possible. The annular and rod-bundle test sections are capable of heating the fluid to 600 °C at a pressure of 25 MPa, while the tubular test section is mechanically limited to a maximum fluid temperature of 475 °C at 25 MPa as the wall temperature reaches the maximum permissible value. Each test section is designed to meet *ASME Power Piping* code to simplify the certification process.

7.1.2 Material Selection

Based on operating temperatures and stress, as well as corrosion behaviour, Inconel 625 is the preferred material for pressure containing components of the test sections. Its superior high-temperature strength allows the test section designs to meet their experimental requirements while staying within desirable geometry bounds. To complement the Inconel 625 base performance, a number of coatings are employed to tailor the test section's response in a given situation. To match the test section's electrical resistance to the power supplies resistance, allowing for maximum heat input to the fluid, in an unfavourable geometry, a custom heating element, in the form of a Kanthal coating, is applied to the heated rods. Coatings for electrical insulation and corrosion resistance can be satisfied with a common ceramic, alumina. Alumina's properties allow it to excel in each different role it is required for throughout the test sections. Copper, which may also be applied as a coating, is used wherever a low resistance conductor is required.

7.1.3 Suggested Future Test section Work

To confirm the test sections' safe operation at maximum pressure and temperature loads, a detailed thermal-structural analysis should be performed with a numerical multi-physics package. This will supplement the ASME code design guides, and allow for the transient

behaviour of the test section to be observed during start-up or a failure event. ANSYS multi-physics solver (structural) is capable of simulating coupled thermal-structural problems including contact. The program would provide a suitable numerical tool, given its industry recognition and extensive validation by its parent company. It is currently employed by other research groups at Carleton. Given ANSYS multi-physics' capabilities and availability, it is recommended for the thermal-structural simulations to be performed on the test sections.

List of References

1. **Canada, Natural Sciences and Engineering Research Council of.** Generation IV Energy Technologies Program. [Online] NSERC, 08 31, 2009. http://www.nserc-crsng.gc.ca/Professors-Professeurs/RPP-PP/GENIV-GENIV_eng.asp.
2. **Association, World Nuclear.** Supercritical Water-Cooled Reactors. *Generation IV Technology Systems*. [Online] <http://www.gen-4.org/Technology/systems/scwr.htm>.
3. —. Generation IV Nuclear Reactors. [Online] December 2010. <http://world-nuclear.org/info/inf77.html>.
4. **Diamond, David J.** *Generation IV Nuclear Energy Systems How They Got Here and Where They are Going*. [PDF] s.l. : Brookhaven Science Associates, DOE, 2003.
5. **Masih Balouch, Anne Mason, Rubisel Alena, Yi-Li Jin.** *Supercritical Water Loop Design Report*. Ottawa : Unpublished, 2010.
6. **Oceaneering.** Grayloc Connectors. *Grayloc Products*. [Online] May 2010. <http://www.oceaneering.com/oceandocuments/brochures/subseaproducts/GRLC%20-%20The%20Ultimate%20Connector.pdf>.
7. **Jermy R. Licht, Mark H. Anderson, Michael L. Corrandini, Riccardo Bonazza.** *Heat Transfer Phenomena in Supercritical Water*. Madison : Department of Energy, 2007. DE-FG07-04ID14602.
8. *The Velocity and Temperature Distribution in One-Dimensional Flow with Turbulence Augmentation and Pressure Gradient.* **Wolfshstein, M.** s.l. : Int. J. Heat Mass Transfer, 1968, Vol. 12, pp. 301-318.
9. **Modisette, J.** *Pipeline Thermal Models*. s.l. : Energy Solutions International, 2002.
10. **Termis.** User Manual v. 2.093. s.l. : 7-Technologies, 2011.
11. **Studio, Pipeline.** Pipeline Studio Application and Technical Overview White Paper. s.l. : Energy Solutions International, 2002.
12. **Gabrielaitiene, Irina.** *Modelling of Turbulent Flow and Heat Transfer Phenomena in Pipes of District Heating Systems Including Transient Temperature Propagation*. Lund : Lund University, 2006.
13. *One-Dimensional Stability of Dissipative Couette Flow.* **V.L. Mazo, N.S. Ruderman.** 5, s.l. : PPM USSR, 1986, Vol. 50, pp. 647-679.

14. *Unsteady Conjugated Heat Transfer in Laminar Pipe Flows with Step Change in Ambient Temperature.* **W. M. Yan, T. F. Lin.** s.l. : Int. Comm. Heat Mass Transfer, 1987, Vol. 14, pp. 699-707.
15. *Unstead conjugated forced convective heat transfer in a duct with convection from the ambient.* **Sucec, J. 9,** s.l. : Int. J. Heat Mass Transfer, 1987, Vol. 30, pp. 1963-1970.
16. *Unsteady forced convection heat transfer in a channel.* **J. Sucec, D. Radley.** 4, s.l. : Int. J. Heat Mass Transfer, 1990, Vol. 33, pp. 683-690.
17. *Periodic Laminar Forced Convection Within Ducts Including Wall Heat Conduction Effects.* **R.O.C Guedes, R.M. Cotta.** 5, s.l. : Int. J. Engng. Sci, 1991, Vol. 20, pp. 535-547.
18. *Theory of one-dimensional and quasi-one-dimensional heat conduction.* **Gladkov, S. O.** 7, s.l. : Tech. Phys., 1997, Vol. 42.
19. **Incropera, DeWitt, Bergman, Lavine.** *Fundamentals of Heat and Mass Transfer 6th ed.* Mississauga : John Wiley & Sons, 2007.
20. *Operational Optimization in a District Heating System.* **A. Benonysson, B. Bohm, H. Ravn.** 5, s.l. : Energy Conversion and Management, 1995, Vol. 36, pp. 297-314.
21. *Modeling temperature dynamics of a district heating system in Naestved, Denmark A case study.* **I. Gabrielaitiene, B. Bohm, B. Sunden.** s.l. : Energy Conversion and Management, 2006, Vol. 48, pp. 78-86.
22. **White, Frank M.** *Fluid Mechanics 5th ed.* Ney York : McGraw-Hill, 2003.
23. **Engineering, LMNO.** Weymouth, Panhandle A and B equations for Compressible Gas Flow. [Online] LMNO Engineering, Research, and Software, Ltd., 2003. <http://www.lmnoeng.com/Flow/weymouth.htm>.
24. **Department, Engineering.** *Flow of Fluids Through Valves, Fittings and Pipe.* Stamford : Crane Co., 2009. 1-40052-712-0.
25. *Experimental investigation on heat transfer from a heated rod with a helically wrapped wire inside a square vertical channel to water at supercritical pressures.* **Hongzhi Li, Haijun Wang, Yushan Luo, Hongfang Gu, Xiaobao Shi, Tingkuan Chen, Exkart Laurien, Yu Zhu.** s.l. : Nuclear Engineering and design, 2009, Vol. 239, pp. 2004-2012.
26. **W. Kays, M. Crawford, B. Weigand.** *Convective Heat and Mass Transfer 4th ed.* New York : McGraw-Hill, 2005.
27. *Heat transfer to supercritical fluids flowing in channels-empirical correlations (survey).* **I. L. Pioro, H. F. Khatabil, R. B. Duffey.** s.l. : Nuclear Engineering and Design, 2004, Vol. 230, pp. 69-91.

28. *Numerical investigation of heat transfer in upward flows of supercritical water in circular tubes and tight fuel rod bundles.* J. Yang, Y. Oka, Y. Ishiwatari, J. Liu, J. Yoo. s.l. : Nuclear Engineering and Design, 2007, Vol. 237, pp. 420-430.
29. *A comparative CFD investigation of helical wire-wrapped 7, 19 and 37 fuel pin bundles and its extendibility to 217 pin bundle.* R. Gajapathy, K. Velusamy, P. Selvaraj, P. Chellapandi, S.C. Chetal. s.l. : Nuclear Engineering and Design, 2009, Vol. 239, pp. 2279-2292.
30. *CFD analysis of thermal-hydraulic behavior in SCWR typical flow channels.* H.Y. Gu, X. Cheng, Y.H. Yang. s.l. : Nuclear Engineering and Design, 2008, Vol. 238, pp. 3348-3359.
31. *Numerical analysis of heat transfer in supercritical water cooled flow channels.* X. Cheng, B. Kuang, Y.H. Yang. s.l. : Nuclear Engineering and Design, 2007, Vol. 237, pp. 240-252.
32. *An algorithm for low Mach number unsteady flows.* Ivan Mary, Pierre Sagaut, Michel Deville. s.l. : Computers & Fluids, 2000, Vol. 29, pp. 119-147.
33. *High Order Explicit Methods for Parabolic Equations. 2,* s.l. : BIT, 1998, Vol. 38, pp. 372-390.
34. *CFD-based application of the Nyquist criterion to thermo-acoustic instabilities.* J. Kopitz, W. Polifke. s.l. : Journal of Computational Physics, 2008, Vol. 227, pp. 6754-6778.
35. *The extension of incompressible flow solvers to the weakly compressible regime.* C.-D. Munz, S. Roller, R. Klein, K.J. Geratz. s.l. : Computers & Fluids, 2003, Vol. 32, pp. 173-196.
36. *in viscous subsonic flow models with nonreflecting boundary conditions.* Dorodnitsyn, L. V. 2, s.l. : Computational Mathematics and Modeling, 2000, Vol. 11, pp. 356-376.
37. *Compressible Navier-Stokes system in 1-D.* Mucha, Piotr Bouguslaw. s.l. : Mathematical Methods in the Applied Sciences, 2001, Vol. 24, pp. 607-622.
38. *Vanishing viscosity limit to rarefaction waves for the Navier-Stokes equations of one-dimensional compressible heat-conduction fluids.* Song Jiang, Buoxi Ni, Wenjun Sun. 2, s.l. : SIAM J. Math Anal., 2006, Vol. 38, pp. 368-384.
39. Dale A. Anderson, John C. Tannehill, Richard H. Pletcher. *Computational Fluid Mechanics and Heat Transfer.* New York : McGraw-Hill, 1984.
40. *Comparison of the SMA, PSIO and ITA Schemes for Unsteady Flows.* S. W. Kim, TJ Benson. 3, s.l. : Computers Fluids, 1992, Vol. 21, pp. 435-454.
41. **Advanced Industrial Components Inc.** Heat Exchanger Specification Sheet. s.l. : Unplished, 2010.
42. **Ogata, Katsuhiko.** *Modern Control Engineering 4th ed.* Upper Saddle River : Prentice Hall, 2002.

43. **John, Aneesh.** *Computational Domain Section With Supercritical Property Valication.* s.l. : Unpublished, 2010.
44. **Special Metals.** INCONEL Alloy XXX Data Sheet. [Online] 2008.
<http://www.specialmetals.com/products/index.php>.
45. *The effect of Nb, Ti, Al on precipitation and strengthening behavior of 718 type superalloys.* **Xishan Xie, Jianxin Dong, Gailian Wang, Wei You, Jinhui Du, Changhong Zhao, Zhigang Wang, Carneiro, T.** Warrendale, PA : TMS, 2006. Superalloys 718,625,706 and Derivatives. Proceedings of the Sixth International Symposium on Superalloys 718, 625, 706 and Derivatives. pp. 287-298.
46. *Work-hardening behavior of the Ni-Fe based superalloy IN718.* **K.V.U. PRAVEEN, G.V.S. SASTRY, and VAKIL SINGH.** 1, s.l. : Metallurgical and Materials Transactions A, 2008, Vol. 39, pp. 65-78.
47. *Gamma prime coarsening and age-hardening behaviors in a new nickel base superalloy.* **Shuangqun Zhao, Xishan Xie, Gaylord D. Smith, Shailesh J. Patel.** s.l. : Materials Letters, 2004, Vol. 58, pp. 1784-1787.
48. *The Temperature Dependence of γ' Volume Fraction in a Ni-Based Single Crystal Superalloy from Resistivity Measurements.* **B. Roebuck, D. Cox and R. Reed.** s.l. : Scripta Materialia, 2001, Vol. 44, pp. 917-921.
49. **The American Society of MEchanical Engineers.** *Power Piping, ASME Code for Pressure Piping, B31.* New York : ASME, 2004.
50. **MatWeb.** Alloy Composition Database. *MatWeb.* [Online]
<http://www.matweb.com/index.aspx>.
51. **Haynes International.** Haynes 556 Alloy. [Online]
<http://www.haynesintl.com/pdf/h3013.pdf>.
52. *General corrosion properties of modified PNC1520 autenitic stainless steel in supercritical water as a fuel cladding candidate material for supercritical water reactor.* **Y. Nakzono, T. Iwai and H. Abe.** s.l. : Journal of Physics: Conference Series, 2010, Vol. 215.
53. *Corrosion behavior of Hastelloy C-276 in supercritical water.* **Zhang, Qiang, et al.** 9, s.l. : Corrosion Science, 2009, Vol. 51, pp. 2092-2097.
54. *Corrosion Phenomena Associates with SCWO Systems.* **D.B Milton, J.C Orzalli and R.M Lantanision.** s.l. : Proceedings of the Third International Symposium on Supercritical Fluids, 1994, Vol. 3, p. 43.
55. *Corrosion resistance of high-Cr oxide dispersion strengthened ferritic steels in super-critical pressurized water.* **H.S Cho, A. Kimura.** s.l. : Journal of Nuclear Materials, 2007, Vols. 367-370, pp. 1180-1184.

56. *Corrosion Screening Tests of High-Performance Ceramics in Supercritical Water Containing Oxygen and Hydrochloric Acid.* Nikolaos Boukisa, Nils Claussenb, Klaus Eberta, Rolf Janssenb and Michael Schacht. s.l. : Journal of European Ceramic Society, 1996, Vol. 17, pp. 71-76.
57. *Corrosion of alumina ceramics in acidic aqueous solutions at high temperatures and pressures.* M. Schacht, N. Boukis, E. Dinjus. s.l. : Journal of Materials Science, 200, Vol. 35, pp. 6251-6258.
58. *Corrosion of zirconia ceramics in acidic solutions at high pressures and temperatures.* Michael Schachta, Nikolaos Boukisa, Corresponding Author Contact Information, Eckhard Dinjusa, Klaus Eberta, Rolf Janssenb, Frank Meschkeb and Nils Claussen. s.l. : Journal of the European Ceramic Society, 1998, Vol. 18, pp. 2373-2376.
59. *Assessment of Boiling-Length-Average Heat-Flux Approach for Predicting Dryout Power in CANDU 37-Element Bundles.* Leung, Laurence K.H. Kanazawa : The 13th International Topical Meeting on Nuclear Reactor Thermal Hydraulics, 2009.
60. **Accuratus.** Materials. [Online] 2002. <http://accuratus.com/materials.html>.
61. **Auerkari, Pertti.** *Mechanical and physical properties of engineering alumina ceramics.* s.l. : VTT Manufacturing Technology, 1996.
62. **SANDVIK.** *Kanthal Super Electric Heating Element Handbook.* s.l. : AB Sandvik Materials Technology, 2010.
63. **Copper Development Association.** *High Conductivity Coppers.* s.l. : Int. Copper Assoc., 1998. CDA Pub. 122.
64. **Advanced Energy Technology Group.** Copper Material Properties. [Online] <http://www-ferp.ucsd.edu/LIB/PROPS/PANOS/cu.html>.
65. *Experimental heat transfer of supercritical carbon dioxide flowing inside channels (survey).* Romney B. Duffey, Igor L. Pioro. s.l. : Nuclear Engineering and Design, 2005, Vol. 235, pp. 913-924.
66. **Teshima, Paul.** *Fouling Rates from a Sodium Sulphate – Water Solution in Supercritical Water Oxidation Reactors.* Vancouver : Dept. Mech. Eng, UBC, 1997. M.S. Thesis.
67. *Heat transfer to water at supercritical pressures in a circular and square annular flow geometry.* Jeremy Licht Mark Anderson, and Michael Corradinia. 1, s.l. : Int. Journal of Heat and Fluid Flow, 2008, Vol. 29, pp. 156-166.
68. *Forced Convective Heat Transfer to Supercritical Water Flowing in.* Yamagata K, Nishikawa K, Hasegawa S, Fujii T. s.l. : International Journal of Heat and Mass Transfer, 1971, Vol. 15, pp. 2575-2593.

69. Junjie Gu, Chukwudi Azih, Daniel McGuire. *Thermal Hydraulics Loop: Detailed Design*. s.l. : Unpublished, 2010.
70. *Mixed Convection heat transfer to water flowing through a vertical passage of annular Cross Section: Part 2*. Tian-Hua Wu, Zeyuan Xu and J.D Jackson. A, s.l. : Trans IChemE, 2002, Vol. 80.
71. *Single-phase convective heat transfer in rod bundles*. Mary V. Holloway, Donal E. Beasley, Michael E. Conner. s.l. : Nuclear Engineering and Design, 2008, Vol. 238, pp. 848-858.
72. *Subchannel analysis of supercritical light water-cooled fast reactor assembly*. Jaewoon Yoo, Yoshiaki Oka, Yuki Ishiwatari, Jue Yang and Jie Liu. s.l. : Nuclear Engineering and Design, 2007, Vol. 237, pp. 1096-1105.
73. *CFD analysis of thermal-hydraulic behaviour in SCWR typical flow channels*. H.Y. Gu, X. Cheng, Y.H. Yang. s.l. : Nuclear Engineering and Design, 2008, Vol. 238, pp. 3348-3359.
74. Cooper Crouse-Hinds. E1017 Series. [Online] <http://store.jbn-duraline.com/category/7>.
75. PP Benham, RJ Crawford & CG Armstrong. *Mechanics of Engineering Materials 2nd ed*. Essex : Prentice Hall, 1996.
76. Swagelok. 316 Stainless Steel Swagelok Tube Fittings with Advanced Geometry Back Ferrules. [Online] 2003. <http://www.swagelok.com/downloads/webcatalogs/EN/MS-06-16.PDF>.
77. American Society for Testing and Materials. *Test Method for Thermal Conductivity of Solids by Means of Guarded-Comparative-Longitudinal Heat Flow Technique*. s.l. : ASTM Int, 2009. ASTM E1223-9.
78. —. *Standard Test Method for Thermal Conductivity of Liquids*. s.l. : ASTM Int., 2009. ASTM D2717-95.

Appendix A: Conductive and Convective Heat Transfer Theory

The study of heat transfer in engineering applications is broken down into three categories: conduction, convection and radiation. Conduction and convection effects are significant in the thermal-hydraulics loop thermal modeling, while radiation effects are made insignificant by design, and will not be discussed further.

Conduction is the energy transfer process that occurs when two atoms or molecules collide and exchange kinetic energy. The random nature of the atoms or molecules motion makes conduction a diffusive mechanism. This phenomenon is well represented macroscopically by Fourier's law of conduction (Eqn. A.1). This postulates that the heat flux through a surface due to conduction is linearly proportional to the temperature gradient at the surface. A proportionality constant based on the material, its conductivity, is used to generate the equality:

$$\dot{q}_{cond}'' = -k \frac{\partial T}{\partial x_i} \quad (A.1)$$

Given the materials conductivity and temperature gradient, the heat transfer may be determined in this way. A material's conductivity is determined experimentally for both solids and fluids [77][78]. The conductivity coefficient is a strong function of temperature with a weak pressure dependency. As conduction is dependent on collisions between molecules, there is a dramatic change in a materials thermal conductivity between phases, dropping dramatically from solid, through liquid, to vapour as the molecules mean free path continues to increase. These trends are shown below in Figure A-1, showing the thermal conductivity for water in its liquid, vapour and supercritical phases.

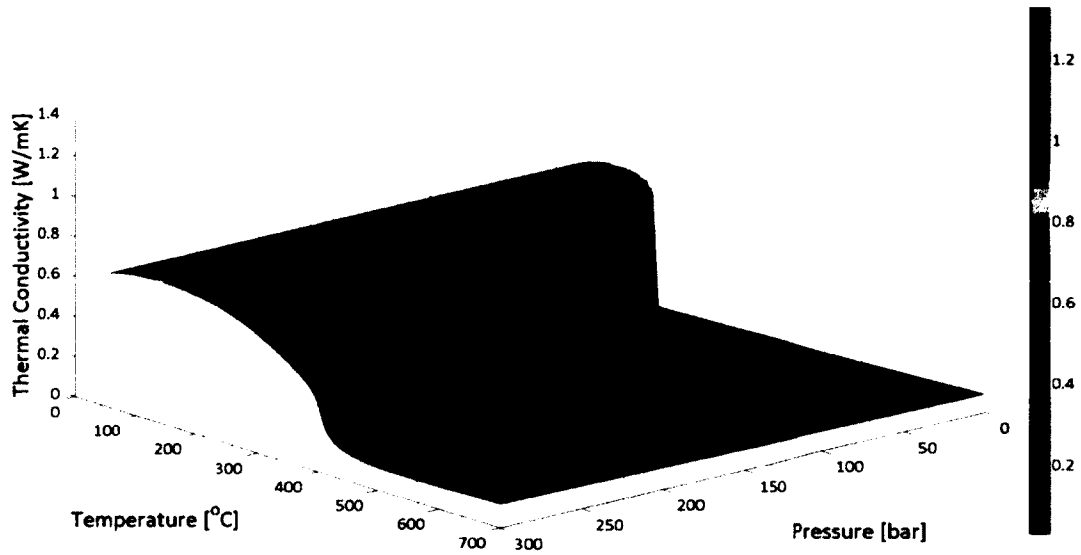


Figure A-1: Thermal Conductivity of Water

An exception to the general behaviour occurs around the critical point, where a singularity exists and the thermal conductivity approaches infinity as the temperature and pressure approach the critical point asymptotically. This greatly increased thermal conductivity near the critical point makes supercritical fluids advantageous for heat transfer applications.

In problems involving flow, due to the advection of thermal energy by the fluid, the temperature gradient field's dependency on time can become very complex, with the change in fluid properties due to transport mechanisms often dominating over diffusion effects. Flow over a flat plate with heat transfer is illustrated in Figure A-2, for both laminar and turbulent flow. In both cases the bulk flow continues to bring cool fluid and removes the heated fluid, preventing a buildup of heat. In the case of turbulent flow, eddies within the bulk flow provide additional mechanisms to mix the flow in addition to the bulk motion, improving heat transfer.

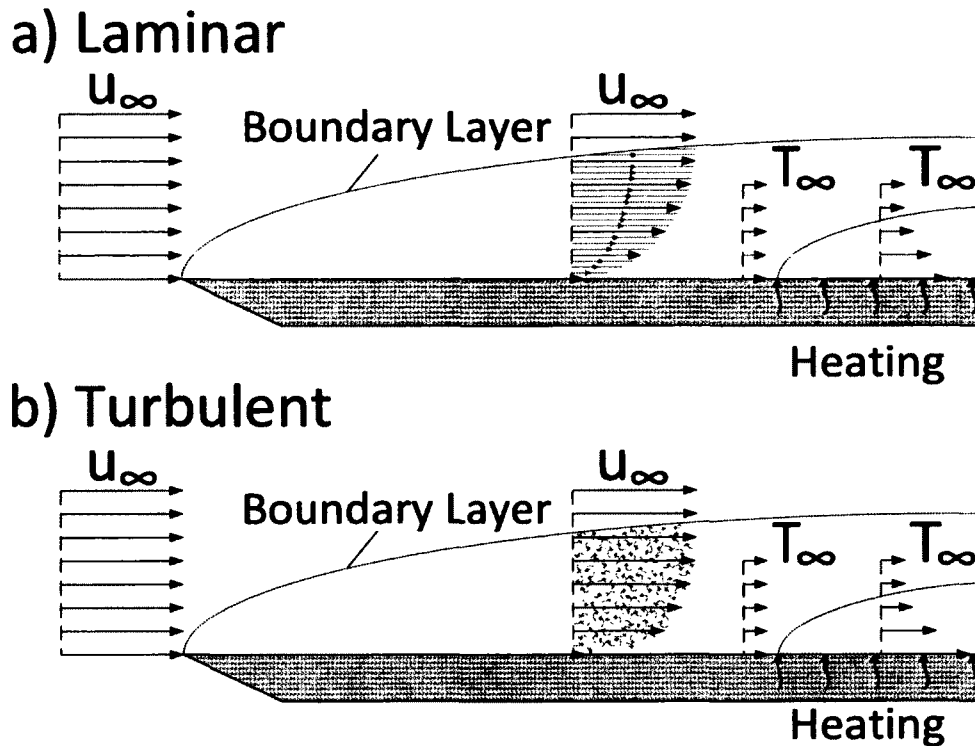


Figure A-2: Boundary layer velocity and temperature distributions. a) Laminar, b) Turbulent

In cases where flow is present, it is desirable to combine the advection and diffusion effects into a single parameter when the system is well known to simplify the problem. This approach has proved very successful for well studied heat transfer problems including, internal pipe flow [26]. A combined view point of both advection and diffusion effects results in a convection heat transfer view point. Convection heat transfer is defined using Newton's law of cooling (Eqn. A.2) using a convective heat transfer coefficient h and the temperature difference across the flow to define the heat flux through a surface bounding the flow.

$$\dot{q}''_{conv} = h_{conv}(T_s - T_\infty) \quad (\text{A.2})$$

Newton's law of cooling has the additional advantage of linearizing the problem, which greatly simplifies the solutions computation. The challenge with solving a convection heat transfer problem is determining the convective heat transfer coefficient. The common approach is to

utilize a non-dimensional parameter that allows one to correlate the coefficient to a large variety of situations. The convective heat transfer coefficient is captured by employing either the Nusselt or Stanton number, which are complimentary to each other. The Nusselt number will be used exclusively for all future considerations with no loss of generality.

$$Nu = \frac{h_{conv}L}{k_f} \quad (A.3)$$

A large body of experimental work has shown that the Nusselt number is a function of the Reynolds and Prandtl numbers (Eqn. A.5, A.6) in forced convection, giving rise to numerous empirical correlations covering many different geometries and flow arrangements. This work is well documented and may be found in any introductory text on convective heat transfer [26]. The reader is directed to these for a detailed explanation of the development of the correlations. Of particular interest to the heat transfer problem found in the thermal-hydraulic loop is forced convection of internal turbulent flows. Across all flow variations seen in the thermohydraulic loop's operation, the following empirical formulation for the Nusselt number, given by Sleicher and Rouse, can be utilized [26].

$$Nu = 5 + 0.015Re^a Pr^b \quad (A.4.a)$$

$$a = 0.88 - \frac{0.24}{4+Pr}; b = 0.333 + 0.5e^{-0.6Pr} \quad (A.4.b)$$

The correlation is stated to be valid across the ranges of $0.1 < Pr < 10^4$ and $10^4 < Re < 10^6$, and within three to four percent of experimental results [26]. The Reynolds and Prandtl numbers are defined respectively:

$$Re = \frac{m''L}{\mu} \quad (A.5)$$

$$Pr = \frac{c_p \mu}{k} \quad (A.6)$$

For fluids with a sufficiently high Prandtl number ($Pr > 0.5$) in turbulent flow, limiting heat transfer effects are confined to the flow's sublayer region [26]; the geometry of the duct, compared to a circular cross section, does not factor into the determination of heat transfer as long as the change in perimeter versus a circular duct is accounted for. To account for the perimeter change, one introduces an effective diameter, called the hydraulic diameter, as the length characteristic for all geometries.

$$D_h = \frac{4A_c}{P} \quad (\text{A.7})$$

By normalizing the flows cross sectional area to the perimeter one generates a correlation between any ducts flow and the potential area for heat transfer. In the simple case, a circular cross section, the hydraulic diameter reduces to the diameter of the circular cross section.

Combining the above Equations the local convective heat transfer coefficient may be determined at any point knowing the geometry, Reynolds number and Prandtl number. From this convective heat transfer coefficient, the local heat flux may be solved.

$$\dot{q}_{conv}'' = \frac{k_f}{D_h} (5 + 0.015Re_{D_h}^a Pr^b) (T_s - T_\infty) \quad (\text{A.8})$$

In the event of running at a lower Reynold's number, a solution for fully developed laminar flow with constant heat addition is also available for the desired thermal-hydraulic loop geometry.

Interest for the thermal modeling is always restricted to the heat flux though the outer surface, as described below; the outer surface Nusselt number as developed by Kays et al [26] is given in Equation A.9. This is further simplified by the constraint that the inner surface, if present, is adiabatic, reducing the Nusselt number to be solely dependent on the annular radius ratio,

$r^* = \frac{r_i}{r_o}$, as presented in Table A-1.

$$Nu_o = \frac{Nu_{oo}}{1 - \left(\frac{q_i''}{q_o''}\right)\theta_o^*} \quad (\text{A.9})$$

Table A-1: Circular-tube annulus solutions for constant heat rate [26]

r^*	Nu_{ii}	Nu_{oo}	θ_i^*	θ_o^*
0	∞	4.364	∞	0
0.05	17.81	4.792	2.18	0.0294
0.10	11.91	4.834	1.383	0.0562
0.20	8.499	4.883	0.905	0.1041
0.40	6.583	4.979	0.603	0.1823
0.60	5.921	5.099	0.473	0.2455
0.80	5.58	5.24	0.401	0.299
1.00	5.385	5.385	0.346	0.346

Using a similar process developed for the turbulent flow, given the Nusselt number, the convective heat transfer coefficient can be derived for laminar flow, and the equivalent to Equation A.8 generated. For both laminar and turbulent flows, determining the temperature difference between the heat transfer surface and centerline yields the local heat flux. Examining Figure A-3 for turbulent flow reveals that across the valid range of Prandtl numbers for Equation A.4 the centerline temperature may be approximated closely by the fluid's bulk temperature. The surface temperature may then be calculated using the first law of thermodynamics to equate Equations A.1 and A.2 at the surface interface, resulting in Equation A.10.

$$T_s = -\frac{k}{h_{conv}} \frac{\partial T}{\partial x_l} + T_\infty \quad (\text{A.10})$$

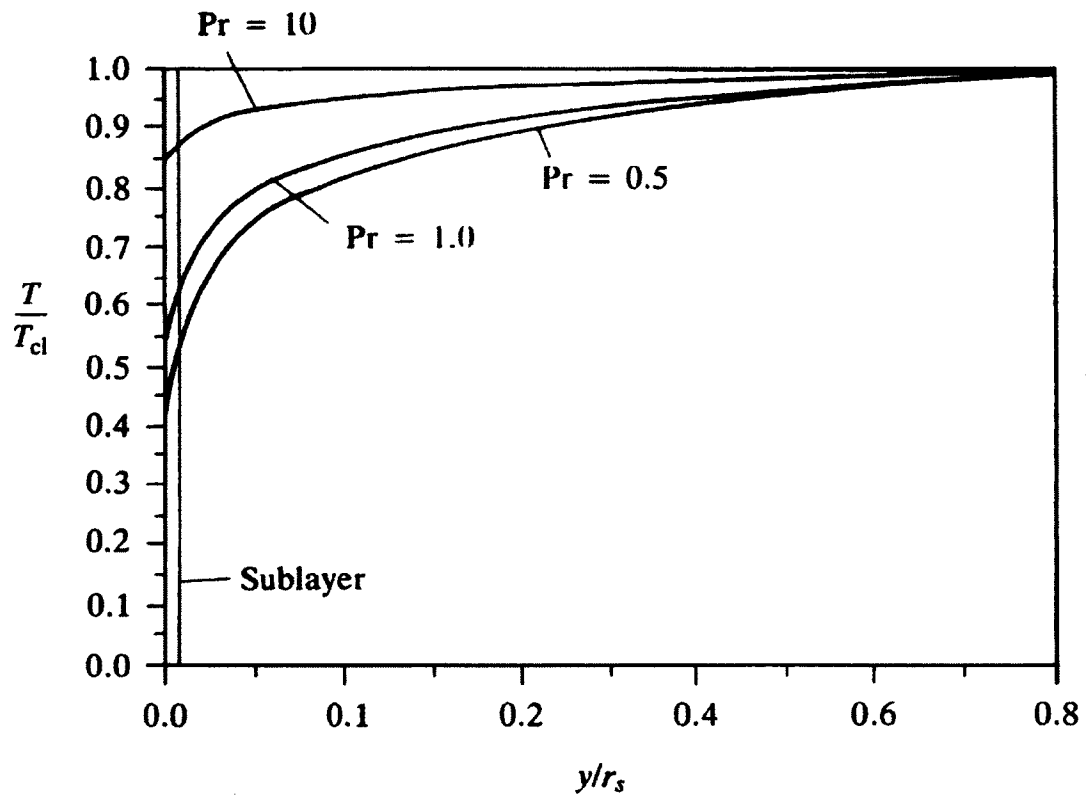


Figure A-3: Temperature profile for turbulent flow; $Re = 100,000$ [26]

Appendix B: Modeling Energy Continuity with the First Law of Thermodynamics

Using the convective heat transfer coefficient previously developed in Appendix A to account for heat transfer in the radial direction, and ignoring the viscous heating effects, the energy continuity Equation may be replaced with the Equation for the first law of thermodynamics for an open system (Eqn. B.1).

$$\frac{\partial E}{\partial t} = \frac{\partial Q}{\partial t} + \frac{\partial W}{\partial t} + \sum \dot{m} \left(h + \frac{u^2}{2} \right) \quad (\text{B.1})$$

Each term of the first law is independent, so the solution may be sought as a sum each contribution which may be solved independently:

$$\frac{\partial E}{\partial t} = \frac{\partial E}{\partial t_{work}} + \frac{\partial E}{\partial t_{heat}} + \frac{\partial E}{\partial t_{advection}} \quad (\text{B.2})$$

Work

The work contribution term to the energy Equation is limited to pump work exerted on the working fluid for the thermo hydraulic loop. The pump work is a predefined quantity that has a continuous first derivative. Where applicable the work term will therefore be represented as a time varying source applied across the flow path of a pump component.

$$\frac{\partial E}{\partial t_{work}} = \frac{\partial(\Delta p \dot{V})}{\partial t} \quad (\text{B.3})$$

The power term, $\Delta p \dot{V}$ is a user defined input as defined by the pumps operating characteristics. Since the viscous heating effect is ignored and only pump does any work in the loop, the work term is dropped from the general energy continuity Equation.

Heat

Heating of the fluid can be defined by using Gauss' law to convert the volumetric heating to the sum of heat fluxes through the element's faces.

$$\oint \dot{q}'' dA = \iiint \dot{q}''' dV \quad (\text{B.4})$$

From Appendix A the heat flux includes the contribution of both diffusion and convection terms at each face. This allows one to write the heat contribution term of the energy Equation as a first order partial differential Equation, including the heat fluxes and source terms, shown below.

$$\frac{\partial E}{\partial t}_{heat} = \sum -k \frac{\partial T}{\partial x_i} dA_i + \sum h (T_{s_j} - T_{\infty}) dA_j + \dot{Q}_{source} \quad (B.5)$$

Advection

The advection term (Eqn. B.6) may be solved directly since the mass flow and Equation of state is known throughout the fluid field. The use of specific enthalpy instead of internal energy as presented in Equation A.13 is convenient as it includes the pressure term which would otherwise need to be solved for simultaneously from the momentum continuity Equation.

$$\frac{\partial E}{\partial t}_{advection} = \sum \dot{m} \left(h + \frac{u^2}{2} \right) \quad (B.6)$$

Combining the simplifications and assumptions provides a complete set of one dimensional Equations to satisfy the heat transfer and frictional behavior of the fluid field. Mass continuity remains unchanged, but becomes directly coupled to the Equation of state to yield the velocity field. The momentum continuity Equation is replaced with a specific version to determine frictional affects, and becomes decoupled from the energy continuity Equation. With the momentum continuity Equation decoupled and the viscous terms neglected, the energy continuity is solved in the form of the first law of thermodynamics for an open system. The system of Equations provides a sufficiently accurate model for the transient thermal response of the fluid field for design applications.

$$\frac{\partial \rho}{\partial t} + \frac{\partial}{\partial x} (\rho u) = 0 \quad (B.7)$$

$$\frac{dp}{dx} = f \frac{\rho u^2}{2D_h} \quad (B.8)$$

$$\frac{\partial E}{\partial t} = \sum -k \frac{\partial T}{\partial x_i} dA_i + \sum h_{conv} (T_{s_j} - T_{\infty}) dA_j + \dot{Q}_{source} + \sum \dot{m} \left(h + \frac{u^2}{2} \right) \quad (B.9)$$

Appendix C: Stability of the DuFort-Frankel Method in Two Dimensions

In two dimensions, the DuFort Frankel Method for diffusion becomes:

$$\frac{T_{ij}^{n+1} - T_{ij}^{n-1}}{2\Delta t} = \frac{\alpha}{(\Delta x)^2} (T_{i-1,j}^n - T_{ij}^{n+1} - T_{ij}^{n-1} + T_{i+1,j}^n) + \frac{\alpha}{(\Delta r)^2} (T_{i,j-1}^n - T_{ij}^{n+1} - T_{ij}^{n-1} + T_{i,j+1}^n) \quad (C.1)$$

Applying the von Neumann stability analysis to this Equation with the Fourier component of the form:

$$T_{ij}^n = e^{at} e^{ik_x x} e^{ik_r r} \quad (C.2)$$

Yields the following stability criterion (Eqn. C.4) which for unconditional stability $|G| \leq 1$

$$G = \frac{2(r_x \cos(\beta_1) + r_r \cos(\beta_2)) \pm \sqrt{4(r_x \cos(\beta_1) + r_r \cos(\beta_2))^2 + 1 - 4(r_x - r_r)^2}}{1 + 2r_x + 2r_r} \quad (C.3)$$

$$r_x = \frac{\alpha \Delta t}{(\Delta x)^2} \quad (C.4.a)$$

$$r_r = \frac{\alpha \Delta t}{(\Delta r)^2} \quad (C.4.b)$$

$$\beta_1 = ik_x \Delta x \quad (C.4.c)$$

$$\beta_2 = ik_r \Delta r \quad (C.4.d)$$

The stability criterion for the two-dimensional Dufort-Frankel method cannot be expressed as a convenient equality like the simple explicit case (Eqn. C.5) shown below. Stability for the Dufort Frankle method is better represented graphically. Considering the function representing the stability criterion, the magnitude of $\cos(\beta_1)$, $\cos(\beta_2)$: $[-1, 1]$ while r_x, r_r : $(0, \infty)$, one is able to create a nested dataset as the trigonometric terms have a restricted scaling effect on the magnitude of the stability criterion.

$$\alpha \Delta t \left[\frac{1}{(\Delta x)^2} + \frac{1}{(\Delta y)^2} \right] \leq \frac{1}{2} \quad (C.5)$$

By holding r_x , and r_r constant while solving all combinations of β_1 , and β_2 a limiting value of G (the maximum) can be defined for the specified r_x , and r_r . Varying r_x , and r_r and plotting the

limiting value of G generates a solution space where various combinations of r_x , and r_r that yield unconditional stability may be easily identified.

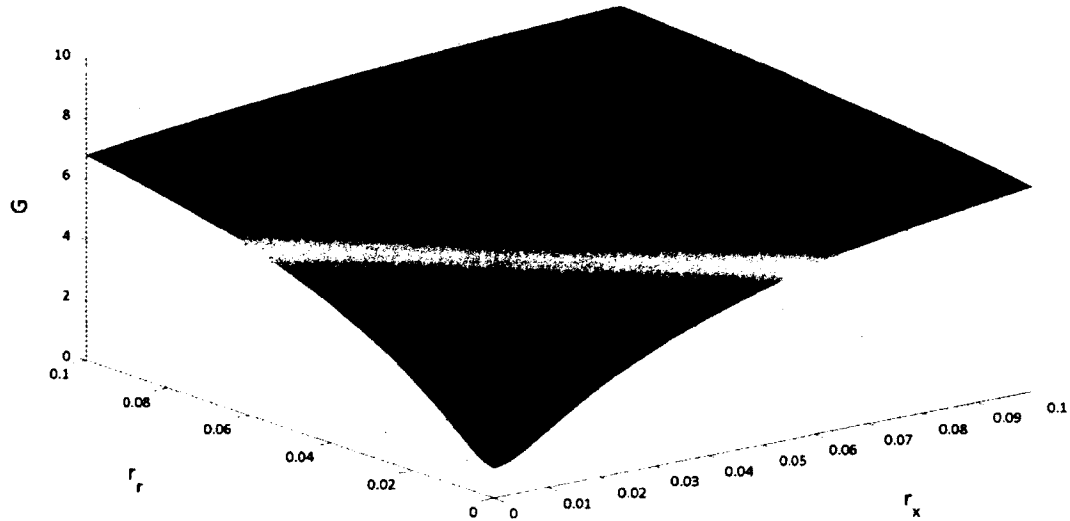


Figure C-1: Magnitude of Stability Criterion for the limiting values of β_1 and β_2 for the Two-Dimensional DuFort-Frankel Method.

As can be seen in the figure above, the 2 dimensional Dufort Frankle Method becomes unconditionally unstable, as the stability criterion is greater than one for all non-zero r_x , and r_r values. While higher order methods can be desirable for their higher order accuracies, the increased complexity in determining their universal stability as well as the potential change from unconditionally stable to unconditionally unstable transitioning from one-dimensional to two-dimensional results in the Explicit Euler as the scheme to be implemented.

Appendix D: SCW Thermal-Hydraulic Loop Parts

Name	Description	Manufacture	Model Number
Accumulator	Bladder accumulator	Accumulators Inc	A5TBG6100XS
Filter	20 µm Tee-type filter	Norman	4500 Series-587 Size
Flow Meter	Turbine Flow Meter	Flow Technology	FT-12C6XWBLED-6-FT-I
Globe Valve	316 SS, class 2500	Severn Glocon LTD	SAREx25-LTU-5.6
Heat Exchanger	U-Tube and Shell	AIC	K100728-15-17 (Ref#)
Pump	Centrifugal	Klaus Union	SLM HVHO 040-025-160-09T02
NPS 1.5" Pipe	316 SS, Schedule XXS	-	-
NPS ¾" Pipe	316 SS, Schedule 160	-	-
1.5" #2500 Flange	316 SS, Schedule XXS	-	-
¾" #2500 Flange	316 SS, Schedule 160	-	-
Grayloc Connector	Hub or T-joint, NPS 1.5"	Grayloc	1-1/2 GR11